

THE EARTH'S MAGNETOTAIL DURING
VARYING LEVELS OF GEOMAGNETIC
ACTIVITY

Elizabeth Anne Davey

A Thesis submitted for the degree of

Doctor of Philosophy

at the University of Leicester

Radio and Space Plasma Physics Group

Department of Physics and Astronomy

University of Leicester, U.K.

August 2012

Abstract

The Earth's Magnetotail during varying levels of geomagnetic activity

Elizabeth Anne Davey

This thesis describes work that has employed both ground- and space-based data to investigate the magnetotail and its response to differing levels of geomagnetic activity.

The first study of current sheet motion involved analysing the number of crossings that the Cluster 3 spacecraft made of the cross-tail current sheet, as a measure of current sheet dynamics. Geomagnetic conditions measured during the crossings allowed a comparison of the current sheet dynamics during substorms, magnetic storms and quiet times. The results indicated that more motion of the current sheet is seen during substorms compared to quiet times. In addition, there was evidence that current sheet motion is suppressed when the ring current is enhanced.

An analysis of current sheet structure is presented in the next study, which examines the orientation, current density and thickness of the current sheet. The current sheet was found to be more tilted during substorms than quiet times and when magnetic storms were occurring the tilt was reduced. The current density analysis showed larger values during storms compared to quiet and substorm times.

The final study investigated how the lobe magnetic field varies according to geomagnetic activity. Results are presented showing evidence of a larger lobe magnetic field during magnetic storms, compared to quiet times and substorms.

The thesis work provides a more complete picture of the current sheet and lobes, during different levels of geomagnetic activity, than has been previously shown. There is evidence that substorm occurrence is related to current sheet motion and a highly tilted orientation. The increased lobe field found during magnetic storms may cause a rigidity to the magnetotail that suppresses this motion and its tilting in the YZ plane. The increased lobe field also results in an increased current density in the current sheet during storms.

Acknowledgements

To be honest, I really didn't think I'd ever get to the stage of writing this bit! I owe thanks to Prof Mark Lester firstly, for putting up with me as his student and never making me feel stupid when I ask ridiculously simple questions. I am grateful for all his time and support and couldn't have picked a better supervisor. Thanks also to Prof Steve Milan for always providing support when I needed it. Thanks to everyone in RSPP - what a great group of people, thank you for being fab! Special thanks to my office mates (past and present), in particular Steph, Sarah and Suzie, for cakes, chocolate, gossip, laughs and above all huge support. Thanks to Rob Fear for always taking the time to explain things to me and helping hugely at various stages along the way. Finally, thanks to Prof. Stan Cowley who petrified me every time he asked me a question in the group meetings, and while I hope it didn't show, I'm sure it did! Thanks for teaching me a lot and having a great research group filled with great people.

And so my biggest thanks go to Graham, who has put up with me, especially when I've constantly been saying that I can't do this PhD! If I didn't have him around, I wouldn't have got this far at all and I wouldn't get far with anything really. Thank you for constantly saying "Molehills not mountains, Elizabeth!" when I'm in panic-mode. And of course, my little Tegan, you are amazing and never forget that. Thanks also to Mum, Dad and Emma for endless support and encouragement.

I would also like to thank the STFC for providing the funds for my studies and to all the instrument teams for the data that I have used in this thesis.

Declarations

The research undertaken during the course of this doctoral programme has led to the submission and publication of the following scientific papers:

Davey, E. A., M. Lester, S. E. Milan and R. C. Fear (2012), Storm and substorm effects on magnetotail current sheet motion, *J. Geophys. Res.*, *117*, *A02202*, doi:10.1029/2011JA017112.

Davey, E. A., M. Lester, S. E. Milan, R. C. Fear, and C. Forsyth (2012), The orientation and current density of the magnetotail current sheet: a statistical study of the effect of geomagnetic conditions, *J. Geophys. Res.*, *117*, *A07217*, doi:10.1029/2012JA017715.

Contents

1	Introduction	1
1.1	Plasma Physics	1
1.1.1	Single particle motion	2
1.1.1.1	Particle gyration and mirroring	3
1.1.1.2	Particle drift	5
1.1.2	Magnetohydrodynamics	7
1.1.2.1	Frozen-in flow	8
1.1.2.2	Magnetic Reynolds Number	11
1.1.2.3	Magnetic reconnection	12
1.1.3	Solar-terrestrial physics	12
1.1.3.1	Solar wind and interplanetary magnetic field	12
1.1.3.2	The Earth's magnetosphere	14
1.1.3.3	The magnetotail	15
1.1.3.4	Geomagnetic disturbances	17
2	The Earth's magnetotail	21
2.1	General size and structure of the tail	21
2.2	Currents in the magnetotail	24
2.3	General effects on the tail	26
2.4	The cross-tail current sheet	29
2.4.1	Current sheet motion	29
2.4.2	Current sheet structure	32
2.4.2.1	Current sheet tilt	32
2.4.2.2	Current sheet current density	35
2.4.2.3	Current sheet profile and thickness	37
2.5	Magnetotail lobes	39
2.6	Research questions	44

3	Instrumentation and data analysis	47
3.1	The Cluster Mission	47
3.1.1	Cluster's Fluxgate Magnetometer	50
3.1.2	Cluster Ion Spectrometer	52
3.2	OMNI data	54
3.3	Ground-based measurements	54
3.3.1	SYM-H data	55
3.3.2	AE data	56
3.4	Analysis techniques	56
3.4.1	Minimum Variance Analysis	56
3.4.2	The Curlometer technique	58
3.4.3	Mann Whitney Test	60
3.5	Coordinate Systems	60
4	Current sheet motion	63
4.1	Selection of dataset	64
4.2	Orbit analysis	71
4.2.1	Geomagnetic activity	72
4.2.2	The influence of substorms and magnetic storms	74
4.3	Normalising the data	77
4.4	Discussion	81
4.5	Conclusions	83
5	Current sheet structure	85
5.1	Introduction	85
5.2	Methodology	86
5.2.1	Selection of dataset	86
5.2.2	Data analysis methods	86
5.3	Results	88
5.3.1	Current sheet orientation	88
5.3.2	Current sheet current density	94
5.4	Discussion	99
5.4.1	Tilt angle analysis	100
5.4.2	Current density analysis	102
5.5	Conclusions	105

6	Magnetotail lobes	106
6.1	Introduction	106
6.2	Lobe selection	106
6.3	Position and dynamic pressure variation	108
6.3.1	Normalisation	110
6.4	Influence of geomagnetic activity	113
6.5	Discussion	121
6.5.1	Data analysis and normalisation	122
6.5.2	Influence of substorms and magnetic storms	123
6.6	Conclusions	125
7	Summary and future work	126
7.1	Introduction	126
7.2	Thesis summary	127
7.3	Future work	130

List of Figures

1.1	Particle gyration and mirroring.	5
1.2	The Frozen-in Theorem.	9
1.3	The Parker Spiral.	13
1.4	The magnetosphere.	16
1.5	The Dungey Cycle.	18
1.6	An example of a magnetic storm.	19
2.1	Diagram of the Earth’s magnetosphere.	22
2.2	Summary of magnetotail size research.	23
2.3	Magnetospheric currents.	25
2.4	<i>Zhang et al.</i> [2005]’s current sheet crossings.	30
2.5	Current sheet in motion.	31
2.6	<i>Sergeev et al.</i> [2006]’s Superposed epoch study results.	33
2.7	<i>Petrukovich et al.</i> [2005]’s current sheet crossings.	34
2.8	<i>Thompson et al.</i> [2005]’s superposed epoch analysis.	36
2.9	<i>Zhang et al.</i> [2006]’s current sheet crossings.	37
2.10	<i>Runov et al.</i> [2006]’s current sheet crossings.	38
2.11	<i>Slavin et al.</i> [1985]’s lobe field strength with distance downtail.	40
2.12	Lobe field strength with distance downtail.	41
2.13	<i>Fairfield and Jones</i> [1996]’s radial gradient of the lobe field.	42
2.14	<i>Fairfield and Jones</i> [1996]’s radial gradient of the lobe field after normalisation.	42
2.15	<i>Nakai et al.</i> [1999]’s radial gradient of the equatorial region.	43
2.16	<i>Nakai et al.</i> [1999]’s radial gradient of the lobe field.	44
3.1	Cluster spacecraft.	48
3.2	Cluster orbits.	49

3.3	Basic fluxgate magnetometer.	51
3.4	Curlometer technique.	58
3.5	GSM coordinate system.	62
4.1	Examples of crossings of the current sheet by Cluster 3.	66
4.2	Positions of current sheet crossings.	67
4.3	Distributions of number of crossings per orbit for different thresholds in B_X	69
4.4	Mean number of crossings per orbit per year.	70
4.5	Example of Cluster 3 orbits in 2002 and 2007.	71
4.6	Comparison of an inactive to an active current sheet.	73
4.7	Comparison of an inactive to an active current sheet for different thresholds of crossing for 2001-2004.	74
4.8	Comparison of number of crossings for quiet, substorm and storm conditions.	75
4.9	Comparison of geomagnetic conditions for different thresholds of crossing.	77
4.10	Comparison of an inactive to an active current sheet for the normalised data.	79
4.11	Comparison of number of crossings for different geomagnetic conditions for the normalised data.	80
5.1	Distribution of tilt angle with SYM-H and AE.	89
5.2	Distribution of tilt angle with SYM-H and AE separated into bins.	90
5.3	Mean tilt angle with position.	92
5.4	Mean tilt angle for different geomagnetic conditions.	93
5.5	Mean tilt angle for geomagnetic conditions for 2001-2004.	94
5.6	Mean maximum current density with position.	95
5.7	Mean current density for different geomagnetic conditions.	97
5.8	Mean current density for 2001-2004.	98
6.1	Variation of lobe magnetic field with dynamic pressure.	108
6.2	Variation of lobe magnetic field with dynamic pressure.	109
6.3	Non-linear fit of the variation of lobe magnetic field with downtail position.	110
6.4	Variation of normalised lobe magnetic field with dynamic pressure.	111
6.5	Variation of final normalised lobe magnetic field with position.	112

6.6	Variation of final normalised lobe magnetic field with position with geomagnetic activity.	114
6.7	Variation of final normalised lobe magnetic field with SYM-H and AE.	115
6.8	Variation of final normalised lobe magnetic field with SYM-H and AE.	117
6.9	Variation of final normalised lobe magnetic field with SYM-H and AE.	119
6.10	Variation of final normalised lobe magnetic field with AE for the north and south lobe.	120
6.11	Final normalised lobe magnetic field for different levels of geomagnetic activity.	120

List of Tables

3.1	Cluster Instrument list	50
6.1	Summary of magnetic storm lobe field events.	116
7.1	Summary of main results	130

Chapter 1

Introduction

This thesis is concerned with the cross-tail current sheet dynamics, structure and intensity of the magnetotail of the Earth's magnetosphere. The main focus of the work has been to study the magnetic field data from spacecraft orbiting the Earth, through this region. However, before discussing the studies in detail, it is important to introduce some of the basic plasma physics concepts that underpin how magnetic fields and plasmas behave and relevant information regarding solar terrestrial physics.

1.1 Plasma Physics

Plasmas are very low density gases consisting of ionised particles and since there are usually an equal number of positive and negative charges, are considered in a general sense, to be electrically neutral. The collisions between particles in these gases are usually treated as negligible (on timescales of the collective processes) and as such, particle motions are treated in terms of how the charged particles react to electric and magnetic fields. It is possible to describe interactions of individual particles with electromagnetic forces (see Section 1.1.1) and also to consider collec-

tions of particles (1.1.2). Both approaches are used to understand the behaviour of a plasma and are the basis of the work in this thesis. The following sections will describe some important aspects of both descriptions of plasmas as well as introducing some relevant concepts in solar terrestrial physics (1.1.3).

1.1.1 Single particle motion

As will be discussed in more detail later, the Earth's near-space environment is one that is defined by varying magnetic field, plasma flows and current systems. By understanding how individual charged particles behave in electromagnetic fields, it can be shown that particles gyrate around magnetic field lines and that changes in that field result in various particle drifts. These concepts describe how the plasma within the magnetosphere behaves under different influences. Whilst the details of some of the theories discussed here are not directly the focus of the research described in the thesis, they provide the basis for the behaviour of the different regions of the magnetosphere under varying geomagnetic conditions. How the magnetosphere responds to geomagnetic activity is the underlying theme of the thesis and as such it is appropriate to introduce some of the relevant basic plasma physics. In addition, some of the concepts and equations described here are directly used in the research, such as the application of Ampère's Law to the Curlometer technique (Chapter 3).

The motion of individual charged particles is described by the equation of motion of a charged particle in an electromagnetic field and Maxwell's Equations, shown below.

$$m \frac{d\mathbf{v}}{dt} = q(\mathbf{E} + \mathbf{v} \times \mathbf{B}) \quad \text{Equation of motion} \quad (1.1)$$

$$\nabla \cdot \mathbf{B} = 0 \quad \text{Gauss's Law for magnetism} \quad (1.2)$$

$$\nabla \cdot \mathbf{E} = \frac{\rho_q}{\epsilon_0} \quad \text{Gauss's Law} \quad (1.3)$$

$$\nabla \times \mathbf{E} = -\frac{\partial \mathbf{B}}{\partial t} \quad \text{Faraday's Law} \quad (1.4)$$

$$\nabla \times \mathbf{B} = \mu_0 \epsilon_0 \frac{\partial \mathbf{E}}{\partial t} + \mu_0 \mathbf{J} \quad \text{Ampère's Law} \quad (1.5)$$

where m and \mathbf{v} are the mass and velocity of the particle, ρ_q is the charge density, μ_0 is the permeability of free space, ϵ_0 is the permittivity of free space and \mathbf{J} is the current density. The first term on the right hand side of Ampère's Law is the displacement current and is usually ignored in space plasma physics as the variations in electric field (\mathbf{E}) are assumed to take place over large time scales. These equations can be used to describe particle motion under different conditions, some of which are discussed in the following sections.

1.1.1.1 Particle gyration and magnetic mirroring

In the equation of motion (1.1), the right hand side terms are the Coulomb force due to the electric field and the Lorentz force acting on the particle due to the magnetic field (\mathbf{B}). The Lorentz force acts in a direction perpendicular to both \mathbf{B} and \mathbf{v} . In a situation where there is no electric field and the magnetic field is assumed to be uniform and steady in the Z direction, equation 1.1 is then,

$$m \frac{d\mathbf{v}}{dt} = q(\mathbf{v} \times \mathbf{B}) \quad (1.6)$$

Differentiation of individual components of this equation lead to an equation of simple harmonic motion, indicating that a charged particle will gyrate around

a magnetic field line (its guiding centre) with a gyroradius (r_g) and gyrofrequency (ω_g),

$$r_g = \frac{mv_{\perp}}{qB} \quad (1.7)$$

$$\omega_g = \frac{qB}{m} \quad (1.8)$$

where x , y and z are cartesian coordinates, the magnetic field is directed along the z direction and v_{\perp} the velocity perpendicular to the field $= \sqrt{(v_x)^2 + (v_y)^2}$ and $v_{\parallel} = v_z$. The gyroradius is dependent on the mass and charge of the particle and as such, electrons and ions will gyrate in opposite directions, with electrons having smaller gyroradii. It can also be shown, that the total velocity ($v = \sqrt{(v_{\perp})^2 + (v_{\parallel})^2}$) is constant and thus the kinetic energy of a particle in a magnetic field does not change. The gyration of particles is shown in panel (a) of Figure 1.1, taken from *Prölss and Bird* [2004].

If the electric field is still ignored but the magnetic field is considered not to be uniform, for example in a converging magnetic field, it can be shown that as the magnetic field increases the perpendicular velocity increases, and the parallel velocity decreases, to a point where the magnetic field is large enough for the parallel velocity to be zero. This point is called the ‘Mirror Point’ and occurs in the magnetic field of the Earth, which converges towards the poles. Without any electric field present, the particle gyrates around a magnetic field line, approaching the mirror point, where it reverses in direction, towards the opposite pole, and the situation repeats. This is termed ‘Magnetic Mirroring’ and is shown in panel (b) of Figure 1.1.

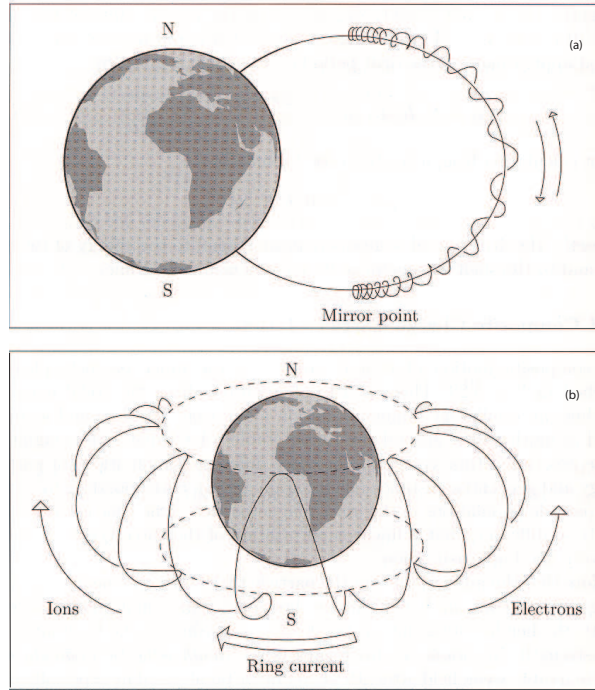


Figure 1.1: Diagram showing the gyration (a) and mirroring (b) of particles in the Earth's magnetic field. Taken from *Prölss and Bird* [2004].

1.1.1.2 Particle drift

If an electric field is present, the equation of motion remains in the form shown in equation 1.1. This can be manipulated and the expression for the perpendicular velocity becomes

$$\mathbf{v}_{\perp} = \frac{\mathbf{E} \times \mathbf{B}}{B^2} - \frac{m}{qB^2} \frac{d\mathbf{v}}{dt} \times \mathbf{B} \quad (1.9)$$

Whilst the second term on the right-hand side of equation 1.9 describes particle gyration (Section 1.1.1.1) and is dependent on the mass and charge of the particle, the first term is a velocity that is independent of mass or charge, and as a result all particles move in the same direction and no current exists. This motion is usually called the ' **$\mathbf{E} \times \mathbf{B}$ drift**' and acts in a direction perpendicular to both **\mathbf{E}** and

B. Although it is called the $\mathbf{E} \times \mathbf{B}$ drift, the perpendicular velocity is, in fact, inversely proportional to the magnetic field. Of relevance to this thesis, the $\mathbf{E} \times \mathbf{B}$ drift occurs in the magnetotail, during convection. The plasma undergoes an $\mathbf{E} \times \mathbf{B}$ drift towards the plasma sheet in each lobe and then once reconnection has occurred, in a direction towards the Earth. This is described in more detail in Chapter 2.

Another drift occurs when there is a gradient in the magnetic field, in a direction perpendicular to the field, called the ‘**grad-B** drift’. Note that a gradient in the magnetic field parallel to the magnetic field results in magnetic mirroring discussed in Section 1.1.1.1. **Grad-B** drift occurs when there is a gradient perpendicular to the field that occurs on a similar scale to the particle’s gyroradius. As a result there is motion of the particle in a direction perpendicular to both the gradient of the magnetic field and the direction of the magnetic field itself. Because the ions and electrons move in opposite directions, a current is produced. The gradient drift can be described as

$$\mathbf{v}_{gradB} = \frac{mv_{\perp}^2}{2qB^3}(\mathbf{B} \times \nabla B) \quad (1.10)$$

Grad-B drift occurs close to the Earth causing a drift of particles and a current in a westward direction around the Earth.

The final drift to consider is the ‘Curvature drift’ which occurs where the direction of the magnetic field changes along the field line, for example on a curved magnetic field line of the Earth. Again this drift is charge dependent and so a current is produced. The curvature drift can be described as

$$\mathbf{v}_{curv} = \frac{mv_{\parallel}^2}{qB^2} \frac{\mathbf{R}_c \times \mathbf{B}}{R_c^2} \quad (1.11)$$

where R_c is the radius of curvature of the field line.

Both the grad-B and curvature drifts give rise to the ring current, described in

Section 1.1.3.4.

1.1.2 Magnetohydrodynamics

Magnetohydrodynamics (MHD) considers the plasma as a fluid and can be described with Maxwell's equations (Equations 1.2-1.5) and two conservation equations, shown below.

$$\frac{\partial \rho}{\partial t} + \nabla \cdot (\rho \mathbf{v}) = 0 \quad \text{Conservation of mass} \quad (1.12)$$

$$\rho \frac{d\mathbf{v}}{dt} = \rho \mathbf{g} - \nabla P + \rho_q \mathbf{E} + \mathbf{j} \times \mathbf{B} \quad \text{Conservation of momentum} \quad (1.13)$$

where \mathbf{v} is the centre of mass velocity or bulk velocity, ρ is the mass density, P is the pressure, ρ_q is the charge density of the ions and electrons and \mathbf{j} is the current density. Ideal MHD considers that plasmas studied at large scales are infinitely conducting and that parameters vary slowly compared to the gyrofrequency.

The last term of Equation 1.13 ($\mathbf{j} \times \mathbf{B}$), the magnetic force per unit volume, can be manipulated, using Ampère's Law (1.5), while ignoring the displacement current, such that

$$\begin{aligned} \mathbf{j} \times \mathbf{B} &= \frac{1}{\mu_0} (\nabla \times \mathbf{B}) \times \mathbf{B} \\ &= \frac{1}{\mu_0} (\mathbf{B} \cdot \nabla) \mathbf{B} - \nabla \left(\frac{B^2}{2\mu_0} \right) \end{aligned} \quad (1.14)$$

Thus the magnetic force comprises two components, magnetic pressure and magnetic tension. The last term of Equation 1.14 is the magnetic pressure force component (P_m) and at a boundary between a plasma and magnetic field, an

equilibrium can be attained where the magnetic pressure, P_m , is equal to the plasma pressure, P_P , so that

$$P_m = \frac{B^2}{2\mu_0} = P_P = nk_B T \quad (1.15)$$

where k_B is Boltzmann's constant.

The first term on the right-hand side of Equation 1.14 describes the tension force per unit volume exerted by the magnetic field. This force acts to straighten bent magnetic field lines. An example of this occurring in the magnetosphere follows reconnection in the tail, where magnetic field lines are forced Earthwards during magnetospheric convection.

1.1.2.1 MHD induction equation and frozen-in flow

Ohm's Law states that

$$\mathbf{j} = \sigma(\mathbf{E} + \mathbf{v} \times \mathbf{B}) \quad (1.16)$$

where σ is the conductivity of the medium where the current is flowing.

Taking the curl of the above yields

$$\frac{1}{\sigma}(\nabla \times \mathbf{j}) = \nabla \times (\mathbf{E} + \mathbf{v} \times \mathbf{B}) \quad (1.17)$$

Substituting Ampère's Law (1.5) and Faraday's Law (1.4) gives

$$\frac{1}{\mu_0\sigma}(\nabla \times \nabla \times \mathbf{B}) = \frac{-\partial\mathbf{B}}{\partial t} + \nabla \times (\mathbf{v} \times \mathbf{B}) \quad (1.18)$$

Rearranging and using the vector identity $\nabla \times \nabla \times \mathbf{B} = \nabla(\nabla \cdot \mathbf{B}) - (\nabla \cdot \nabla)\mathbf{B}$ and equation 1.2 gives

$$\frac{\partial\mathbf{B}}{\partial t} = (\nabla \times \mathbf{v} \times \mathbf{B}) + \frac{1}{\mu_0\sigma}(\nabla^2\mathbf{B}) \quad (1.19)$$

Therefore in a perfectly conducting plasma, with infinite conductivity, the second term on the right hand side is negligible and the remaining terms form the MHD

induction equation, shown below. This indicates that the flux is ‘frozen-in’ to the plasma and vice versa.

$$\frac{\partial \mathbf{B}}{\partial t} = (\nabla \times \mathbf{v} \times \mathbf{B}) \quad \text{MHD induction equation} \quad (1.20)$$

An alternative method of showing that is by considering a closed contour, C , which is the boundary of a surface, S (see Figure 1.2). The magnetic flux through the surface,

$$\Phi = \int_S \mathbf{B} \cdot d\mathbf{S} \quad (1.21)$$

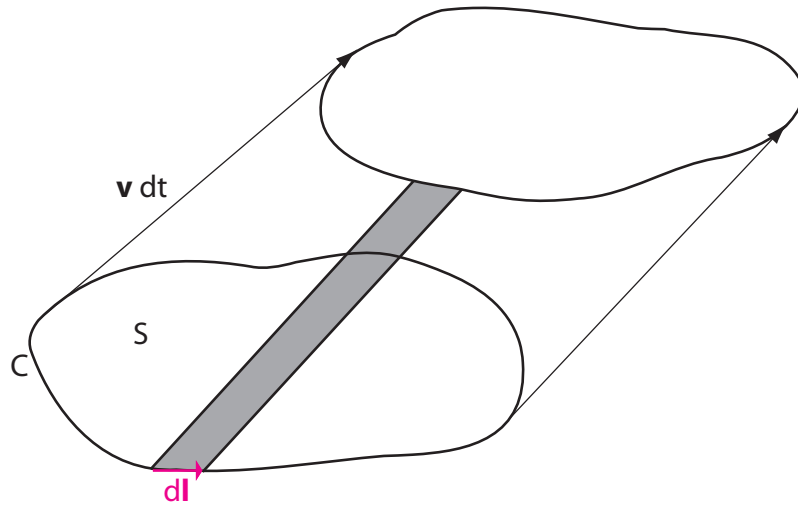


Figure 1.2: Diagram showing proof of the Frozen-in Theorem.

As the surface changes over time, the magnetic flux will also change in two ways. Firstly, changes of the magnetic field with time result in a change of

$$\frac{\partial \phi_1}{\partial t} = \int_S \frac{\partial \mathbf{B}}{\partial t} \cdot d\mathbf{S} \quad (1.22)$$

Secondly the closed contour C will also change with time. If the element dl moves

with a plasma velocity of \mathbf{v} over a time dt , then it sweeps an area $d\mathbf{S}$ out which is

$$\mathbf{v}dt \times d\mathbf{l} \quad (1.23)$$

The resultant change in flux, due to changes in the surface contour, C is

$$\begin{aligned} \partial\phi_2 &= \int_C \mathbf{B} \cdot d\mathbf{S} \\ &= \int_C \mathbf{B} \cdot \mathbf{v} \times d\mathbf{l} \\ &= \int_C d\mathbf{l} \cdot \mathbf{B} \times \mathbf{v} \\ &= - \int_C \mathbf{v} \times \mathbf{B} \cdot d\mathbf{l} \end{aligned} \quad (1.24)$$

Combining these, the total rate of change of flux is

$$\frac{d\phi}{dt} = \int_S \frac{\partial \mathbf{B}}{\partial t} \cdot d\mathbf{S} - \int_C \mathbf{v} \times \mathbf{B} \cdot d\mathbf{l} \quad (1.25)$$

Stoke's Theorem states that

$$\int_C \mathbf{B} \cdot d\mathbf{l} = \int_S \nabla \times \mathbf{F} \cdot d\mathbf{S} \quad (1.26)$$

and if this is applied, the total change in flux becomes

$$\frac{d\phi}{dt} = \int_S \frac{\partial \mathbf{B}}{\partial t} \cdot d\mathbf{S} - \int_S \nabla \times (\mathbf{v} \times \mathbf{B}) \cdot d\mathbf{S} = \int_S \left(\frac{\partial \mathbf{B}}{\partial t} - \nabla \times (\mathbf{v} \times \mathbf{B}) \right) \cdot d\mathbf{S} \quad (1.27)$$

Substituting the MHD induction equation yields

$$\frac{d\phi}{dt} = \int_S \left(\frac{\partial \mathbf{B}}{\partial t} - \frac{\partial \mathbf{B}}{\partial t} \right) \cdot d\mathbf{S} = 0 \quad (1.28)$$

Thus, there is no change in flux with time and the flux is said to be 'frozen-in' with

the plasma and vice versa. This condition only holds when the MHD induction equation is valid. As a result, for low density plasmas, such as exist in the magnetosphere, the conductivity is high and in general the ‘frozen-in’ approximation holds. This is also known as Alfvén’s Theorem.

1.1.2.2 Magnetic Reynolds Number

The first term on the right hand side of equation 1.19 can be described as the convective term as it shows how the fluid and plasma are frozen together and move under the $\mathbf{E} \times \mathbf{B}$ drift. The second term on the right hand side describes how the magnetic field can diffuse through the medium (diffusion term) and for high conductivities is negligible. The equation can be written in its dimensional format as

$$\frac{B}{\tau} = \frac{VB}{L} + \frac{B}{L^2\mu_0\sigma} \quad (1.29)$$

where B is the average magnetic field strength, τ is the time duration of the magnetic field variations, V is the average perpendicular (to the field) plasma velocity, σ is the conductivity, μ_0 is the permeability of free space and L is the distance over which the field varies. The ratio of the first and second terms on the right hand side is the Magnetic Reynolds Number,

$$R_m = \mu_0\sigma VL \quad (1.30)$$

When the conductivity of the medium, σ , is large and the characteristic scale length of the field variations (L) is also large, then $R_m \gg 1$. In this case, the convective transport term dominates (the frozen-in condition applies). In the solar wind, $R_m \approx 7 \times 10^{16}$ and the frozen-in flux situation holds true [*Baumjohann and Treumann, 1996*]. If $R_m \ll 1$, then the diffusion term will dominate and the

frozen-in condition no longer applies. In this situation the magnetic field can then diffuse through the plasma and reconnection can occur, which is discussed in the next section.

1.1.2.3 Magnetic reconnection

Magnetic reconnection occurs when Alfvén’s Theorem breaks down, i.e. when the Magnetic Reynolds Number is much less than unity. Magnetic reconnection describes the process when opposing magnetic field lines meet and merge. When there are regions of magnetic field lines of opposite direction and if Alfvén’s Theorem remains true, then Ampère’s Law (1.5) states that a current sheet will exist between the two regions. However as the two regions become closer, Alfvén’s Theorem breaks down and the magnetic field lines ‘break’ and reconnect. Due to magnetic tension forces, described in 1.1.2, the field lines move away from the reconnection site, often called the ‘neutral line’ or ‘X-line’. This process occurs at the magnetopause, where energy is transferred from the solar wind into the magnetosphere and in the magnetotail, where energy is transferred from the tail into the inner plasmasphere. These interactions are discussed in more detail in Section 1.1.3.

1.1.3 Solar-terrestrial physics

1.1.3.1 Solar wind and Interplanetary magnetic field

The solar wind is the term used to describe the outflow of ionised plasma from the Sun and the interplanetary magnetic field (IMF, the Sun’s magnetic field) which permeates it. As the plasma and magnetic field leave the Sun’s corona, they form what is called the ‘Parker Spiral’ shown in Figure 1.3. The magnetic field lines forming the IMF are rooted to the Sun’s corona and due to the Sun’s rotation, form a spiral as they pervade the interplanetary space. The solar plasma consists

of mainly ionised Hydrogen, with ionised Helium and smaller amounts of heavier elements. At about 1 AU (Astronomical Unit) the solar wind reaches the Earth and has a typical speed of about 400 km s^{-1} and a pressure of about 30 nPa [Kivelson and Russell, 1995]. Particle densities are approximately 7 cm^{-3} and typical temperatures are about 10^5 K [Kivelson and Russell, 1995].

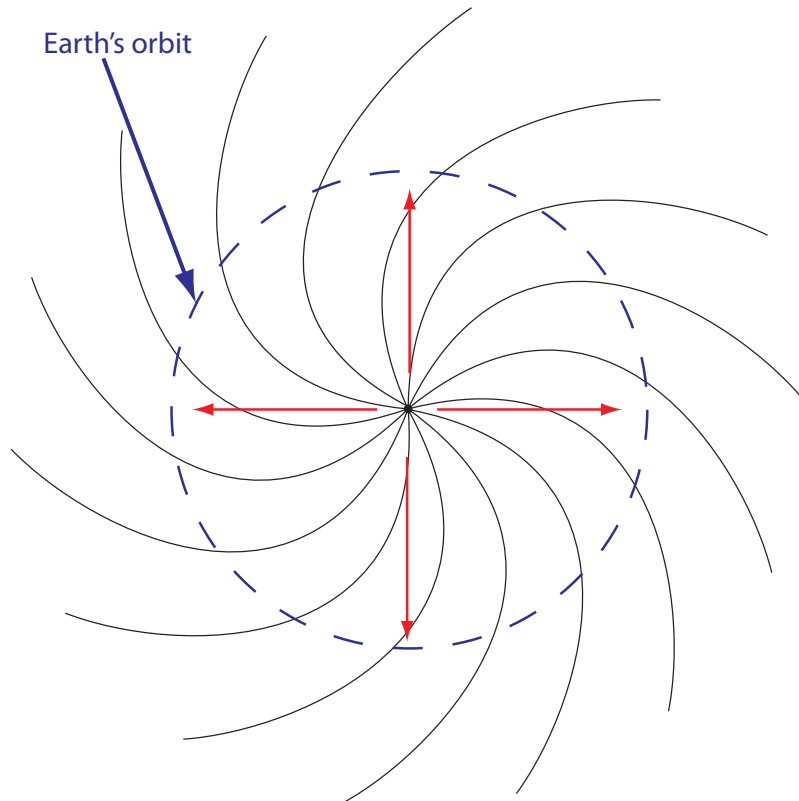


Figure 1.3: The Parker Spiral. Based on a figure from *Kivelson and Russell* [1995]. The Sun is at the centre of the diagram, showing the solar wind escaping and passing the Earth's orbit. The black lines show the magnetic field orientation and the red arrows indicate the solar wind flow.

Although there is regular interaction between the IMF and magnetosphere, there are two types of phenomena that are generated from the solar corona and travel into interplanetary space, which play an important role in particularly strong coupling between the solar wind and the Earth's magnetic field. These are co-rotating interaction regions (CIRs) and coronal mass ejections (CMEs). CIRs are

formed from the interaction between fast and slow solar wind streams from the solar corona. Fast solar wind catches up with slow solar wind regions further downstream and a compressed region forms ahead of the fast solar wind and a rarefaction region behind. Due to the CIRs being related to the Sun's rotation, these effects can be observed at the Earth at a frequency of about every 27 days. CMEs are explosive ejections of plasma from the corona, often from solar flares. These are more frequent during the peak of the solar cycle compared to lower solar activity and are non-recurrent [Gopalswamy *et al.*, 2004]. Although the solar wind regularly interacts with the Earth's magnetic field, both CIRs and CMEs cause strong coupling and active magnetospheric conditions. The solar wind-magnetospheric coupling, including that following CIRs and CMEs, is described in the following sections.

1.1.3.2 The Earth's magnetosphere

The region of space comprising the Earth's magnetic field (the magnetosphere, Figure 1.4) acts as obstacle to the flow of the solar wind [Chapman and Ferraro, 1930]. This is due to the fact that the geomagnetic field and associated plasma are 'frozen together' in the same way that the solar wind plasma and IMF are 'frozen-in', due to Alfvén's Theorem, described in 1.1.2.1. The approaching solar wind is supersonic and a bow shock is formed just outside the magnetosphere. Between the bow shock and magnetosphere is the magnetosheath, formed from the solar wind plasma being decelerated due to the shock front, resulting in temperature rises and increased particle densities in this region. The magnetopause is the boundary that separates the magnetosheath from the magnetosphere. Ampère's Law (1.5) tells us that a current sheet exists along the magnetopause (the Chapman-Ferraro current) as it separates two regions of magnetic field which can change substantially in direction and strength.

The general shape of the magnetosphere depends on the balance between the pressure exerted by the magnetosheath and that of the magnetosphere. The mag-

netosheath pressure comprises the thermal and magnetic pressures, however it is mainly determined by the solar wind dynamic pressure. The magnetospheric pressure is dominated by magnetic pressure. As such at the nose of the magnetosphere, the two pressures are in equilibrium, and

$$\rho_{sw} u_{sw}^2 = \frac{B_{ms}^2}{2\mu_0} \quad (1.31)$$

where ρ_{sw} is the solar wind density, u_{sw} is the solar wind speed, B_{ms} is the magnetospheric magnetic field and μ_0 is the permeability of free space.

Figure 1.4 is a representation of the magnetosphere showing some of the main current systems and regions. In a general sense the solar wind pressure pushes the nose of the magnetopause towards the Earth on the dayside and the nightside magnetosphere is stretched out to form the magnetotail, discussed in the next section.

1.1.3.3 The magnetotail

The magnetotail, located on the nightside of the Earth, is an important region within the magnetosphere due to its role in geomagnetic disturbances and is the main area of interest in this thesis. The magnetotail acts as a storage facility of plasma and energy, particularly during geomagnetic activity. It is also the region which forces plasma towards the Earth, following magnetic reconnection in the central plasma sheet in the tail, producing effects on the Earth such as the aurora, as well as more destructive effects that can occur during large magnetic storms such as disruption to satellite communications and power grids on the ground.

Figure 1.4 shows the main regions within the magnetotail, which consists of the north and south lobes, together forming the cylindrical shape of the tail. The plasma sheet and plasma sheet boundary layer (PSBL) separate the lobes and are

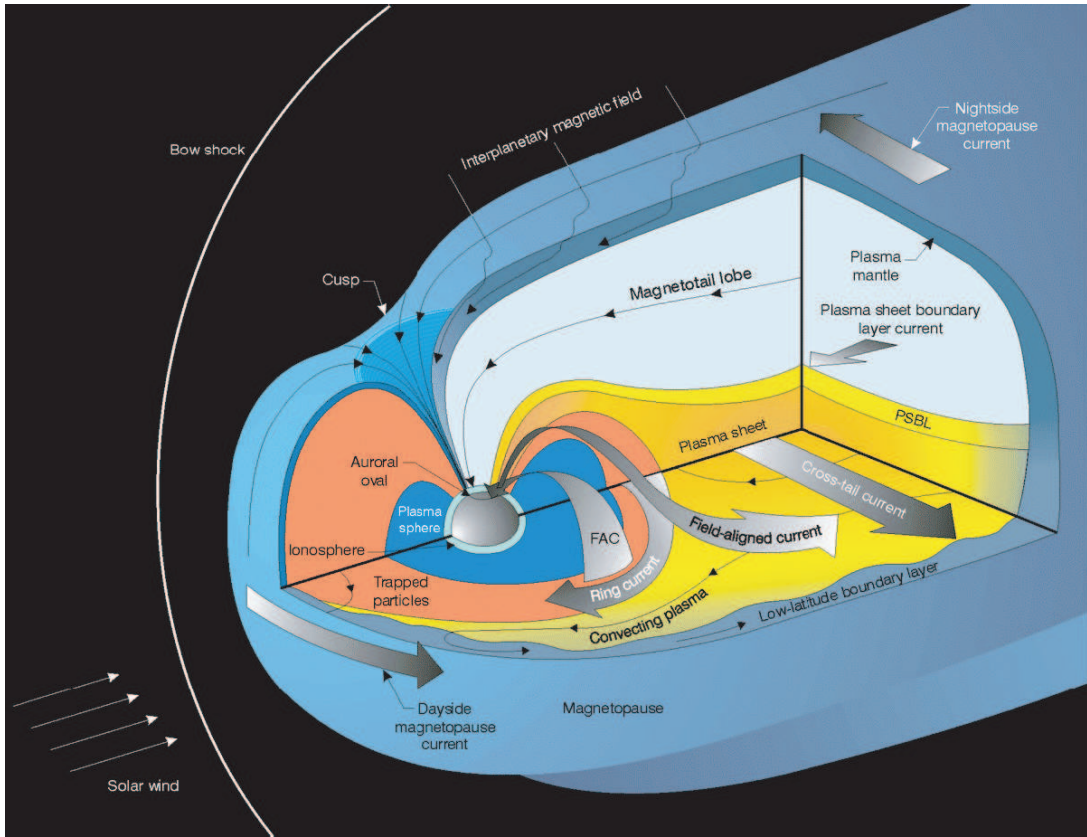


Figure 1.4: Schematic of the magnetosphere showing the main regions and current systems of interest. From *Pollock et al.* [2003].

located in the centre of the tail. The lobes are sparsely populated by plasma, with typical densities of up to 0.1 cm^{-3} , temperatures in the eV range [*Kivelson and Russell, 1995*] and magnetic field values of approximately 40 nT at around $15 R_E$ downtail, decreasing in strength with increased distance downtail [*Fairfield and Jones, 1996*]. The magnetic field lines within the lobes have their footprints on the Earth within the auroral ovals at one end and in the solar wind at the other end and are said to be ‘open’. The plasma within the lobes is of mixed origin, from the ionosphere and solar wind.

The plasma sheet is comparably hotter and denser than the lobes, with typical densities up to 1.0 cm^{-3} and temperatures in the keV range [*Kivelson and Russell, 1995*]. The footprints of the magnetic field lines in the inner plasma sheet are

in both hemispheres of the Earth and are said to be ‘closed’. The magnetic field within this region is lower than in the lobes in order for pressure balance between the lobes (mainly magnetic pressure) and the plasma sheet (mainly plasma pressure) to exist. Between the plasma sheet and lobes exists the PSBL. This region has typical plasma parameters in between the lobe and plasma sheet.

The cross-tail current sheet, or neutral sheet is located in the centre of the plasma sheet. The cross-tail current sheet is directed dawn-to-dusk and exists because of the oppositely directed magnetic field directions in the lobes. The magnetospheric lobes and current sheet will be the main focus of this thesis and are discussed in detail in Chapter 2.

1.1.3.4 Geomagnetic disturbances: Substorms and magnetic storms

The three studies described in this thesis will compare how the magnetotail responds to varying levels of geomagnetic activity, in the form of substorms and storms. Magnetic storms and substorms are the result of strong coupling between the solar wind and the magnetosphere. For a ‘closed’ magnetosphere the solar wind and IMF are separate from the magnetosphere. However during times of southward IMF, the two systems interact when magnetic reconnection occurs on the dayside [Dungey, 1961]. This is shown in Figure 1.5 taken from *Milan et al.* [2003]. Dayside reconnection at (a) joins IMF and magnetospheric field lines, which are then swept tailward by the flow of the solar wind (b and c). There they form the magnetotail (d) and as the magnetic field in the lobes increases, lines of oppositely directed magnetic field converge resulting in magnetic reconnection in the plasma sheet (e). Plasma is then pushed Earthward (f), although there is also a plasmoid formed that is pushed tailward and into the solar wind. The whole process continues (g) whilst the solar wind conditions remain in this configuration. The process is described as the Dungey cycle. The succession of reconnection on the dayside and in the magnetotail, forcing plasma towards the Earth describes a ‘substorm’

[Akasofu, 1964]. This results in visual auroral displays in the Earth's ionosphere, as excited charged particles from the reconnection process collide with atmospheric particles, releasing energy in the form of the aurora.

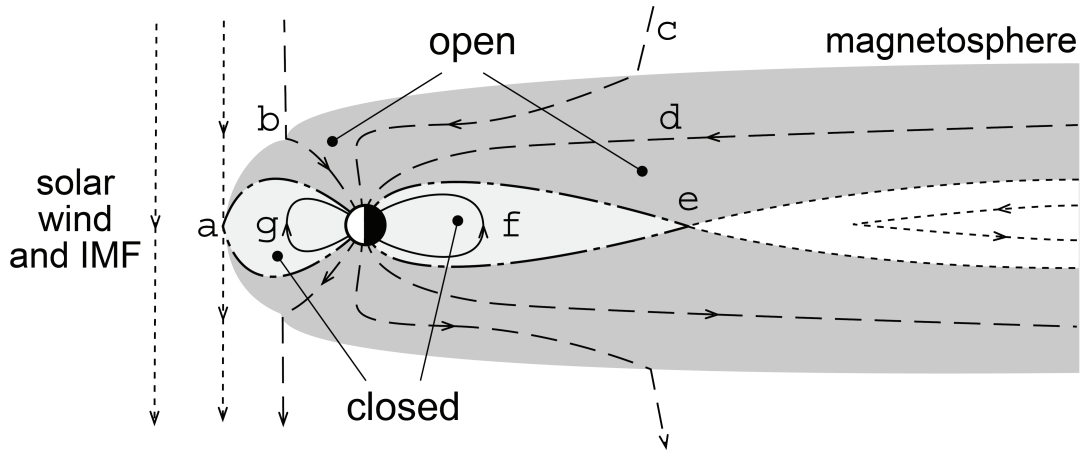


Figure 1.5: A schematic of the magnetosphere in the noon-midnight meridian, undergoing dayside and nightside reconnection, following the Dungey cycle. Taken from *Milan et al.* [2003].

Magnetic storms occur during prolonged southward IMF and result in an enhancement of the ring current. The causes of magnetic storms can be generally divided into those resulting from CME's and those from CIR's, discussed earlier. Storms have 3 main phases: the initial phase, main phase and recovery phase [Gonzalez et al., 1994]. The initial phase (lasting minutes to hours) is caused by the compression of the dayside magnetosphere by the solar wind. This increases the magnetic field near Earth on the dayside. The main phase (lasting up to a few hours) involves a decrease in the magnetic field near Earth on the nightside, caused by the enhancement in the ring current. The recovery phase describes the time it takes for conditions to return to baseline levels and it can take up to several days for the ring current ions to go through various loss processes. Storms can be categorised depending on their strength, in terms of the Dst or SYM-H index, which

are measured by ground-based magnetometers, discussed in Chapter 3. Intense storms have been described as having $D_{st} < -100\text{nT}$, moderate as $< -50\text{nT}$ and small as $< -30\text{nT}$ [Gonzalez *et al.*, 1994]. An example of a magnetic storm, indicated by a variation in the Dst index, is shown in Figure 1.6, from a storm on July 12-16 1982, taken from Gonzalez *et al.* [1994]. The increase in the Dst index of the initial phase can be seen before the Dst becomes negative, in the main phase of the storm, reaching less than -300 nT . The recovery phase in this example only lasts for a few hours.

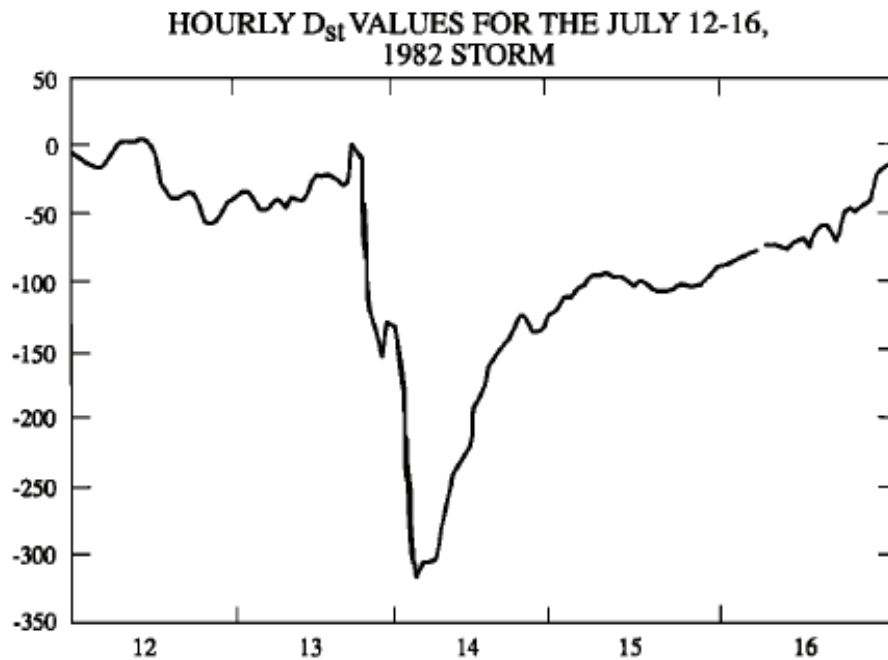


Figure 1.6: An example of Dst data for a magnetic storm on July 12-16 1982, taken from Gonzalez *et al.* [1994].

The phases of magnetic storms can vary depending on the cause of the storm. CME-type storms often have a rapid onset and a ‘sudden storm commencement’ where the ram pressure within the solar wind increases suddenly and hits the magnetosphere, causing the temporary increase in the geomagnetic field. In comparison CIR events often start gradually and do not involve a sudden impulse in pressure. CIR storms are often less intense during the main phase compared to CME storms

and frequently take longer to recover than CME events [*Tsurutani et al.*, 2006].

This thesis is concerned with the cross-tail current sheet and lobes of the magnetotail and how they behave during quiet times, substorms and magnetic storms. Chapter 2 will describe the current sheet and lobes in more detail, summarising the previous research related to these regions. Chapter 3 then introduces the data used in the research and the instrumentation employed. It also summarises some of the analysis techniques used. Chapter 4 is the first data study within the thesis, which focuses on the dynamics of the cross-tail current sheet and how this may be affected by varying geomagnetic activity. The second study, described in Chapter 5, considers the current sheet structure, in terms of its orientation, current density and thickness, again in relation to geomagnetic events. The final study, discussed in Chapter 6 completes the picture, by summarising how geomagnetic activity affects the lobe magnetic field and relates the results back to the earlier studies. The final chapter (Chapter 7) summarises the three research studies undertaken and proposes areas of research that could be undertaken to progress the work further.

Chapter 2

The Earth's magnetotail

The Earth's magnetotail, described in brief in Section 1.1.3.3 of Chapter 1, plays an important role in both substorms and magnetic storms as it is the region that stores energy for those processes as well as the region that initiates the release of the energy towards the Earth. An overview of the main structure of the tail and current systems will be provided first, together with a summary of the more general changes in the magnetotail due to certain geomagnetic events. Finally, this chapter will pay particular attention to the cross-tail current sheet and lobes of the magnetotail, which are the main areas of study in this thesis, and how these may be affected by changes in geomagnetic activity.

2.1 The general size and structure of the magnetotail

The magnetotail has long been defined as a dual lobe tail, reaching out into the solar wind (review by *Ness* [1987]). Figure 2.1 is a diagram of the Earth's magnetosphere in the XZ plane, based on a schematic from *Milan* [2009], showing the tail on the nightside of the Earth and the associated magnetic field lines and some

of the current systems within the magnetosphere. The tail is formed from dayside reconnection of geomagnetic field lines and the transfer of those lines to the night-side of the Earth [Dungey, 1961] as discussed in Section 1.1.3.4. Dungey [1965] estimated the tail length to be of the order of $1000 R_E$, and it has been observed out as far as $80 R_E$ by the IMP D satellite in 1966 and also by the Pioneers 7 and 8 spacecraft, which crossed the tail at $500 R_E$ and $1000 R_E$ [Ness [1987], Ness *et al.* [1967]]. The tail was also observed at about $3000 R_E$ by the Pioneer 7 spacecraft in 1977 [Intriligator *et al.*, 1979].

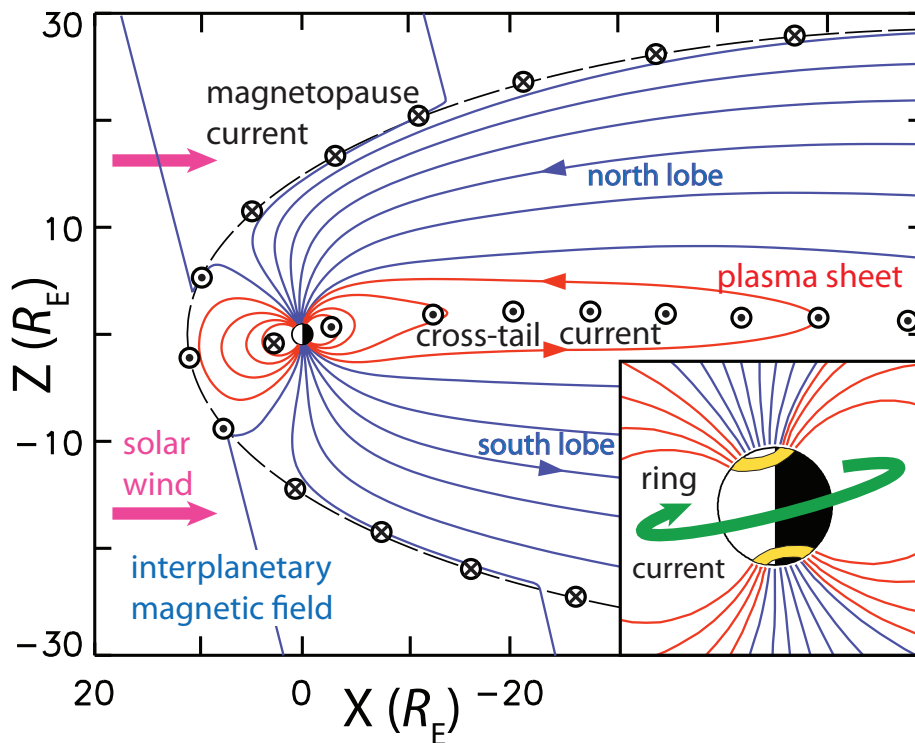


Figure 2.1: A schematic of the Earth's magnetosphere, based on a figure from Milan [2009].

As will be discussed in the following sections, the magnetotail structure changes with external and internal influences and this may have an effect on the length of the tail. In view of this, Oberc [1983] inferred a tail length of about $6000 R_E$ after a protracted time period of quiet conditions. He also argued that the tail

could become as short as about $600 R_E$ after a series of strong substorms. *Milan et al.* [2004] also studied how the tail length might vary during substorms and their calculations suggested that the tail length reduced by a factor of 10 within an 8-hour period (from $4000 R_E$ to $400 R_E$). They found it was at its smallest value after periods of rapid tail reconnection after substorm onset. A summary of the observations and calculated lengths of the tail are summarised in panel (a) of Figure 2.2.

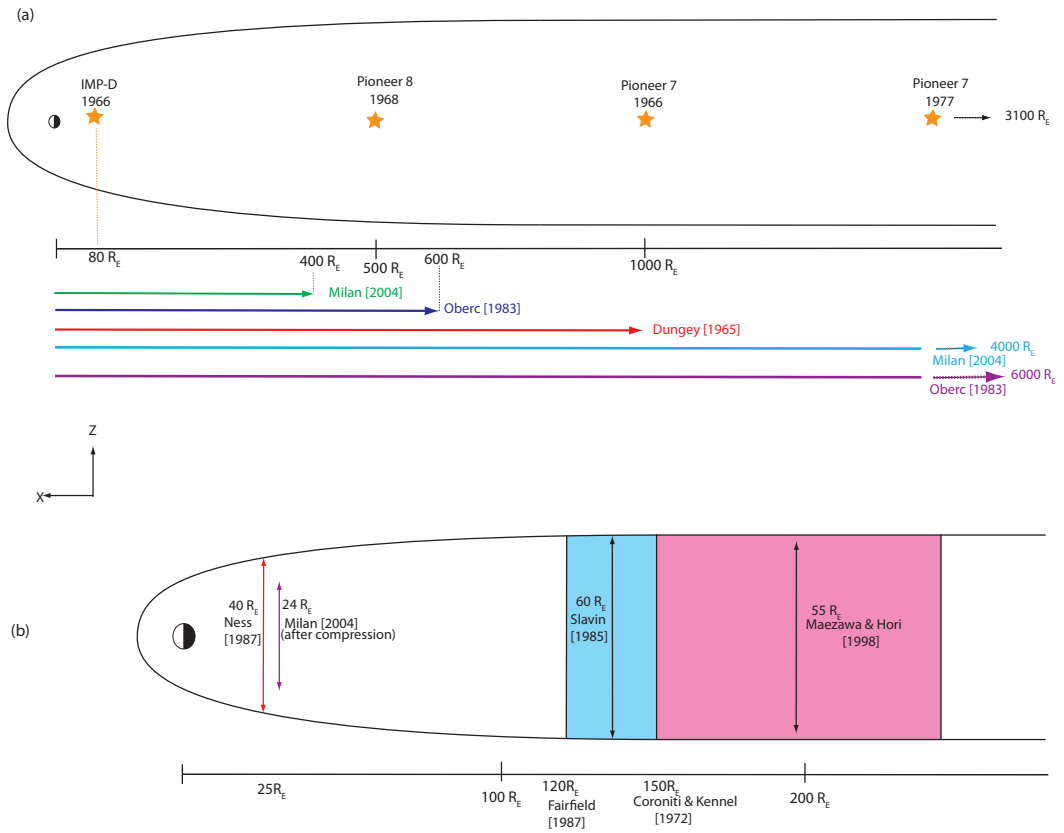


Figure 2.2: A summary of some of the previous research related to magnetotail length (panel a) and diameter (panel b) in the XZ plane.

The angle between the solar wind velocity and the magnetopause surface on the dayside is large and on the nightside it reduces with larger downtail distances. There comes a point where the angle becomes zero and the radius of the tail is constant. This point occurs between about $120 R_E$ [Fairfield, 1987] and $150 R_E$

downtail [*Coroniti and Kennel, 1972*], where the radius stabilises at an estimate of about $30 R_E$ [*Slavin et al. [1985]* and review by *Fairfield [1987]*]. Later estimates using the GEOTAIL spacecraft were of a tail diameter of $55 R_E$ between 150 to $220 R_E$ downtail [*Maezawa and Hori, 1998*]. Further towards the Earth, the IMP 1 satellite measured the diameter of the tail of about $40 R_E$ at $20 R_E$ downtail [*Ness, 1987*]. In contrast, *Milan et al. [2004]* proposed that the tail radius would be as small as $12 R_E$ at about $25 R_E$ downtail in the X direction, following the closure of the majority of open flux in the tail after a solar wind dynamic pressure compression of the magnetosphere. A summary of some of the previous research related to tail diameter is shown in panel (b) of Figure 2.2. As with the length of the tail, the diameter will also adapt to pressure from the variable solar wind. The tail flares during periods of dayside reconnection, as discussed in Section 2.3.

2.2 Currents in the magnetotail

There are 4 main current systems within the magnetosphere, including the tail current, which is the main focus of this work. The currents are not independent of each other and so a brief explanation of their interaction is necessary. Current sheets exist in the magnetosphere where the magnetic field changes in strength or direction over a small distance in comparison to the other length scales within the system. Ampère’s Law (Equation 1.5) states that a current must exist under these conditions. In addition, consideration of the frozen-in flux concept, described in Section 1.1.2.1 of Chapter 1, also means that the current sheets must exist when two different regions of plasma meet but cannot mix.

The main currents within the magnetosphere are shown in Figure 2.3. The magnetopause current (or Chapman-Ferraro current) exists at the boundary between the Earth’s magnetic field and the impeding solar wind and is a result of the Lorentz force acting on the ions and electrons at the boundary. The ions and elec-

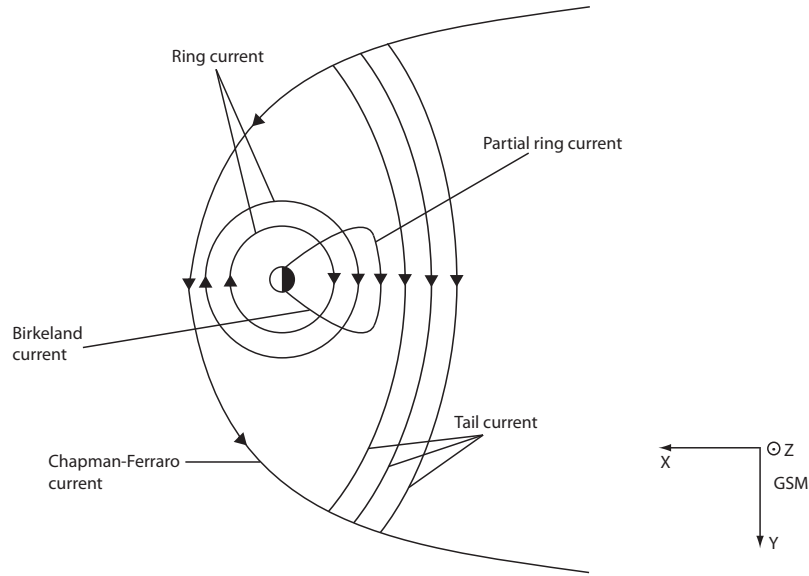


Figure 2.3: The main magnetospheric currents. Based on a figure from *Kivelson and Russell* [1995].

trons respond to the Lorentz force and move a half-gyration in opposite directions, resulting in a dawn-to-dusk magnetopause current. The magnetopause current connects over the lobes to the tail current. The tail current, also in a dawn-to-dusk direction, is implied due to the stretched out and oppositely-directed magnetic field lines of the magnetotail lobes and is described in more detail in Section 2.4. The ring current in the inner magnetosphere is a clockwise flow around the Earth and is due to the drift of trapped particles (Section 1.1.1.2) that have been injected into the inner magnetosphere via convection processes such as those that occur during magnetic storms and substorms. The ring current is generally located at around $4-6 R_E$, near to the inner edge of the plasma sheet [Hargreaves, 1995]. Finally Birkeland or field-aligned currents connect the partial ring current (a dawn-dusk current in the equatorial plane) to the ionosphere. Within the ionosphere, Pedersen and Hall currents are present as a result of magnetospheric convection. Pedersen currents are closed through the field-aligned current system. The Hall currents within the auroral oval are known as the electrojets and an index measuring these

is discussed in Section 3.3.2.

The magnetospheric current systems are dependent on solar wind conditions and some of the results of this will be discussed in the next section. Of specific importance to this thesis, changes in the ring current and magnetopause current can be observed in ground-based data, described in Chapter 3.

2.3 Overview of the response of the tail to geomagnetic activity

As discussed briefly in Chapter 1, the magnetotail is formed due to the constant bombardment of the solar wind on the Earth's geomagnetic field. The magnetosphere is often described in a static way, at a particular moment in time, and this is due to the fact that it is constantly changing and responding to both external and internal influences. It is a system of varying plasma regions with their associated magnetic field and current systems. Changes in solar wind parameters are translated into complex changes within the magnetosphere and whilst it would be impossible to describe all the permutations of each regional change here, some of the general changes caused by the solar wind are discussed.

The dynamic pressure of the solar wind is,

$$P_D = \rho_{sw} u_{sw}^2 \quad (2.1)$$

where ρ_{sw} is the solar wind density and u_{sw} is the solar wind speed. It has been shown that an increase in solar wind dynamic pressure, causes a compression of the magnetosphere, at the dayside magnetopause and in the magnetotail [Wilken *et al.* [1982], Russell *et al.* [1999], Li *et al.* [2011]]. In fact, the near-Earth magnetotail is extremely responsive to changes in the solar wind dynamic pressure when it is

in a compressed state [Li *et al.*, 2011]. An increase in dynamic pressure causes an increase in the geomagnetic field on the dayside of the Earth and a movement of the magnetopause towards the Earth [Wilken *et al.*, 1982]. In January 1997, several solar wind density enhancements were observed while other solar wind parameters remained constant. As a result, Shue and Kamide [2001] found that increases in solar wind density caused an increase in auroral electrojets.

More specifically, the tail responds to substorms and magnetic storms in certain ways. During substorms, the circulation of plasma in the magnetosphere is driven by the impact of the solar wind on the day-side of the Earth and reconnection at the magnetopause. However the circulation will only continue if there is also reconnection in the magnetotail, specifically in the central plasma sheet [Hargreaves, 1995]. If there is a steady state of reconnection on both sides of the Earth, then open and closed flux are formed at an equal rate on either side of the Earth. However, the process of dayside and nightside reconnection is often variable and intermittent, and at these times an imbalance will be present [Milan *et al.*, 2003]. As the IMF turns southward, the rate of reconnection on the dayside is larger than the nightside for a time, as more open flux is being produced and dragged anti-sunward, forming the magnetotail lobes and causing the magnetotail to flare [Coroniti and Kennel, 1972]. At the same time the lobe magnetic field and tail current increase and the inner edge of the latter moves Earthward [Fairfield and Ness, 1970]. In addition, the auroral oval moves equatorward. This is the growth phase of the substorm where there is an erosion of closed magnetic flux on the day-side of the Earth and a storage of energy in the magnetotail. During the growth phase, the plasma sheet thins due to the increased pressure from the open flux of the lobes [Hargreaves, 1995].

Following reconnection in the tail, energy release occurs at the onset of the expansion phase of the substorm where plasma is pushed towards the Earth. The cross-tail current then reduces and a part is diverted along the field-aligned current

system (Birkeland currents) into the ionosphere. Enhancement of the Hall currents in the auroral oval occur and can be measured with the AE index, which is discussed in Section 3.3.2. Some of the particles ejected Earthwards during this phase are trapped in the ring current, although some of this is a partial ring current that does not fully encircle the Earth. As open flux is closed in the tail, the field strength in the lobes and the flaring angle both reduce and the plasma sheet thickens. The final phase of the substorm, the recovery phase, is where all regions return to a more neutral state, unless changes in the solar wind impose further processes to be initiated.

Since substorms are frequently still occurring during magnetic storms [Maltsev, 2004], one might assume that the magnetotail responds in a similar way to storms as it does to substorms. One of the main differences is the enhancement of the ring current. For prolonged events such as magnetic storms, the trapped particles from extended magnetospheric convection result in an enhanced ring current. As a consequence of this, the geomagnetic field is depressed and can be measured by ground-based equipment, discussed in Chapter 3.

The different impacts on the magnetotail of storms and substorms were investigated by *Miyashita et al.* [2006] who studied the effect of substorm expansion onsets on the tail, comparing non-storm times to storm times using GEOTAIL data. They studied the near- to mid-tail region at $-5 \geq X \geq -31 R_E$. They demonstrated that the changes within the magnetotail during storm time substorms were similar to non-storm times, in terms of parameters such as temperature, total pressure and electric field, although the effects were larger. Like other studies on storms and the tail, they were unable to study the different phases of storm separately, due to the small numbers of storms and so it is unclear what differences exist when comparing main phases of storms to recovery phases, particularly any differences that exist with similar values of the Dst or SYM-H indices.

The stormtime central plasma sheet between 10-30 R_E was studied (using GEO-

TAIL data) by *Schödel et al.* [2002] who found that the average conditions during the recovery phase of a storm were similar to quiet times ($Dst > -25$ nT) with the exception of the ion temperature. They concluded that the central plasma sheet recovers quickly to its quiet state during the recovery of a storm, although the high ion temperature during recovery points to trapped energetic ions, only losing their energy gradually.

Nakamura and Kokubun [2000] studied the distant tail (83-210 R_E downtail) using GEOTAIL data and found that the tail is compressed during the initial phase of a storm whereas during the main phase, the average diameter is similar to that at quiet times, although the flux is enhanced. They also found that in the recovery phase, the radius of the tail in this region returns close to quiet values.

It is therefore clear that changes in the solar wind conditions have an effect on all regions of the magnetotail and at varying distances downtail. The previous research specifically related to the cross-tail current sheet will be discussed in the next section.

2.4 The cross-tail current sheet

The cross-tail current sheet, described in Section 2.2 is the main focus of this thesis. Its variability in terms of dynamics and structure will be discussed in the following sections.

2.4.1 Current sheet motion

There is evidence that the current sheet is a dynamic region. Its motion is often described as a flapping movement in a North-South direction [*Speiser and Ness*, 1967], either from the centre of the tail propagating out towards the flanks (e.g. *Lui et al.* [1978]; *Nakagawa and Nishida* [1989]) or in a direction along the tail

(e.g. *Speiser* [1973]). The cause of this current sheet motion is unknown, although two explanations have been investigated in the literature. The propagation of the motion from the centre of the tail towards the flanks may indicate that it is initiated in the centre of the tail within the current sheet and caused by some internal mechanism, for example substorm activity (e.g. *Sergeev et al.* [2004]). External influences have also been studied, investigating how changes in the solar wind dynamic pressure may affect the current sheet motion (e.g. *Forsyth et al.* [2009]).

Zhang et al. [2005] investigated a series of spacecraft crossings of the current sheet on 5 August 2004, shown in Figure 2.4. They found that the crossings were due to a kink-like wave which propagated within the current sheet from the centre of the tail towards the flanks, shown in Figure 2.5. They viewed this wave at two positions in the tail, at X GSE = -11 Earth Radii (R_E) and -16 R_E , using Double Star (TC-1 Satellite) and Cluster observations respectively. They estimated that the wave amplitude was 0.6-1.3 R_E with a wavelength of about 4 R_E . These values are consistent with those obtained by *Runov et al.* [2005a] and *Zhang et al.* [2002].

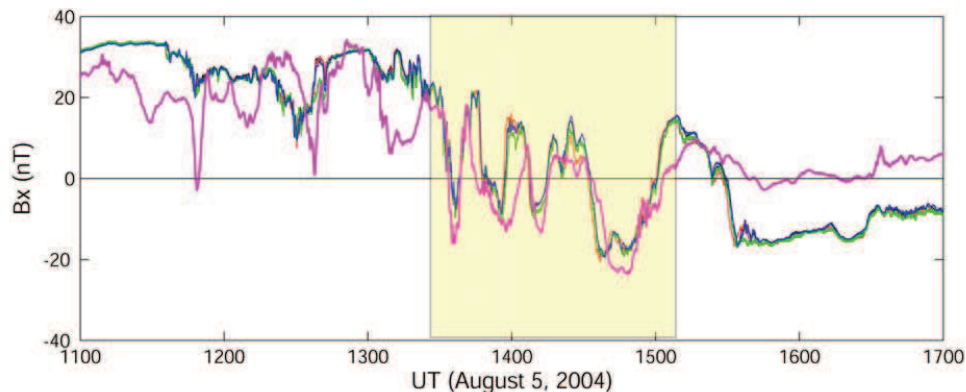


Figure 2.4: The current sheet crossings studied by *Zhang et al.* [2005] that occurred 5 August 2004. Data were from the Cluster and TC-1 spacecraft. The pink line indicates TC-1 data and the shaded region indicates the current sheet crossings studied.

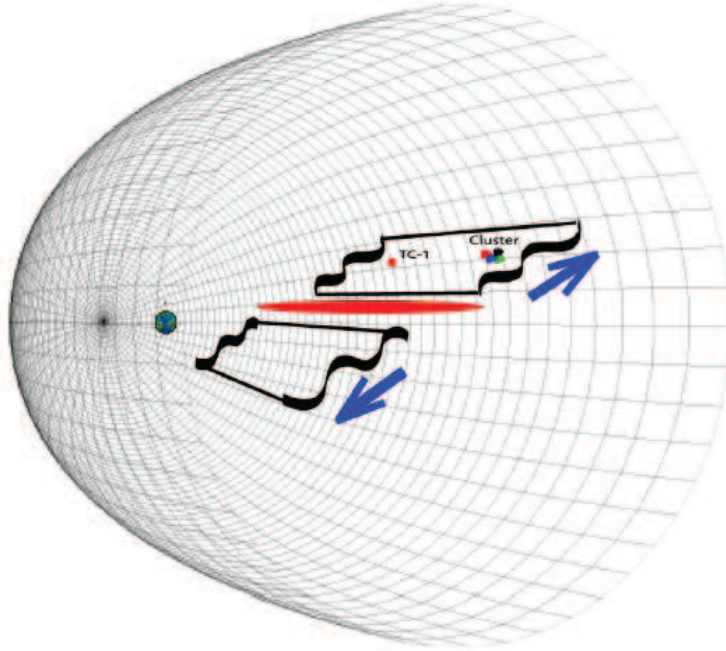


Figure 2.5: A schematic of the current sheet in motion from *Zhang et al.* [2005].

The association between substorm activity and current sheet dynamics was studied by *Bauer et al.* [1995] who found that current sheet motion occurred close to substorm onset. This was confirmed by *Sergeev et al.* [1998]. Later, following the launch of the multi-spacecraft Cluster mission, *Runov et al.* [2006] studied current sheet crossings between July and October 2001. They investigated whether there was any dependence on the structure and thickness of the current sheet with the AE index. No correlation was found, although the dataset was considered too small for a complete analysis. In contrast, *Sergeev et al.* [2006] did find a correlation between substorm expansion phases based on the AE index and flapping motions of the current sheet. They performed a superposed epoch analysis of over 1000 fast crossings between 1997 and 1999, for a timescale of ± 2 hours from the time of the crossing (Figure 2.6). GEOTAIL data was used when it was at distances downtail of 10-30 R_E . *Sergeev et al.* [2006] only used fast crossings ($30 \text{ s} < \Delta t < 300 \text{ s}$) for

the study, and although the expansion phase correlation was found, there were also a significant number of flapping motions when the AE index was low. In addition, they found some evidence that the flapping of the current sheet is related to the occurrence of Bursty Bulk Flows (BBFs). *Milan et al.* [2006] also discussed current sheet motions associated with substorm intensification, during an interval in 2004. *Runov et al.* [2009] observed flapping events in a five hour period in December 2007, using the THEMIS spacecraft, that occurred during substorm growth phases, identified using THEMIS ground-based magnetometers. *Forsyth et al.* [2009] observed current sheet motion which occurred after two substorms following a solar wind pressure pulse. No conclusions could be made regarding the relationship between the motion and substorms due to the presence of a solar wind pulse which caused an oscillation of the plasma sheet.

How the current sheet responds to an enhanced ring current, such as exists during magnetic storms, remains an unanswered question. *Milan et al.* [2008] studied the expansion and contraction of the polar cap in response to variations in the solar wind conditions. They found that the polar cap size (giving an indication of the amount of open flux in the magnetosphere) increases during magnetic storms. Consequently, they suggested that the enhancement of the ring current that occurs during storms may result in an increase in the amount of open magnetotail magnetic flux needed for the commencement of tail reconnection and thus stabilize the tail to substorm initiation. This was also suggested by *Nakai and Kamide* [2003].

2.4.2 Current sheet structure

2.4.2.1 Current sheet tilt

Studies have shown that when the current sheet is active (during flapping motion), it can be highly tilted in the YZ GSM plane and that this tilt is reduced during periods of inactivity when the current sheet is not undergoing flapping motion. For

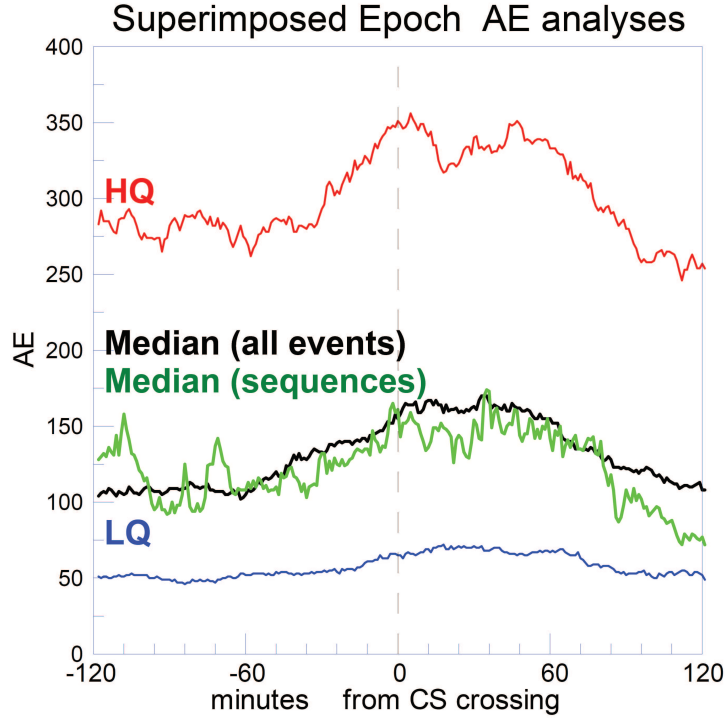


Figure 2.6: The superposed epoch analysis from *Sergeev et al.* [2006], showing the relationship between the AE index and the time of the current sheet crossing.

example, *Zhang et al.* [2002] calculated the inclination angle of the current sheet in the YZ GSM plane using 4 point timing methods for five crossings in 2001 of an active current sheet by Cluster and found that this angle ranged from 41° to over 90° . A further study by *Sergeev et al.* [2003] found large tilt angles of $60\text{-}70^\circ$ in the YZ plane using inter-spacecraft timing and MVA methods. A highly tilted current sheet during flapping motion was also shown by *Sergeev et al.* [2004], where the Z component of the current density measurements was larger than the Y component.

Runov et al. [2005b] noted tilt angles of up to 75° for a series of intervals containing fast crossings due to flapping motion, using Cluster data. In addition, *Runov et al.* [2005a] found in a statistical survey of rapid crossings, that 54 % of the cases studied had tilt angles greater than 45° . Later, *Forsyth et al.* [2009]

used Minimum Variance Analysis and spacecraft timing methods and demonstrated that the Y components of the normal direction to the current sheet were frequently larger than the Z components, indicating a highly tilted current sheet. In general, the aforementioned studies have investigated the current sheet during its flapping motion. In contrast, a statistical study of inactive current sheets during Cluster's 2001-2003 tail seasons by *Petrukovich et al.* [2005] showed lower tilt angles from 0 to 40°. They also found that the tilt of the current sheet increased towards the flanks of the magnetotail, as shown in Figure 2.7.

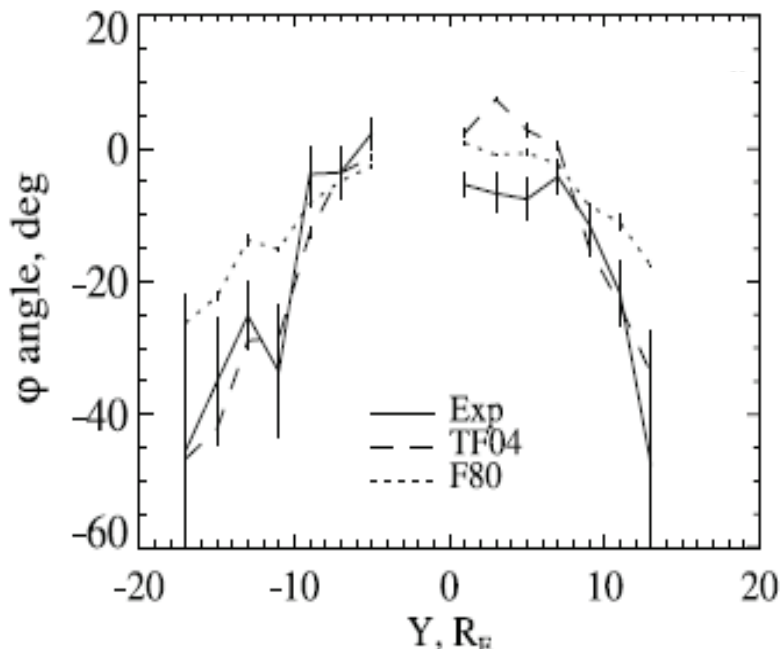


Figure 2.7: The tilt of the current sheet in the YZ plane from *Petrukovich et al.* [2005] for slow monotonic crossings of the current sheet made by the Cluster spacecraft from 2001-2003.

2.4.2.2 Current sheet current density

Observations have shown that the current density in the tail current sheet can range from less than 10 nA m^{-2} [Shen *et al.*, 2008; Sergeev *et al.*, 2003; Rong *et al.*, 2011] to values as high as 30 nA m^{-2} [Runov *et al.*, 2005b, 2006]. Forsyth *et al.* [2009] made current density estimates for 5 crossings of the current sheet on 3 August 2001, which ranged from 9-18 nA m^{-2} , using the curlometer technique. In their study of a series of intervals containing fast crossings, Runov *et al.* [2005b] estimated values of current density of up to 30 nA m^{-2} , although much lower values of around 15 nA m^{-2} were also noted. In a separate statistical study, Runov *et al.* [2005a] estimated current density values ranging from less than 5 nA m^{-2} up to 25 nA m^{-2} . Similarly large values of current density were found by Sergeev *et al.* [1998] of $10\text{-}30 \text{ nA m}^{-2}$ using AMPTE/IRM satellite data. In a later study, Runov *et al.* [2006] estimated current densities for 30 crossings, with maximum current densities within the crossings as low as 3 nA m^{-2} up to 25 nA m^{-2} , for rapid current sheet crossings. A superposed epoch analysis of 21 substorm onsets performed by Thompson *et al.* [2005] demonstrated an increase in current density (to a median value of $J_Y \approx 3 \text{ nA m}^{-2}$) during the growth phase of a substorm, followed by a decrease after onset and into the recovery phase (Figure 2.8). No comparison of storm-time substorms and non-storm-time substorms was made in this study. The results are consistent with more open flux in the tail in the growth phase of a substorm compared to quiet times. A case study of a current sheet flapping under substorm conditions was investigated by Nakamura *et al.* [2006] who found current density estimates of the order of $50\text{-}100 \text{ nA m}^{-2}$ using a spacecraft separation of $0.03 R_E$. Comparing these studies indicates that the current density can vary within an order of magnitude for ‘similar’ events, but large tilt angles have been observed when the sheet is active (flapping).

In contrast, Zhang *et al.* [2006] studied slow crossings of the current sheet and performed a superposed epoch analysis on Cluster data from 2001 and 2002. Their

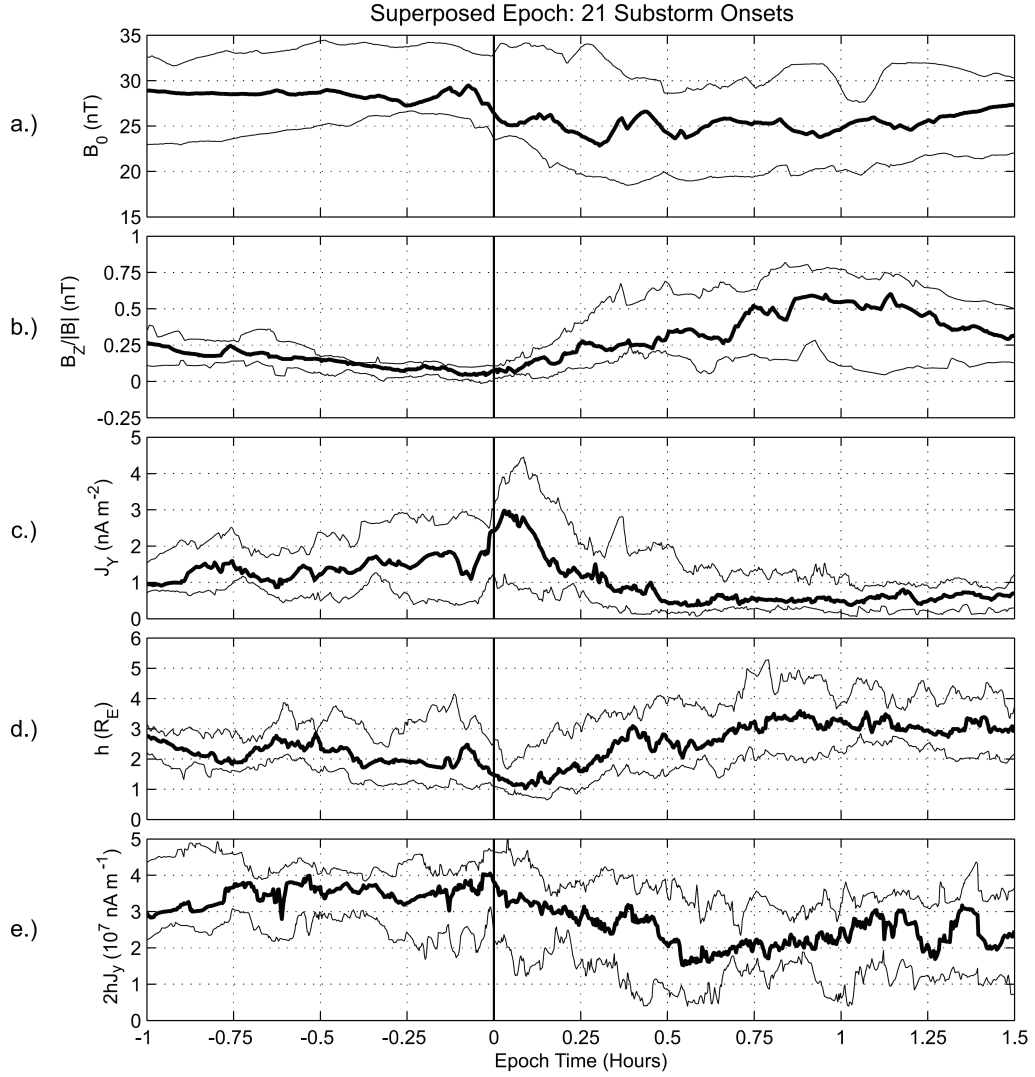


Figure 2.8: The superposed epoch analysis by *Thompson et al.* [2005] of 21 substorms from Cluster’s 2001 and 2002 tail seasons. Of particular relevance to this thesis work are panels (c) and (d) showing the Y-component of the current density and the half thickness, respectively. The thicker lines indicate the median values and the thinner lines indicate the upper and lower quartiles.

current density vertical profile is shown in Figure 2.9 with a peak at 2.7 nA/m^2 .

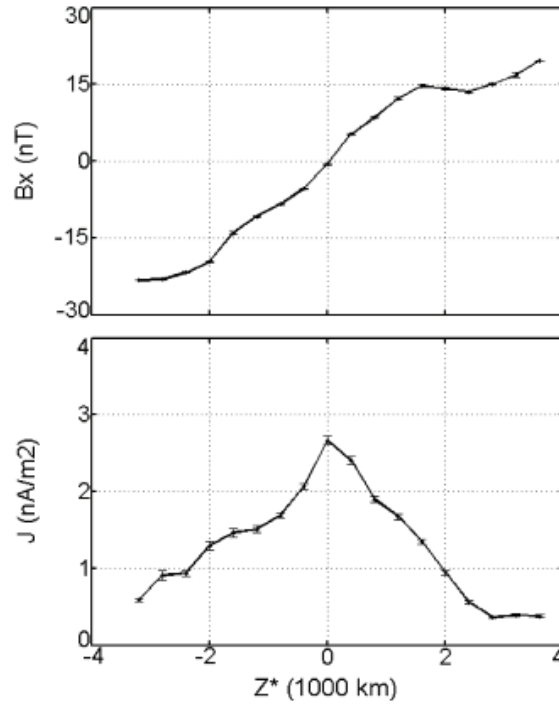


Figure 2.9: The current sheet crossings studied by *Zhang et al.* [2006] that occurred in 2001 and 2002. The data are shown in terms of an averaged vertical current density profile for all crossings.

2.4.2.3 Current sheet profile and thickness

As well as varying in orientation and current density, the current sheet has been shown to have different structures of varying scales. *Runov et al.* [2006] separated out current sheet crossings in terms of the current density profile, into 3 distinct groups: centre peaked (class I), bifurcated (class II) and asymmetric (class III). Their averaged vertical current density profiles are shown in Figure 2.10 for each class of structure. The half thicknesses of the classes of current sheet were estimated to be less than $0.3 R_E$ for class I and III current sheets with about $0.6 R_E$ for class II sheets. It should be noted that their data only considered fast crossings (less than 5 minute duration) of the current sheet. In a study of nearly 6000 crossings

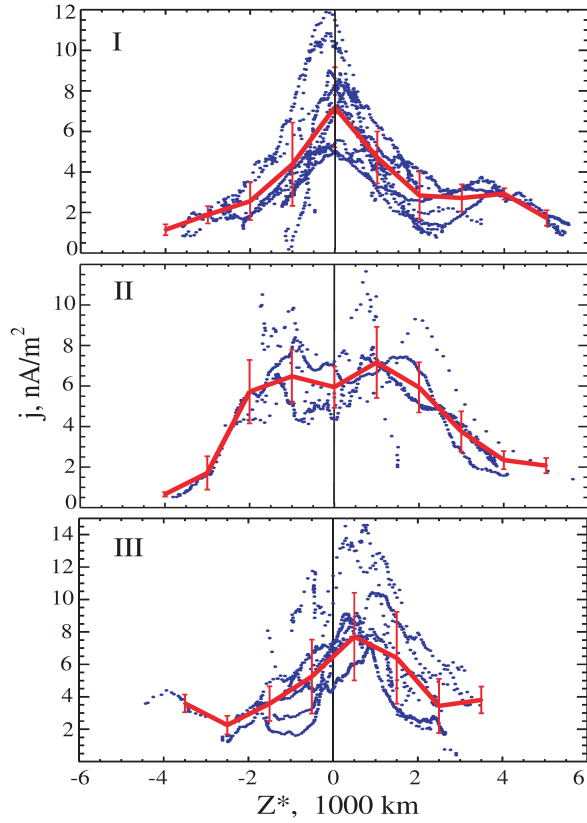


Figure 2.10: The current sheet crossings studied by *Runov et al.* [2006] that occurred between July and October 2001. The data have been averaged and are shown in terms of vertical current density profiles for the three classes of structure as defined by *Runov et al.* [2006]: centre peaked (I), bifurcated (II) and asymmetric (III).

undertaken by *Rong et al.* [2011], the range of half thicknesses calculated in the central tail region (at low Y values) was $0.2-0.4 R_E$ compared to $0.7-1.6 R_E$ at the flanks. No analysis of geomagnetic activity was made in this study.

Sergeev et al. [2006] also considered fast crossings ($30 \text{ s} < \Delta t < 300 \text{ s}$) over a downtail distance of $10-30 R_E$ using GEOTAIL data and found that the half thickness of the current sheet ranged from less than $0.4 R_E$ to $3.6 R_E$ with most values between $0.4-1.2 R_E$. These are in agreement with *Sergeev et al.* [1998] who measured values of $0.2-1 R_E$. Similar values of half thickness were obtained by *Forsyth et al.* [2009] with values that ranged from less than $0.5 R_E$ to $1.8 R_E$ for a

series of crossings on 3 August 2001, with 1 out of 5 having a bifurcated structure. Estimations of half thickness in a superposed epoch study by *Thompson et al.* [2005] varied during the phases of a substorm, with values of $\sim 1.8\text{-}2.6 R_E$ in the growth phase, decreasing to $\sim 1 R_E$ after onset and then increasing to $\sim 3 R_E$ in the recovery phase.

2.5 The magnetotail lobes

The current sheet is directly related to the lobe magnetic field by Ampère's Law (Equation 1.5). The following section will discuss how the lobe field varies with increasing distance downtail and also with different geomagnetic events.

In his review of magnetotail research, *Ness* [1987] noted that the IMP 1 satellite observed average lobe magnetic field values of 16 nT at a $20 R_E$ distance downtail. Research by *Caan et al.* [1975] using data from the Ogo 5 spacecraft at a distance downtail of between 9 and $19 R_E$, studied the differences in the lobe magnetic field during substorms and changes in the IMF. They found that the lobe field was enhanced during the southward IMF phase, with a decrease in the lobe field at the onset of substorm expansion. Later *Slavin et al.* [1985] compared average conditions to substorm conditions in the distant magnetotail using ISEE 3 data. They found that the lobe magnetic field under average conditions was about 15 nT at $50 R_E$ downtail reducing to about 9 nT at $120 R_E$ downtail and remaining relatively constant at larger downtail distances (Figure 2.11). This was represented by a fall in lobe strength with $X^{-0.53 \pm 0.05}$. During substorms (assessed using the AE index), the magnetic field strength in the distant lobes ($|X| < -200 R_E$) was only 1 nT weaker for small AE values (AE < 200 nT) compared to higher AE values (AE > 200 nT). They also found that there was no increase in lobe strength with increasing AE index for the latter group.

In 1991, using data from the ISEE 1 and ISEE 2 spacecraft, *Nakai et al.* [1991]

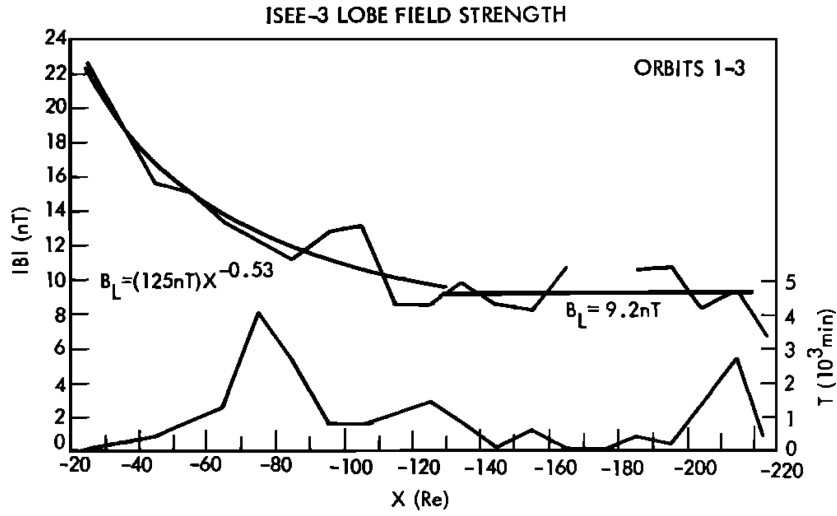


Figure 2.11: Comparison of variation in field strength with distance downtail from *Slavin et al.* [1985] for the first 3 ISEE3 orbits. X refers to the X distance downtail and the right hand side axis relates to the amount of time spent in the lobe with distance downtail.

considered the variation in lobe field strength with distance downtail for the near Earth region of the tail (between 10 R_E and 23 R_E downtail). They found a relationship for the field strength, B of $1030 R^{-1.2}$ nT, where R is the geocentric distance in Earth radii. Their analysis also revealed that the field strength depended on the pressure of the solar wind and the north-south component of the IMF.

A large database of lobe data was studied by *Fairfield and Jones* [1996], using 11 spacecraft over a 20 year period. They compared their relationship of field strength to distance downtail of $1659.2/R^{1.46} + 7.47$ to previous research, shown in Figure 2.12. Their data covered a downtail distance of 15 to 70 R_E . *Fairfield and Jones* [1996] noted, on consideration of the various differences in the methodologies for each of the studies shown in Figure 2.12, that the trends of magnetic field with distance downtail are consistent with each other.

A more detailed representation of the *Fairfield and Jones* [1996] data is shown in

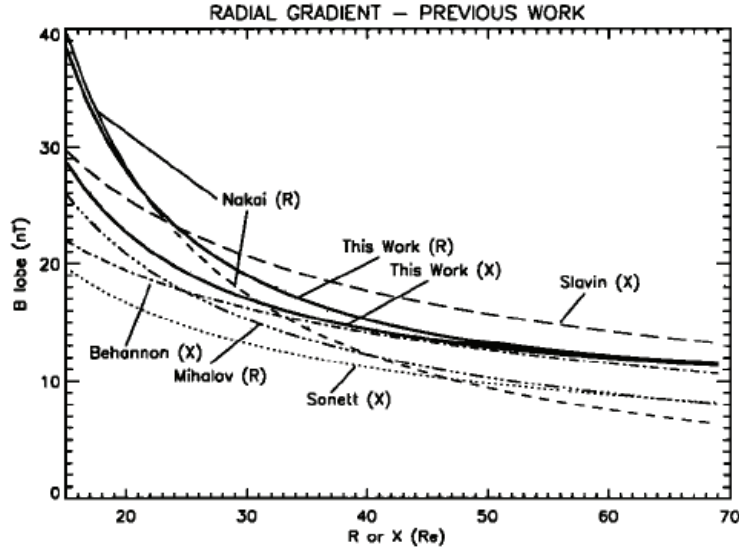


Figure 2.12: Comparison of variation in field strength with distance downtail for previous research, taken from *Fairfield and Jones* [1996]. X or R refers to either the X distance downtail or the radial distance downtail. Nakai data is taken from *Nakai et al.* [1991], Slavin data is taken from *Slavin et al.* [1985], Behannon data is taken from *Behannon* [1968], Mihalov is taken from *Mihalov and Sonett* [1968], and Sonett data is taken from *Sonett et al.* [1971]. ‘This work’ stands for the work carried out by *Fairfield and Jones* [1996].

Figures 2.13 and 2.14. Their analyses also revealed that after normalising the data to a downtail distance of $30 R_E$, long-term variations could be studied, resulting in the conclusion that solar wind dynamic pressure is the primary controlling factor of the lobe field strength. Over two solar cycles were studied and the annual average lobe field strength varied in phase with the dynamic pressure of the solar wind (as found by *Nakai et al.* [1991]) and the AE index.

Later, *Nakai et al.* [1999] studied the near-Earth region ($3\text{-}23 R_E$ downtail) using ISEE 1 data from 1978-1987. They specifically examined the equatorial and lobe regions of the magnetotail. The equatorial region was defined as $|Z| < 5 R_E$ from the average position of the neutral sheet, (in geocentric solar-magnetospheric coordinates), and the lobes were defined as $|Y| < 5 R_E$ and $|Z|$ between 4 and $9 R_E$ from the average position of the neutral sheet. They considered the two regions

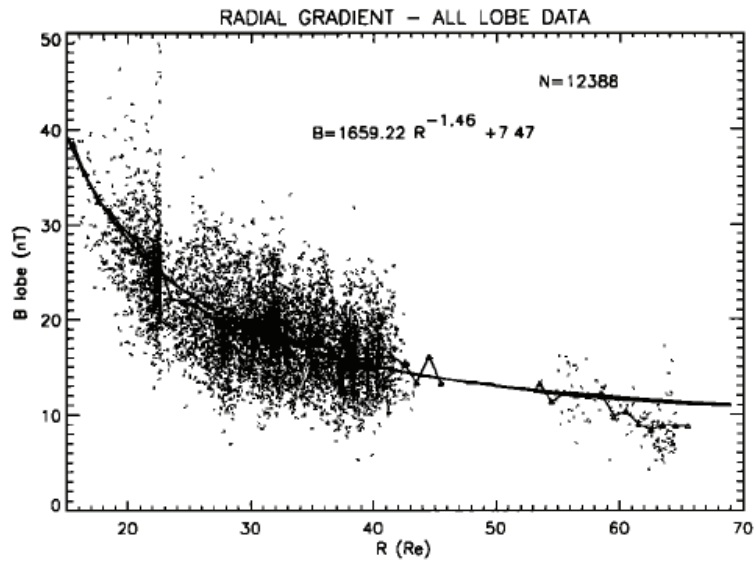


Figure 2.13: Radial variation of the lobe field strength from *Fairfield and Jones* [1996].

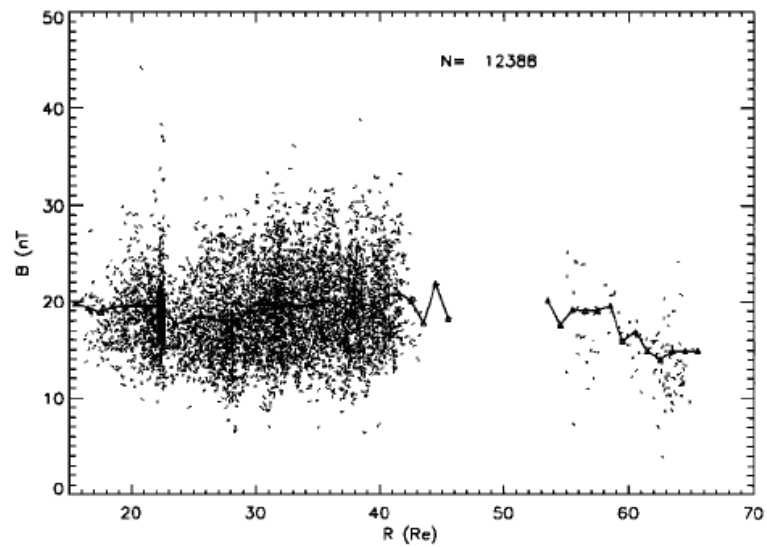


Figure 2.14: Radial variation of the lobe field strength from *Fairfield and Jones* [1996] after normalisation removed the variation with distance.

during substorms and magnetic storms, using the AE and Dst indices. Radial gradients of field strength for the equatorial and lobe regions are shown in Figures 2.15 and 2.16, indicating a similar drop in field strength further from the Earth as

found by the previous authors. The changes with substorm and storm conditions were dependent on the position downtail. Results showed that the equatorial field increased with substorm activity for distances greater than $9 R_E$ downtail and had the opposite effect closer to the Earth. A similar picture was found for storm times, although the critical distance downtail where the change occurred was at $12 R_E$ downtail. The lobe field was found to increase with substorm and storm activity. A study of the effect of an enhanced ring current (using the Dst index) was not possible for $Dst < -45$ nT, at distances closer than $17 R_E$ downtail due to small numbers of data, meaning that only small scale storms were considered.

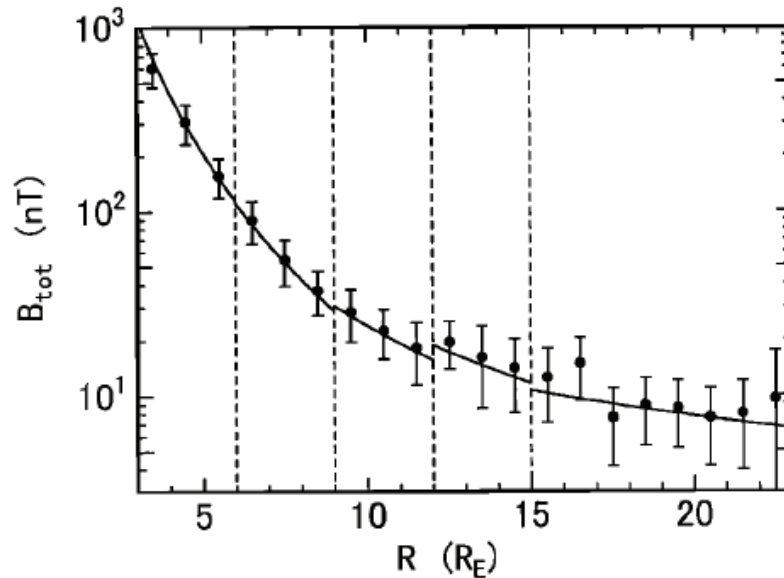


Figure 2.15: Radial variation of the equatorial region field strength from *Nakai et al.* [1999].

The far more distant tail ($\geq 100 R_E$ downtail) was examined by *Nakamura and Kokubun* [2000] using GEOTAIL data during 13 storms between 1993 and 1994. They measured a magnetic field strength of 53 nT during the growth of the ring current, which then reduced during the recovery phase of the storm. They also calculated that the energy stored in the distant tail lobe during the early main phase of storms, was of a similar value to that stored in the mid-tail region during the growth phase of an intense substorm.

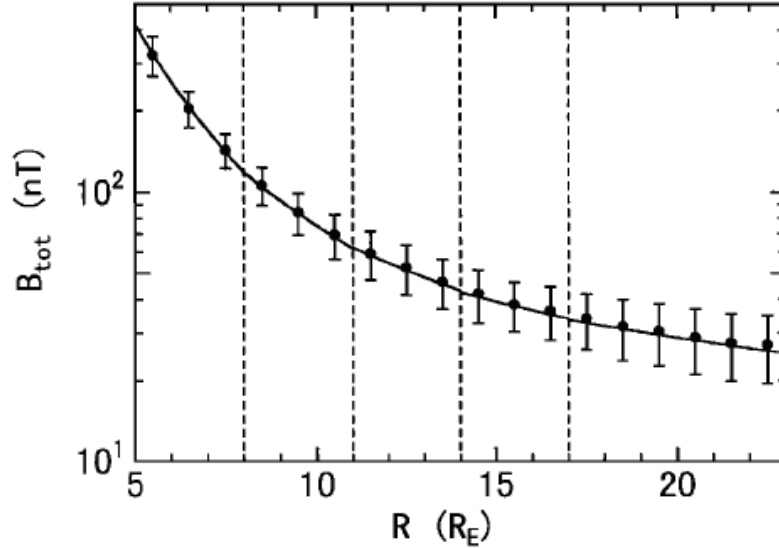


Figure 2.16: Radial variation of the lobe field strength from *Nakai et al.* [1999].

Returning to the near-Earth region, *Miyashita et al.* [2005] used GEOTAIL data to study the 30 October 2003 storm, which coincided with numerous intense substorms. GEOTAIL was located at about $8 R_E$ downtail and measured larger magnetic field values than are usually obtained at this distance, of 50-200 nT. The size of the storm reached a Dst level of -400 nT and one of the most intense substorms during the event caused the westward electrojet to reach -4000 nT.

2.6 Research questions

Observations have shown that the magnetotail varies with both external and internal influences at a large range of distances downtail as well as within the different regions of the tail. This thesis will consider the dynamics and structure of the cross-tail current sheet as well as the lobes. Previous research, as discussed in Section 2.4.1 has shown that the current sheet can move in a flapping motion, although no consistent link with substorms or magnetic storms has been shown. Although

Milan et al. [2008] proposed that storms cause a stabilisation of the magnetotail to substorm initiation, the question of whether the current sheet motion is stabilised under storm conditions is an unanswered question. As such the first results chapter (Chapter 4) will describe a study that investigates the motion of the current sheet in a global context. It considers orbits of the Cluster 3 spacecraft through the magnetotail and studies the overall effects of substorms on the dynamics of the current sheet, rather than focusing on the small-scale changes within each crossing of the current sheet. The Cluster spacecraft enable an investigation of these effects due to their orbit passing through the mid region of the magnetotail, which is of significance in substorm processes. They also provide data of successive passes through the current sheet, enabling a study of its vertical motion. The study focuses on the number of current sheet crossings made by the Cluster 3 spacecraft for each orbit through the magnetotail as a measure of the dynamic nature of the tail during each orbit. The auroral electrojet index is employed as a measure of substorm occurrence, for the period of time that the crossings occur. In addition SYM-H data is used to investigate whether magnetic storms have a similar stabilising effect on the motion of the current sheet as they do to substorm initiation.

The wide range of current density estimates of the tail current sheet discussed earlier have not shown a dependence on substorm or storm activity. In addition, whilst the studies mentioned have shown that the current sheet tilt is highly variable, there has been no systematic study of which factors may affect the variation. These issues are addressed in Chapter 5, using data from the four Cluster spacecraft during crossings of the current sheet made between 2001 and 2007.

Whilst the lobe field has been studied at various distances downtail during substorms and magnetic storms, the relationship between the lobe field and the AE and storm indices has differed. *Slavin et al.* [1985] did not find a relationship between the AE index and the lobe field in the distant tail area, whereas *Nakai et al.* [1999] did find a correlation with the AE index and the Dst index in the nearer

Earth region, although the radial dependence could not be ascertained at distances closer than $17 R_E$ downtail for moderate or severe storms. Chapter 6 takes this work further and reports a study of the differences between quiet, substorm and storm conditions on the lobe field strength whilst also comparing the results to the conclusions drawn in Chapters 4 and 5.

The three chapters taken together provide more understanding of how the magnetotail responds to substorm and storm conditions and how the tail may be stabilised. The next chapter describes the data used in the studies in this thesis as well as the analysis techniques employed.

Chapter 3

Instrumentation and data analysis

This chapter describes the instruments and data employed in the research studies. The main data used have been from the Cluster spacecraft as well as ground-based magnetometers. The analysis techniques which form part of the analyses in the studies will also be summarised in this chapter.

3.1 The Cluster mission

The Cluster mission (Figure 3.1), first proposed in the early 1980's, was designed to study the Earth's magnetosphere and its interactions with the solar wind. Four identical spacecraft were constructed to study small-scale structures in three dimensions, orbiting the Earth in a tetrahedron formation. It is interesting to note that in his inaugural lecture in 1966, Dungey made a clear reference to the need for 'satellite bunches' rather than individual spacecraft missions [*Dungey, 1966*]. The Cluster spacecraft fly in a polar orbit with an apogee of $19.6 R_E$, a perigee of $4 R_E$ and were launched in 2001, being declared operational in February 2001 [*Escoubet et al., 2001*]. The regions of particular interest for the Cluster mission are the solar wind, bow shock, magnetopause, cusps, magnetotail and auroral zones.

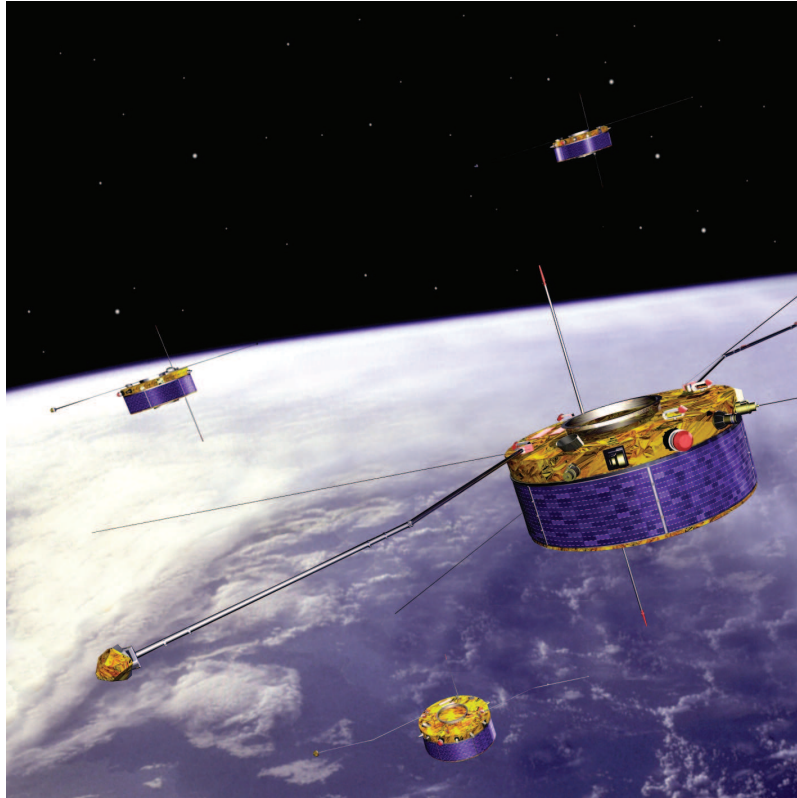


Figure 3.1: Artist's impression of the Cluster spacecraft orbiting the Earth. Courtesy of ESA.

The plane of the spacecraft orbit is fixed in inertial space and so a complete 360° sweep through the magnetosphere is performed each year as the orbit rotates in the XY GSM plane. The GSM coordinate system is discussed in Section 3.5. An example of the orbits at different points throughout a year are shown in panel (a) of Figure 3.2. The so-called 'tail season', when the spacecraft is at perigee in the magnetotail, is for about 3 months, which was centred on September 1st early in the mission. In addition the orbit of the spacecraft has changed over time, whereby the spacecraft crosses the current sheet at distances closer to the Earth over time. This is due to the line of apsides becoming more tilted and moving more southward over time.

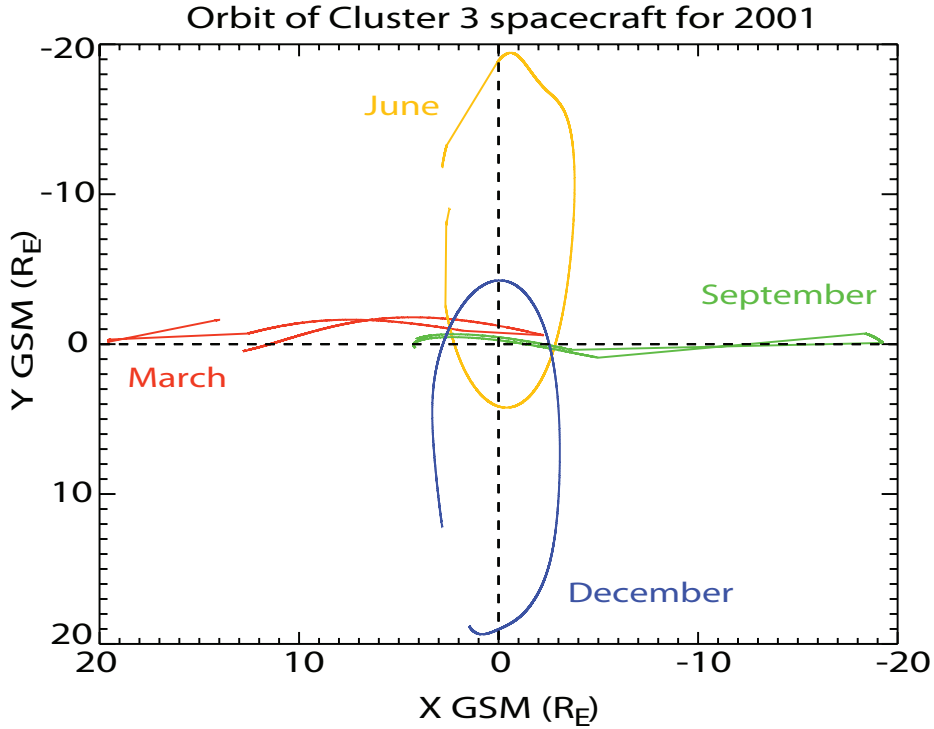


Figure 3.2: Examples of orbits of Cluster 3 at different points throughout the year in 2001.

Each spacecraft is equipped with 11 instruments, measuring electric and magnetic fields as well as ion and electron distribution functions. A list of all the instruments is shown in Table 3.1.

This thesis describes work that utilised data from the Fluxgate Magnetometer (FGM) and Cluster Ion Spectroscopy (CIS) instruments and these will be discussed in the next sections. The data used in the study were obtained from the Cluster Active Archive (CAA, *Perry et al.* [2006] and *Laakso et al.* [2010]). The CAA is an online database of high resolution Cluster data as well as other related data. The initial aims of the service included providing an archive of the best quality data that could be achieved and that its use should be applicable to science research and publication. The data is publicly available and is accessed via personal username and password. As well as data archiving, the service provides documentation on

Table 3.1: A list of Cluster's 11 instruments

Instrument number	Cluster instrument name
1	FGM - Fluxgate Magnetometer
2	EFW - Electric Field and Wave instrument
3	STAFF - Spatio-Temporal Analysis of Field Fluctuation instrument
4	DWP - Digital Wave Processing instrument
5	WHISPER - Waves of High frequency and Sounder for Probing of Electron density by Relaxation experiment
6	WBD - WideBand Data instrument
7	ASPOC - Active Spacecraft Potential Control instrument
8	EDI - Electron Drift Instrument
9	CIS - Cluster Ion Spectrometer
10	PEACE - Plasma Electron and Current Experiment
11	RAPID - Research with Adaptive Particle Imaging Detectors

each instrument, including calibration reports and user guides. The data can be downloaded in small individual files or in larger amounts using the online command-line interface. As well as data retrieval, the website can be used to view the data, using the Graphical Products facility for detailed information and selection or the Quicklook Plots facility which allows the user to view a selection of data, perhaps for checking purposes, which cannot be used in publications as the data have not been calibrated fully. The data from the 11 instruments on the four spacecraft are available on the archive from the start of the mission and the availability of the most up-to-date data depends on the instrument.

3.1.1 Cluster Fluxgate Magnetometer instrument

A simple fluxgate magnetometer, shown in Figure 3.3 is based on a magnetic saturation circuit. It consists of two ferromagnetic parallel bars (cores) positioned close together with each bar being wound by a primary coil, in opposite directions on each core. An alternating current (AC) in the primary coil induces a magnetic

field in each core of the same strength, but of opposite direction at any given point in the AC cycle. The induced field can be made to saturate, which is where the field no longer increases with increasing current. In the presence of an external magnetic field with a component along the axis of the cores, a field is induced in the coils and it will reach saturation at a different time to the other core. Faraday's Law (1.4) tells us that with a temporal variation in the magnetic field, a voltage is induced in the secondary coil which is proportional to the strength of the external magnetic field in the direction of the cores. By using three cores in perpendicular directions, the whole vector magnetic field can be measured.

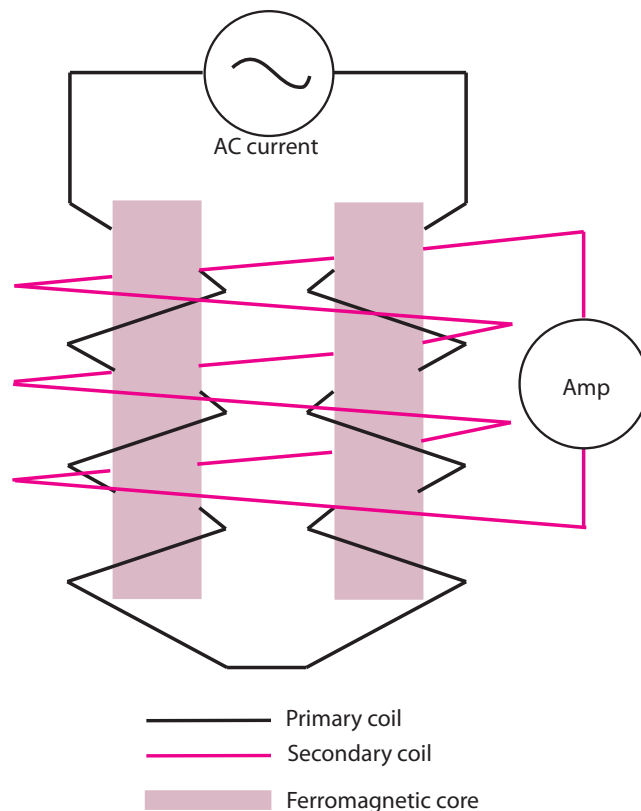


Figure 3.3: Schematic of a basic fluxgate magnetometer.

As part of Cluster's Fluxgate magnetometer (*Balogh et al.* [2001] and *Gloag et al.* [2010]), two triaxial fluxgate magnetic field sensors sit on one of the two 5.2 m radial booms on each of the Cluster spacecraft. In addition a data processing unit

(DPU) is positioned on the main equipment platform of each spacecraft. One of the sensors (Outboard sensor, OB) is at the end of the boom and is usually used as the primary sensor because any effect of background magnetic field from the spacecraft is minimised due to its position. The secondary sensor (Inboard, IB) is positioned 1.5 m from the end of the boom and obtains data at a lower rate. The instrument uses 4 operating ranges which can be selected automatically by the instrument or from the ground. If a component of the measured field is at more than 90% of the range then the range is moved upwards. The magnetic field vectors are sampled at a rate of 201.93 Hz by the primary sensor and transmitted to the ground at a rate of 22.41 Hz and 67 Hz. They are then averaged to usually 5 Hz or spin resolution (about 4 s). The data used in this thesis are both the 5 Hz and spin resolution data.

Calibration is performed both in-flight and on the ground. The calibration takes into account the possible sources of error in the field measurement process as well as interspacecraft calibration. Estimates of the accuracy of the post calibration data are 0.1-0.2 nT for $|B| < 200$ nT and 0.4 nT for $|B| = 200-4000$ nT [Gloag *et al.*, 2010], which is of importance when comparing different magnetic field data.

3.1.2 Cluster Ion Spectrometer instrument

The Cluster Ion Spectrometry (CIS, *Rème et al.* [2001] and *Dandouras et al.* [2010]) experiments consists of two instruments: the COmposition and DIstribution Function analyser (CODIF) and the Hot Ion Analyser (HIA). The purpose of the CIS aspect of the mission is to provide three-dimensional distributions of the main ions of interest in the magnetosphere, mainly H^+ , He^{++} and O^+ . Due to the need to analyse plasma with as low density as in the lobes but also more dense populations as in the solar wind, the CIS provides a large dynamic range. It can cover a wide range of energies, ranging from the spacecraft potential to about 40 keV/e. For

the purposes of this thesis, only the CODIF data were employed.

The CODIF analyser is a mass-resolving spectrometer of high sensitivity providing complete three-dimensional distribution functions of the major ions noted above. It provides the mass per charge composition of the species. The instrument is comprised of a toroidal electrostatic analyser that detects positively charged ions together with a time of flight section, which measures their velocity.

A basic spectrometer with these components usually has two plates with different voltages applied to them. This results in an electric field that acts on charged particles entering the aperture of the analyser section. The electrostatic analyser selects the energy per charge ratio. The ions that pass through the analyser then enter the time of flight region. Here electrons are scattered when the ion impacts some carbon foil, and are subsequently attracted to a positively charged plate. A clock is started when the electrons hit the plate and is stopped when, as a result of the ion hitting a second plate, more scattered electrons impact another positively charged plate. As the distance travelled is known, the velocity, mass and energy can be calculated and the element detected is classified.

Cluster's CODIF instrument uses a copper black coating on the analyser plates and a serrated outer plate, to reduce the transmission of scattered ions. This also reduces the effects of solar UV on the instrument, which can cause problems by producing photoelectrons, which could interfere with the equipment and the accuracy of the data. It is comprised of two 180° sections allowing two different sensitivities of measurement, which achieves the high sensitivity aim of the instrument and the large detection range of densities of ions. The analyser applies a variable high voltage to the inner toroidal plate which allows the selection of particles with a specific energy per charge ratio. The outer plate and top hat section are set to ground potential.

A dual processor-based instrument control and data processing system provide

onboard data processing. Data provided are the plasma density, velocity vectors, momentum flux tensor and the heat flux tensor at spin resolution. During in-flight calibration all functions of the sensor electronics are tested as well as the on-board processing of data. Ground calibration is also undertaken. The data used in this thesis are from Cluster 3 only, in the first and third data studies. The efficiencies of all four spacecraft CODIF instruments have reduced over time and were at less than 5% on Cluster 3 (instrument used in this thesis) in 2008 [*Dandouras et al.*, 2011]. The Cluster 3 instrument was switched off in December 2009 due to a damaged electrical component. The data employed in these studies are up to September 2007.

3.2 OMNI data

In order to investigate interplanetary magnetic field conditions for the final study, the OMNI dataset was used, accessed from the OMNIWeb interface (omniweb.gsfc.nasa.gov). The dataset combines measurements from different spacecraft, usually ACE, Geotail and WIND spacecraft for the time period under study. The data from the spacecraft are lagged to the magnetopause [*Weimer et al.*, 2003; *Weimer*, 2004; *Weimer and King*, 2008a,b]. The data provided are at a resolution of 1 minute and a full description of the methods involved in preparing the data can be found on the OMNIWeb online service .

3.3 Ground-based measurements

In order to investigate substorm and magnetic storm activity, ground-based data were employed from a series of magnetometers, described in the next sections. The data were obtained from the WDC for Geomagnetism, Kyoto.

3.3.1 SYM-H data

The H-component of the symmetric disturbance index (SYM-H) [Iyemori, 1990] at 1 minute resolution is used in this thesis to determine the level of enhancement of the ring current and identify the presence of magnetic storms. The SYM-H index is a derived parameter from measurements taken at six low to mid latitude geomagnetic observatories. Initially, the geomagnetic main field and solar quiet daily variation field must be subtracted from the measurements. Data from five quiet days are averaged and then subtracted from the measurements to produce the disturbance component. The longitudinally symmetric component is derived by averaging the disturbance component for each of the stations being used, which changes depending on availability of good data. The H-component of this parameter is calculated by imposing a latitudinal correction so that the index is in line with the Dst index. The Dst index [Mayaud, 1980] is a separate index derived from stations at slightly lower latitudes, at an hourly time resolution. The SYM-H index provides a high resolution measure of the horizontal component of the disturbance in the geomagnetic field at low to mid latitudes.

As discussed in Section 1.1.3.4 of Chapter 1, the enhancement of the ring current causes a negative disturbance in the geomagnetic field on the night-side of the Earth. The Dst index has long been used to classify the presence of magnetic storms (e.g. Akasofu [1981]) and in more recent times the SYM-H has been employed as a higher resolution counterpart to the Dst index (e.g. Iyemori and Rao [1996]). By comparing Dst and SYM-H data from 1981 to 2002, Wanliss and Showalter [2006] noted an approximate 10 nT difference between the indices for small and moderate magnetic storms, with less than 20 nT difference for intense storms. In view of this the SYM-H index has been the preferred index for indicating the presence of magnetic storms for this research and is more comparable to high resolution spacecraft data than the Dst index.

3.3.2 AE data

The Auroral Electrojet (AE) index [*Davis and Sugiura, 1966*] is used as a measure of substorm activity. Like the SYM-H index it is measured by ground-based magnetometers, recording the horizontal component of the magnetic field, although the chain of magnetometers are at a higher latitude, around the auroral oval. They are therefore best placed to measure any disturbances resulting for substorm activity, as discussed in Section 1.1.3.4 of Chapter 1 and Section 2.2 of Chapter 2.

To derive the index, the average measurements from the chain of magnetometers for the five international quiet days within that month are used to normalise the data. The upper and lower envelopes of the data at each point in time provide the AU and AL indices respectively. The AU (AL) index gives a measure of the eastward (westward) electrojet. The difference between these (AU-AL) gives the AE index, and is generally used as an indication of the overall activity of the electrojets and it is commonly used to provide an indication of the presence of substorm activity [*Baumjohann and Treumann, 1996*].

3.4 Analysis techniques

Two specific analysis techniques have been used in Chapter 5 to estimate the current density and current sheet tilt angle. These are the Minimum Variance Analysis and the Curlometer technique, both described in the following sections.

3.4.1 Minimum Variance Analysis (MVA)

The MVA technique [*Sonnerup and Scheible, 1998*] is used in this thesis to provide an estimation of the orientation of the cross-tail current sheet. The technique assesses from a time series of magnetic field data, the directions of maximum,

intermediate and minimum variance.

The main use of the technique is to find where the variance is minimised so that the normal direction, $\hat{\mathbf{n}}$, can be determined. The variance is given by

$$\sigma^2 = \frac{1}{M} \sum_{m=1}^M |(\mathbf{B}^{(m)} - \langle \mathbf{B} \rangle) \cdot \hat{\mathbf{n}}|^2 \quad (3.1)$$

where

$$\langle \mathbf{B} \rangle = \frac{1}{M} \sum_{m=1}^M \mathbf{B}^{(m)} \quad (3.2)$$

The variance is minimised under the condition that $|\hat{\mathbf{n}}|^2 = 1$. A Lagrange multiplier is then applied with the constraint, resulting in three homogeneous linear equations.

$$\frac{\partial}{\partial n_x} (\sigma^2 - \lambda(|\hat{\mathbf{n}}|^2 - 1)) = 0 \quad (3.3)$$

$$\frac{\partial}{\partial n_y} (\sigma^2 - \lambda(|\hat{\mathbf{n}}|^2 - 1)) = 0 \quad (3.4)$$

$$\frac{\partial}{\partial n_z} (\sigma^2 - \lambda(|\hat{\mathbf{n}}|^2 - 1)) = 0 \quad (3.5)$$

A covariance matrix of \mathbf{B} can then be produced in the form

$$\sum_{b=1}^3 M_{ab} n_b = \lambda n_a \quad (3.6)$$

where M_{ab} , the covariance matrix is $\langle B_a B_b \rangle - \langle B_a \rangle \langle B_b \rangle$ and a and b = 1,2,3 which are the coordinates X, Y and Z. The resulting eigenvectors give the maximum, intermediate and minimum variance directions. A comparison of the eigenvalues allows a judgement as to whether the eigenvectors are meaningful representations for the purpose of the analysis and the ratio of maximum to intermediate eigenvalues is used in this thesis (see Section 5.2.2).

A full description of the analysis technique can be found in *Sonnerup and Scheible [1998]*.

3.4.2 The Curlometer technique

The Curlometer technique [*Dunlop et al., 1988; Dunlop and Woodward, 2000; Dunlop et al., 2002; Dunlop and Eastwood, 2008*] is a method commonly used to estimate the current density of the cross-tail current sheet with Cluster data (e.g. *Forsyth et al. [2009]*). It assumes that the magnetic field varies linearly between the spacecraft and estimates the current density through three of the faces of the tetrahedron, shown in Figure 3.4.

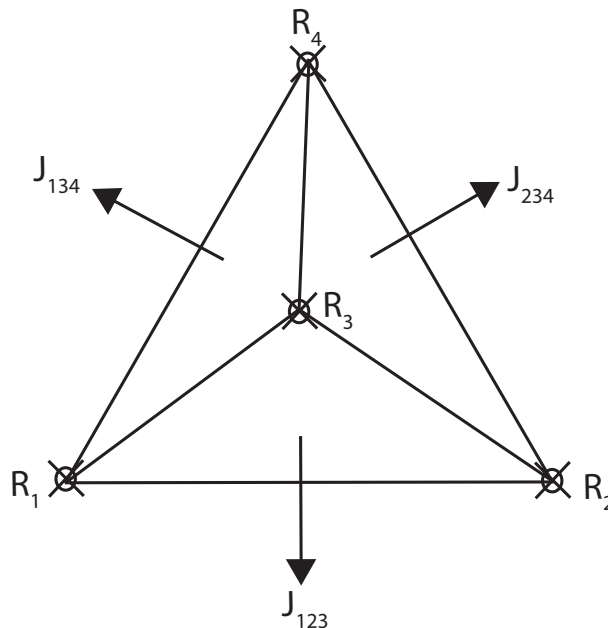


Figure 3.4: Schematic of the Cluster spacecraft to demonstrate the curlometer technique current estimates through each face of the tetrahedron.

Combining Stoke's Theorem and Ampère's Law gives

$$\mu_0 \iint_A \mathbf{J} \cdot d\mathbf{A} = \int_S \mathbf{B} \cdot d\mathbf{S} \quad (3.7)$$

where A is each face of the tetrahedron and the triangular path around A is S. In addition the vector area of each face is

$$\frac{1}{2}(\Delta\mathbf{R}_{21} \wedge \Delta\mathbf{R}_{23}) \quad (3.8)$$

The left hand side of Equation 3.8 is

$$\frac{1}{2}\mathbf{J}_{123} | \Delta\mathbf{R}_{21} \wedge \Delta\mathbf{R}_{23} | \quad (3.9)$$

where \mathbf{J}_{123} is the normal current flow averaged across the face joining spacecraft 1-3.

The right hand side of Equation 3.8 is

$$\int_S \mathbf{B} \cdot d\mathbf{S} = \langle \mathbf{B} \rangle_{ij} \cdot \Delta\mathbf{R}_{ij} + \langle \mathbf{B} \rangle_{ik} \cdot \Delta\mathbf{R}_{ik} + \langle \mathbf{B} \rangle_{jk} \cdot \Delta\mathbf{R}_{jk} \quad (3.10)$$

where $\langle \mathbf{B} \rangle_{ij} = \frac{1}{2}(\mathbf{B}_i + \mathbf{B}_j)$ and is the average magnetic field between spacecraft i and j.

By making one spacecraft a reference and calculating the above for one face,

$$\mu_0 \mathbf{J}_{ij} \cdot (\Delta\mathbf{R}_i \wedge \Delta\mathbf{R}_j) = \Delta\mathbf{R}_j \cdot \Delta\mathbf{B}_i - \Delta\mathbf{R}_i \cdot \Delta\mathbf{B}_j \quad (3.11)$$

Repeating Equation 3.11 for 2 other faces results in 3 simultaneous equations and by combining them, the 3 components of \mathbf{J} can be estimated. The result is considered an estimation of the true current density in the current sheet due to the assumptions made about the linear changes in the magnetic field. Although $\text{div } \mathbf{B}$ should be zero according to Gauss's Law for magnetism, calculations of its value (calculated in a similar way to $\text{curl } \mathbf{B}$) provide non-zero results and are used as a measure of the accuracy of the estimation. The ratio of $\text{div } \mathbf{B}$ to $\text{curl } \mathbf{B}$ is used in this thesis as an indication as to the quality of the current density estimates. The

scale size of the current sheet in comparison to the size of the tetrahedron has an affect on the quality of the measure from this technique. These issues are discussed later in Chapter 5. In addition to the usual quality check of the ratio of $\text{div } \mathbf{B}$ to $\text{curl } \mathbf{B}$, when using the curlometer technique, a subset of curlometer results from this thesis were checked against examples in the research literature.

3.4.3 The Mann Whitney Wilcoxon statistical test

Throughout this thesis the Mann Whitney Wilcoxon test is used to statistically compare certain groups of data. It is a non-parametric test, which is often used when the data groups involved can not be considered to be normally distributed, and as an alternative to the parametric T-Test. The technique tests the null hypothesis that two groups are from the same population. All samples are ranked in order, for both groups. The technique involves noting for each value how many of the data from the other group are less than that value. The sum of these for each group gives the U statistic, which can then be compared to critical value tables for levels of significance. The U statistic is calculated for each group

$$U_1 = N_1 N_2 + \frac{N_1(N_1 + 1)}{2} - R_1 \quad (3.12)$$

where U_1 is the U statistic for group 1, N_1 is the number in group 1 and R_1 is the sum of the ranks in group 1. A more detailed explanation can be found in *Barlow [1989]*.

3.5 Coordinate Systems

There are various coordinate systems used in solar-terrestrial research. The coordinate system used in the work throughout this thesis is the Geocentric Solar Magnetospheric (GSM) system (Figure 3.5). It is an Earth-centred system and

the X-axis is fixed along the Earth-Sun direction, with positive values towards the Sun. The results within this thesis will often be described at a certain distance ‘downtail’, which means at a point within the magnetotail. These positions are at negative X values in the GSM system. The Y-axis is perpendicular to the Earth’s magnetic dipole and along the dawn-dusk meridian, with dusk at positive Y values. The Z-axis is in the same sense as the northern magnetic pole, with the dipole lying in the XZ GSM plane (panel b of Figure 3.5). The angle between the GSM Z-axis and the north magnetic pole is known as the dipole tilt angle, which is positive when the pole is towards the Sun. With the daily rotation of the Earth, the Y and Z GSM axes are not fixed with respect to the Sun and move about the X GSM axis, whilst always staying orthogonal to each other, and to the X-axis (panel c).

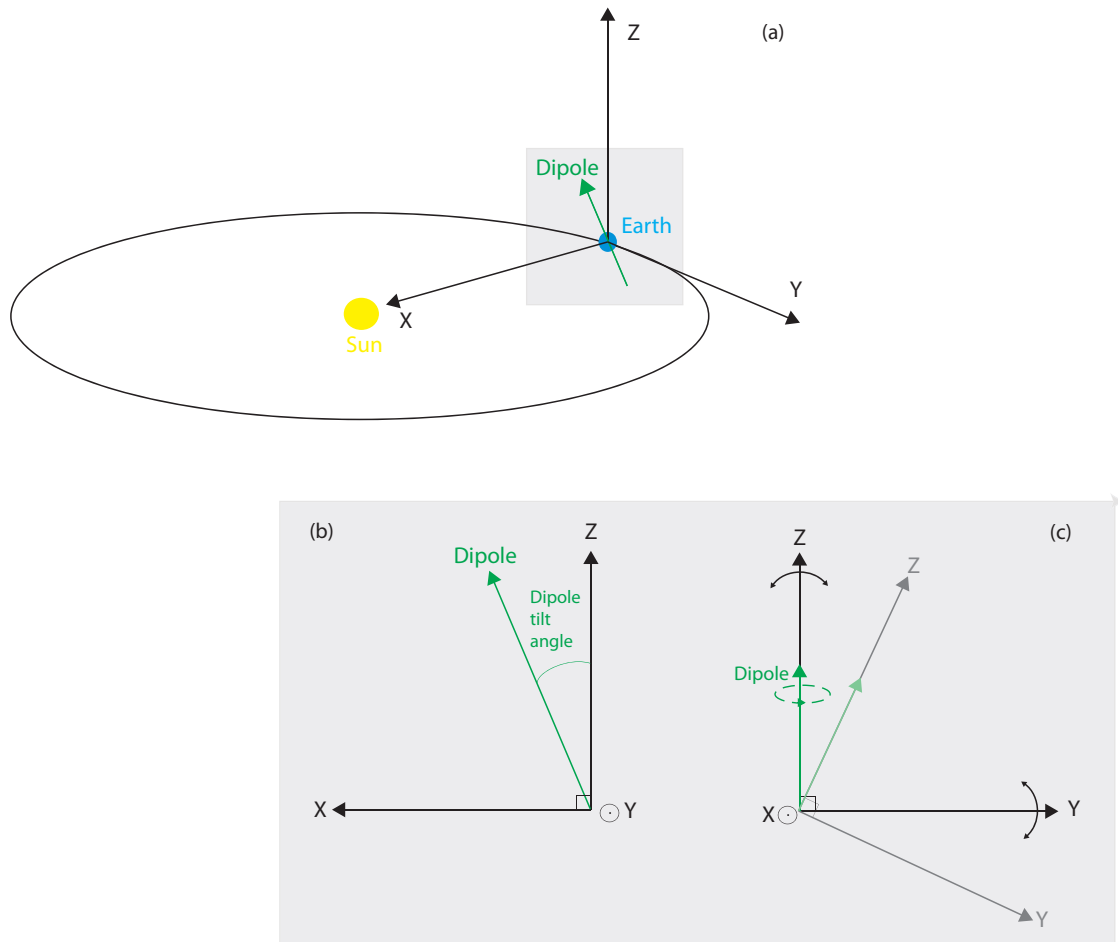


Figure 3.5: Diagram showing the GSM coordinate system. Panels b and c are different views of panel a, showing that the X axis is fixed on the Earth-Sun line and the Y and Z axes move about the X axis in response to the dipole tilt.

Chapter 4

Current sheet motion

As discussed in Chapter 2, there is evidence that the current sheet is a dynamic region and is often described as moving in a flapping motion, in a North-South direction [*Speiser and Ness*, 1967]. The cause of this flapping is not currently known but the literature does include research on its connection with substorms (e.g. *Sergeev et al.* [2004]) and solar wind pressure pulses (e.g. *Forsyth et al.* [2009]). Although current sheet motion has been observed during both types of activity, no clear cause and effect has been shown and current sheet motion during magnetic storms has not been investigated to date. In addition, *Milan et al.* [2008] showed that the magnetotail was stabilised to the onset of substorms due to the large amount of open flux in the tail during magnetic storms.

The work in this chapter was stimulated by both the lack of research regarding current sheet motion during different levels of geomagnetic activity and the desire to investigate if the stabilisation observed by *Milan et al.* [2008] is evident in current sheet motion. This chapter describes work comparing current sheet motion during different geomagnetic conditions, specifically during quiet times, substorms and magnetic storms. The topic is investigated from a statistical perspective, looking at the number of current sheet crossings made by the Cluster spacecraft, during each orbit through the magnetotail, together with the geomagnetic conditions during

each orbit, defined by the AE and SYM-H indices (described in Sections 3.3.2 and 3.3.1 of Chapter 3).

4.1 Selection of dataset

In order to study the dynamics of the current sheet, a database was created of each orbit of the Cluster 3 spacecraft through the mid region of the magnetotail, setting an inner limit at $X=-8 R_E$ (to ensure that the data is further downtail than the ring current) and a maximum distance downtail equivalent to the distance at apogee at approximately $X=-19 R_E$. The number of current sheet crossings within each orbital pass through the region was identified, thereby viewing the orbits as a whole. This enabled an investigation of current sheet activity within one orbital pass, during magnetic storms, substorms and quiet conditions. The data comprised orbits from July/August to October/November of each year, from 2001 to 2007.

The X (GSM) component of the magnetic field (B_X) measured by Cluster 3 was used to identify the crossings of the current sheet and thereby study its motion. B_X is positive in the north lobe of the magnetotail, passing through $B_X=0$ in the current sheet, and is negative in the south lobe. Current sheet motion is identified when B_X is seen to fluctuate about $B_X=0$. A crossing of the current sheet is defined here as a change in B_X from +5 nT to -5 nT or vice versa and the crossings for each orbit were counted. This criterion resulted in a dataset of part-orbits through the magnetotail, with one or more crossings of the current sheet in each orbit.

In addition, smaller and larger changes in B_X were also considered, to assess the impact of different thresholds on the results. As well as using a ± 5 nT threshold in B_X , ± 3 nT and ± 7 nT thresholds in B_X were also employed in this study. The B_X threshold criteria used in this study are different from those employed in other studies (e.g. *Runov et al.* [2006]). Other studies investigated the flapping motion of the current sheet by considering larger changes in B_X and limiting the

time duration of each crossing. Simple criteria are employed here to consider more general motion of the current sheet.

Examples of orbits with current sheet crossings are shown in Figure 4.1. Panel (a) of Figure 4.1 shows the B_X component from an orbit with only one ± 5 nT crossing as defined by the criterion, indicating a stable current sheet. Panel (b) of Figure 4.1 shows the B_X component from an orbit with 19 crossings at the ± 5 nT threshold, indicating a more dynamic current sheet. By comparison to the number of 5 nT crossings for the orbits shown in Figure 4.1, panel (a) contains only one (nine) crossing at the ± 7 nT (± 3 nT) threshold and panel (b) contains 13 (23) at the ± 7 nT (± 3 nT) threshold.

In order to minimise undetected crossings due to data gaps, orbits with data gaps of more than 480 seconds in the region where the crossings occurred, were removed from the dataset. In addition, Cluster enters the magnetosheath during some of its orbits, where the spacecraft are towards the flanks of the tail. The magnetosheath is a region where the magnetic field is highly variable in nature and plasma densities can reach 20 cm^{-3} [Sibeck and Gosling, 1996]. It is therefore highly probable that B_X variations on orbits which cut through the flanks of the tail could be due on occasion to the spacecraft passing into the magnetosheath rather than current sheet motion. Thus, in order to ensure that crossings into the magnetosheath have been removed such that magnetic field fluctuations measured were due to current sheet motion alone, two further criteria were employed. Orbits with a maximum H^+ number density of more than 1.5 cm^{-3} , between the start and end of the crossings within each orbit, were not included. In addition, orbits with crossings in the flanks of the tail ($|Y(\text{GSM})| > 10 R_E$) were removed. The resulting database comprised 128 orbits from 2001 to 2007, as H^+ density data were unavailable at the time in the CAA after 2007. The final dataset included orbits from August to November due to the restrictions set in $Y(\text{GSM})$.

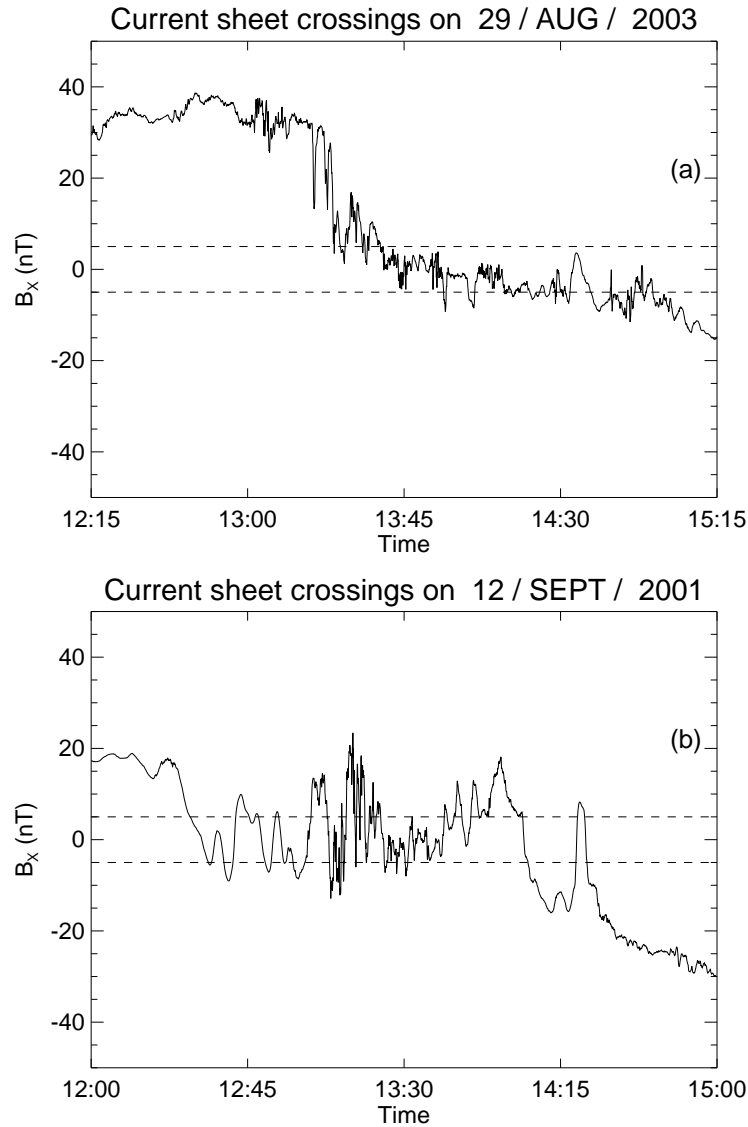


Figure 4.1: Examples of crossings of the current sheet by the Cluster 3 spacecraft, indicated by changes in B_X between $+5$ and -5 nT and vice versa. A stable current sheet (with 1 crossing) is shown in panel (a). A more dynamic current sheet (with 19 crossings) is shown in panel (b).

Figure 4.2 shows the distribution of the positions of the crossings for all data, with each line representing a 5 nT crossing. The limits in the X and Y directions (GSM) are due to the orbit of the spacecraft and the limits in Y defined above. The positions of the crossings in the Z (GSM) direction range from about -4 to $+5 R_E$. The middle panel of Figure 4.2 shows a tilt in the position of the crossings in YZ plane using data from 2001 to 2007. This tilt was also observed by *Petrukovich*

et al. [2005], who used data from Cluster's 2001-2003 tail seasons. They noted that the macroscale position of the current sheet in the YZ plane was due to seasonal changes in the dipole tilt orientation. Similar YZ tilts were observed by *Zhang et al.* [2006] who used 2001 and 2002 Cluster tail season data and by *Rong et al.* [2010] who used 2001-2005 Cluster data.

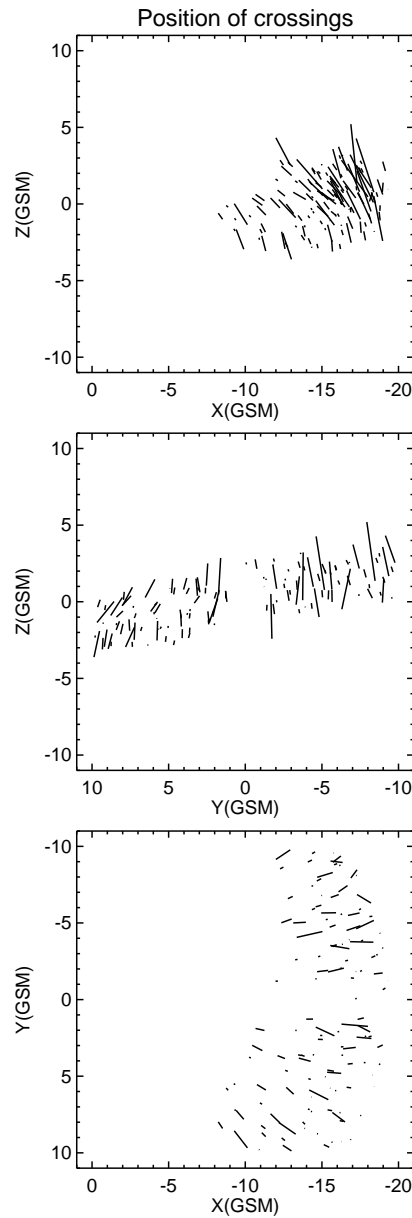


Figure 4.2: Position of crossings, shown by each black line. Positions are shown in the XZ, YZ and XY GSM planes. The lines shown for each crossing cover the positions of the start and end of each crossing as defined by a change in B_X between at least +5 and -5 nT.

Figure 4.3 presents the distribution of the number of crossings per orbit for the whole dataset, for 7 nT (panel a), 5 nT (panel b) and 3 nT (panel c) threshold criteria. In the 128 orbits within the database, there were 445 crossings using the ± 7 nT criterion, 648 crossings using the ± 5 nT threshold and 1022 crossings using the ± 3 nT threshold. The mean number of crossings for each threshold was 3.5, 5 and 8 for the 7 nT, 5 nT and 3 nT criteria respectively. Considering the 5 nT crossings in panel (b), almost half of the orbits contain only one crossing, implying that the current sheet is in a stable condition for half of the time, based on this criterion. In addition, 63% of the orbits have less than the mean number of 5 nT crossings. It is also clear that the 7 nT threshold data are dominated by only one crossing per orbit, compared to the 3 nT threshold data, where there is more spread in the data and less than 45% of the data only have one crossing per orbit. The following analysis will consider the 5 nT crossings only, but the other thresholds will be revisited in Section 4.2.

Figure 4.4 shows the distribution of mean number of crossings per orbit per year in red using the left-hand Y-axis, using the 5 nT threshold criterion. The mean number of crossings peaks in 2002 and is then followed by a decline up to 2007. The standard error of the mean is shown by vertical lines through the centre of each bar.

Figure 4.5 shows selected orbits from August 2002 and 2007. The point of apogee for each of the orbits changes over the years under study, meaning that the passes through the current sheet are not at the same position in the tail nor do the Cluster spacecraft pass through the current sheet at the same angle. Those passes at an angle away from the current sheet normal will spend longer in the vicinity of the current sheet than those following a path along the normal. In addition, the slices through the current sheet are not in the same section of the orbital path, when the spacecraft is travelling at different speeds at different sections of the orbit. As a result of these issues, when the spacecraft spends more time in the current

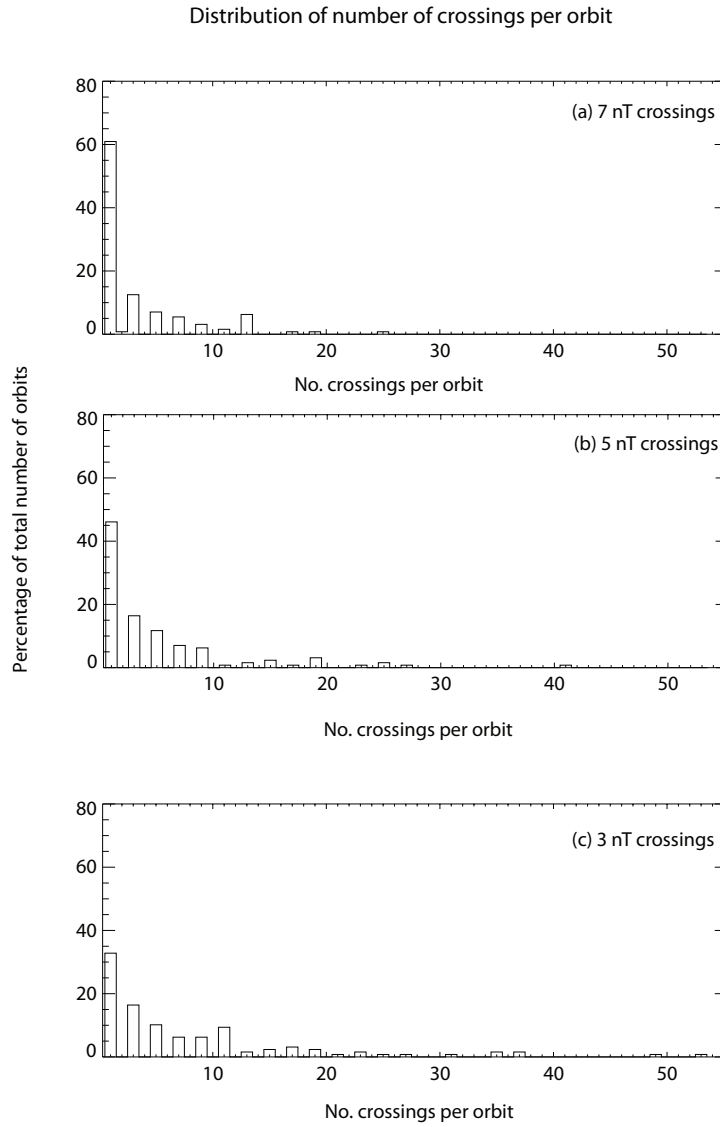


Figure 4.3: Distribution of number of crossings per orbit. Panel (a) shows the number of 7 nT crossings, panel (b) shows the number of 5 nT crossings and panel (c) shows the number of 3 nT crossings.

sheet, it is more likely that motion will be observed.

In order to remove any orbital effect, the number of crossings per orbit was normalised to the amount of time spent between $+3 R_E$ and $-4 R_E$ in the Z GSM direction. For each orbit, the number of crossings was divided by the time spent in

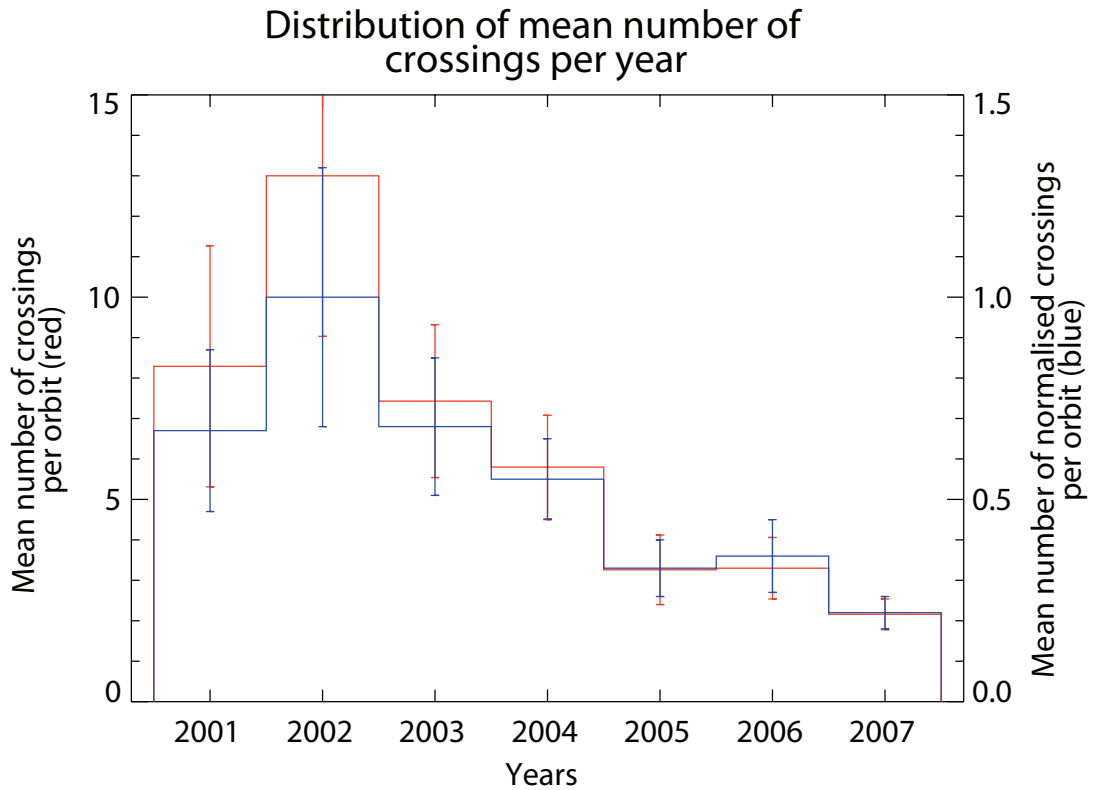


Figure 4.4: Distribution of mean number of crossings per orbit per year in red for 2001 to 2007, using the left-hand Y-axis. The mean number of normalised crossings per hour in each orbit for 2001 to 2007 is shown in blue, using the right-hand Y-axis. The normalised data were calculated by dividing the number of crossings within each orbit by the time spent between $+3 R_E$ and $-4 R_E$ in the Z (GSM) direction (the spread of positions of the crossings in the dataset). Standard errors of the means are shown by vertical lines in the centre of each bar.

the aforementioned region, resulting in a normalised number of crossings per hour per orbit. A more detailed explanation of this method is discussed in Section 4.3. Figure 4.4 shows the distribution of the mean number of normalised crossings per year in blue using the right-hand Y-axis. Again the standard error of the mean is shown by vertical lines through the centre of each bar. The data show a similar decline in the mean number of crossings after 2002 to that in red. The decline in the number of crossings seen may be due to external effects, such as solar cycle variability, rather than changes in the orbital path of the Cluster spacecraft. During periods of high solar activity, for example around 2000-2002, the dynamics of the

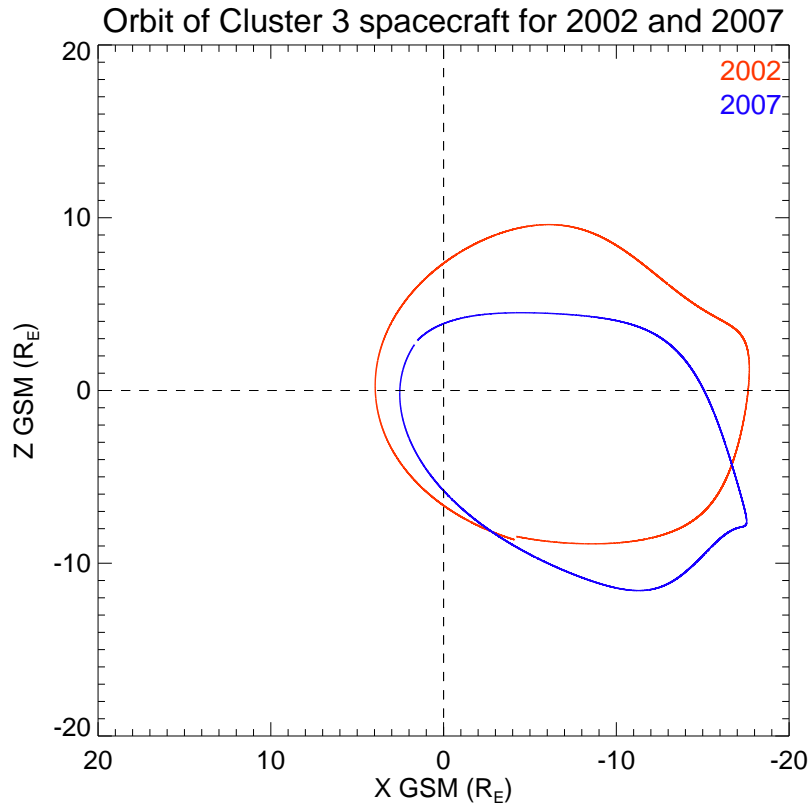


Figure 4.5: Selected Cluster 3 orbits from August 2002 (red) and 2007 (blue), in the XZ plane in GSM coordinates, showing the change in orbital path over time.

tail may be increased compared with periods of lower solar activity. However, further study would be required to confirm this suggestion.

4.2 Orbit analysis

Comparing orbits in the dataset is problematic due to the issues discussed in the previous section concerning the changes in the orbital path of the Cluster spacecraft over time. Therefore in the initial analysis each year was treated separately since changes of the orbit within each tail season are minor compared to changes between tail seasons. The time period when crossings occurred was used to determine the geomagnetic conditions for each orbit.

For each year, the data were divided into 2 groups: a stable current sheet (< 5 crossings per orbit) and a group where the current sheet was more disturbed (≥ 5 crossings). Five crossings have been selected to separate the dataset since this was the mean number of crossings per orbit for the entire dataset and the two groups are approximately equal in size.

4.2.1 Geomagnetic activity

The AE index is a measure of electrojet activity, as discussed in Section 3.3.2. The standard deviation of the AE index during the time duration of the crossings is used as an indication of the presence of substorms for each orbit. This parameter provides an insight into whether the AE index was changing during the crossings, rather than using a threshold value, which would not necessarily inform us as to the presence of substorms, and may only indicate a high baseline value. The mean values of the standard deviation of the AE index for each group (inactive current sheet and active current sheet) for the 5 nT crossings are shown for each year in Figure 4.6. The standard errors of the mean values are indicated by the vertical lines through the bars. The number of orbits in each group of Figure 4.6 are shown above each bar. A difference is seen between the mean values of the standard deviation of the AE index for the inactive current sheet and the active current sheet. For every year studied this parameter is higher and hence there is more variability in the AE index present during the orbits with an active current sheet. To investigate the significance of these results, the Mann-Whitney-Wilcoxon test (*Barlow* [1989], pg. 174) was applied. This test was selected because it cannot be assumed that the data are normally distributed, and the Mann-Whitney-Wilcoxon test does not assume a normal distribution. However, such tests were limited due to the sometimes small sample sizes for comparison, and were not possible for 2002 or 2007. Where the test was applicable, results were statistically significant (reaching a significance level of < 0.05) for all the years except in 2006.

Comparison of an inactive and active current sheet

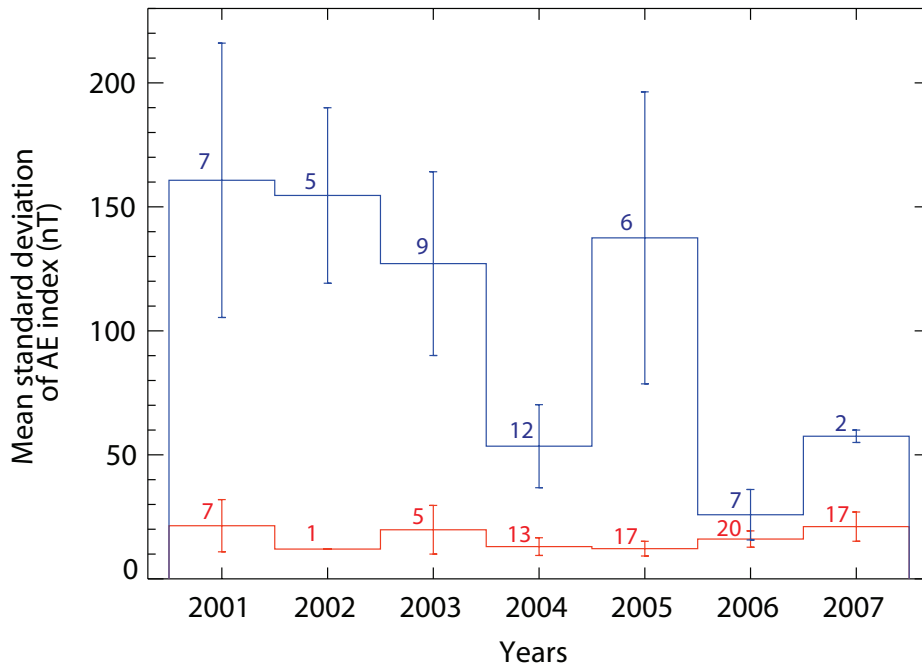


Figure 4.6: Mean standard deviation of the AE index for an inactive current sheet (red) compared to a more active current sheet (blue). The inactive current sheet group comprises orbits with less than average number of crossings (< 5 crossings). The active current sheet group comprises orbits with greater than average crossings (≥ 5 crossings). Standard errors of the means are shown by vertical lines in the centre of each bar. The number of orbits in each group are shown above each bar.

The data for 2001-2004 were combined as the orbital path varies less within these years than after 2004. A similar comparison of an inactive and active current sheet was made, shown in panel (a) of Figure 4.7. Standard errors and numbers in each group are shown for each bar. There is a significant difference between the active and inactive current sheet groups ($p < 0.05$). Figure 4.7 also shows the same comparison (also using ≥ 5 crossings to define an active current sheet) for the 3 nT crossings (panel (b)) and the 7 nT crossings (panel (c)). Significant differences between an inactive and active current sheet are also present for both smaller threshold (3 nT) and larger threshold (7 nT) crossings.

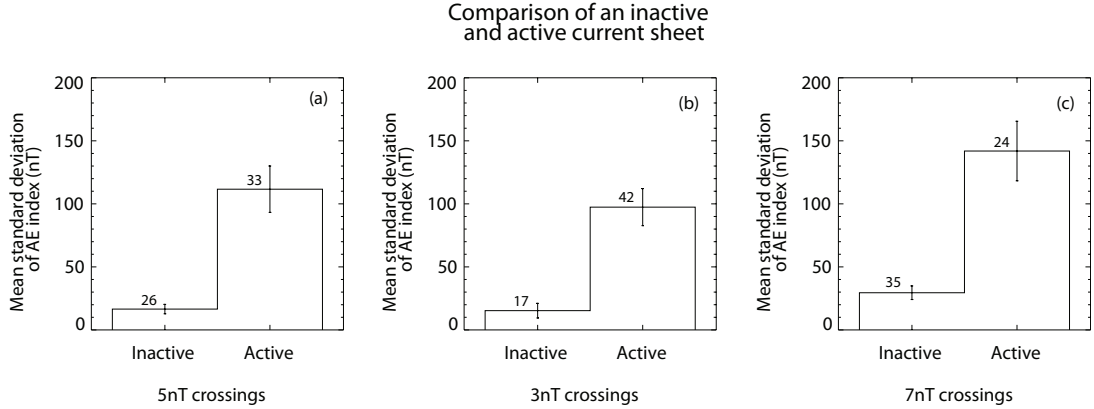


Figure 4.7: Mean standard deviation of the AE index for an inactive current sheet compared to a more active current sheet for 5 nT (panel (a)), 3 nT (panel (b)) and 7 nT (panel (c)) crossings. The inactive current sheet group comprises orbits with less than average number of crossings (< 5 crossings). The active current sheet group comprises orbits with greater than average crossings (≥ 5 crossings). Standard errors of the means are shown by vertical lines in the centre of each bar. The number of orbits in each group is shown above each bar. Data used are for 2001-2004 only.

4.2.2 The influence of substorms and magnetic storms

The data were then grouped in a different way to further examine the influence of substorms and magnetic storms. Within each year, data were separated based on various conditions, using the values of AE and SYM-H. Quiet conditions were defined as having a standard deviation of the AE index of less than or equal to the mean value of the standard deviation (47 nT) together with a quiet ring current (minimum SYM-H > -50 nT). An enhanced ring current was defined as having a minimum SYM-H value of less than -50 nT. For each year, three groups were compared: quiet geomagnetic conditions (Quiet), conditions with a quiet ring current but greater than average standard deviation of the AE index (AE), and similar AE variability to the ‘AE’ group together with an enhanced ring current (RC). Figure 4.8 shows the mean number of 5 nT crossings for each of these groups for each year, with the standard error of the mean shown by vertical lines. The number of

orbits in each group is indicated by the numbers next to each data point. Note that for years 2005-2007 there were no orbits in the RC (blue triangles) group. Out of the 128 orbits in the dataset, only 6 orbits had a minimum SYM-H value of less than -50 nT occurring with greater than average AE variability. When the data are divided into separate years, the numbers for comparison are therefore reduced.

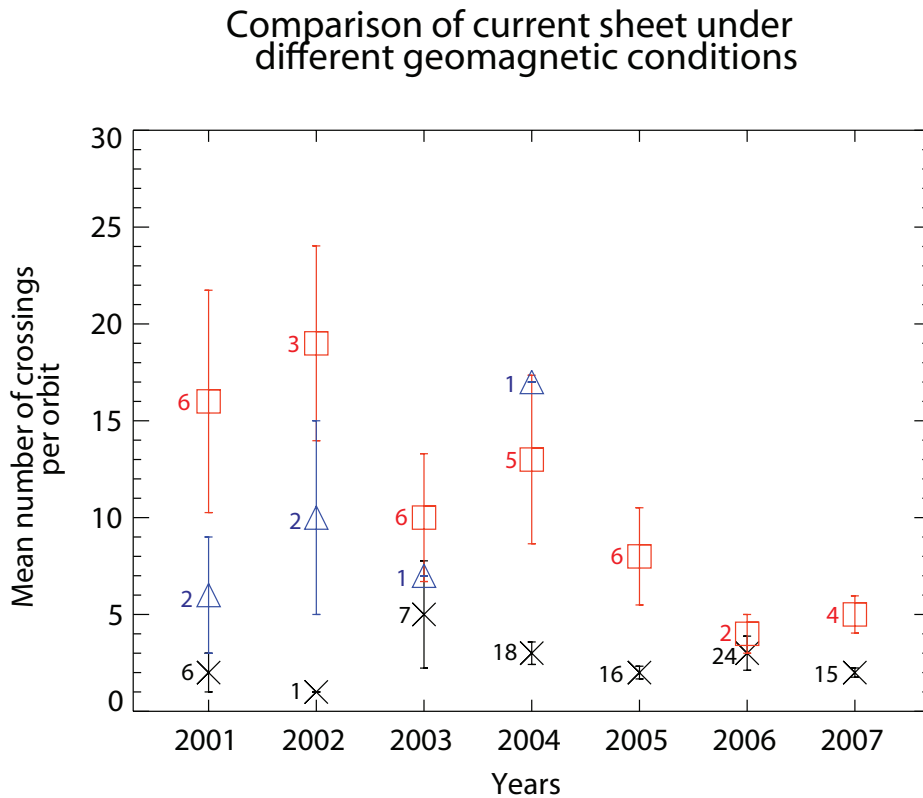


Figure 4.8: Mean number of crossings for different conditions. A group of orbits under quiet conditions (Quiet) are shown by black crosses, with low AE variability and a quiet ring current. A group of orbits with greater than average AE variability (AE) and a quiet ring current are shown by red squares. Finally the blue triangles show a group of orbits with an enhanced ring current and greater than average AE variability (RC). Standard errors of the means are shown by vertical lines and the number of orbits in each group is shown by each data point.

However, there are two main results from Figure 4.8. Firstly the mean number of crossings is larger in the groups with more AE variability (AE - red squares) than compared to quiet conditions (Quiet - black crosses) for each year studied.

This result is in line with that obtained in the earlier analysis. Again statistical testing was limited due to small group sizes. However, where the Mann-Whitney test was applied, there was a significant difference between the ‘AE’ and ‘Quiet’ groups for all years except 2003 and 2006.

Secondly, data from 2001 to 2003 showed that orbits with an enhanced ring current (RC - blue triangle) had a lower mean number of crossings when compared to the conditions with a quiet ring current and high AE variability (AE - red squares). Unfortunately there were no orbits in the ‘RC’ group for the years 2005-2007. Data from 2004 show an increase in the mean number of crossings for the enhanced ring current group compared to the other groups. However, this ring current group is based on only one orbit. Statistical tests were not possible on the ring current group due to the sample sizes.

Figure 4.9 shows comparison data for 2001-2004 for the 5 nT crossings (panel (a)) as well as the 3 nT (panel (b)) and 7 nT (panel (c)) crossings. Again, vertical lines through each bar indicate the standard error and the number of orbits in each group is shown above each bar. Results show larger mean number of crossings for the ‘AE’ group compared to the ‘QT’ group for all sizes of crossing. The differences between the ‘QT’ and ‘AE’ groups are statistically significant. The ‘RC’ groups show a smaller mean value of crossings compared to the ‘AE’ group for all sizes of crossing, although the difference for the 7 nT data is only very small.

The analysis shows an increased motion of the current sheet during larger than average AE variability. There is also some evidence of a reduced motion during times with an enhanced ring current in the 5 nT and 3 nT data, but the ring current has very little effect on the larger crossings (7 nT). A further method of analysing the data was then employed, discussed in the next section.

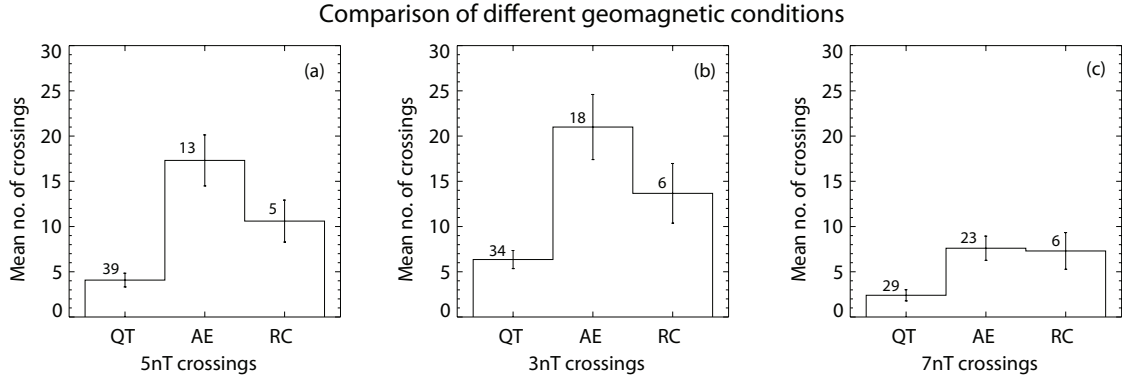


Figure 4.9: Mean number of crossings for different conditions for 5 nT (panel (a)), 3 nT (panel (b)) and 7 nT (panel (c)) crossings. A group of orbits under quiet conditions have low AE variability and a quiet ring current (QT). A group of orbits with greater than average AE variability and a quiet ring current are shown by ‘AE’. Finally ‘RC’ shows a group of orbits with an enhanced ring current and high AE variability. Standard errors of the means are shown by vertical lines in the centre of each bar. The number of orbits in each group is shown above each bar. Data used are for 2001-2004 only.

4.3 Normalising the data

An alternative method of analysing the data is to normalise the orbits against the amount of time spent near the current sheet. The Cluster spacecraft spent different periods of time near the current sheet due to changes in the orbital path from 2001 to 2007 as indicated in Figure 4.5. By approaching the current sheet from different angles due to a combination of the orbital plane and the tilt of the current sheet, the spacecraft spent a shorter time in the current sheet when approaching from an angle along the normal to the current sheet compared to an angle away from the normal. To reduce the impact of such orbital effects, the number of crossings for each orbit was divided by the time taken for the spacecraft within each orbit to travel from $+3 R_E$ to $-4 R_E$ in the Z (GSM) direction. This range was chosen because it was within the region that the crossings occurred for the whole database and because the spacecraft orbits crossed this region within the tail for all the years studied. This result is referred to as the normalised number of crossings per

hour. The previous section considered smaller and larger changes in B_X to define a crossing and demonstrated that using a change of 5 nT in B_X was a sensible criterion to use to define a crossing of the current sheet and show any effects of an enhanced ring current and substorms. In the following analysis therefore, only 5 nT crossing data are used.

Figure 4.10 shows the mean values of the standard deviation of the AE index for a group with lower than average normalised number of 5 nT crossings (0.5), shown by the ‘Inactive’ group compared to a group with greater than average motion (Active). The standard error of the mean is shown by vertical lines through the centre of each bar. The results show that the standard deviation of the AE index is larger for orbits with the most normalised crossings. The number of orbits in each group are shown above each bar. Statistical testing using the Mann-Whitney-Wilcoxon test shows significant differences (reaching a significance level of <0.01) in the standard deviation of the AE index between the groups.

Figure 4.11 shows the mean number of normalised crossings for different conditions with the standard error of the mean shown by vertical lines through the centre of each bar. The number of orbits in each group are shown above each bar. The conditions are the same as those discussed previously: a quiet conditions group, a group with larger than average AE variability and a group with an enhanced ring current together with larger than average AE variability. The results show that orbits with a high standard deviation of the AE index and a quiet ring current (AE) have a higher mean number of current sheet crossings per orbit (normalised for the effect of different orbital paths from year to year) compared with quiet conditions (Quiet). This is statistically significant (reaching a significance level of <0.01). The data also show that orbits with an enhanced ring current (RC) tend to have a slightly lower mean normalised crossings value compared to the ‘AE’ group, although this result was not statistically significant.

Comparison of an inactive and active current sheet

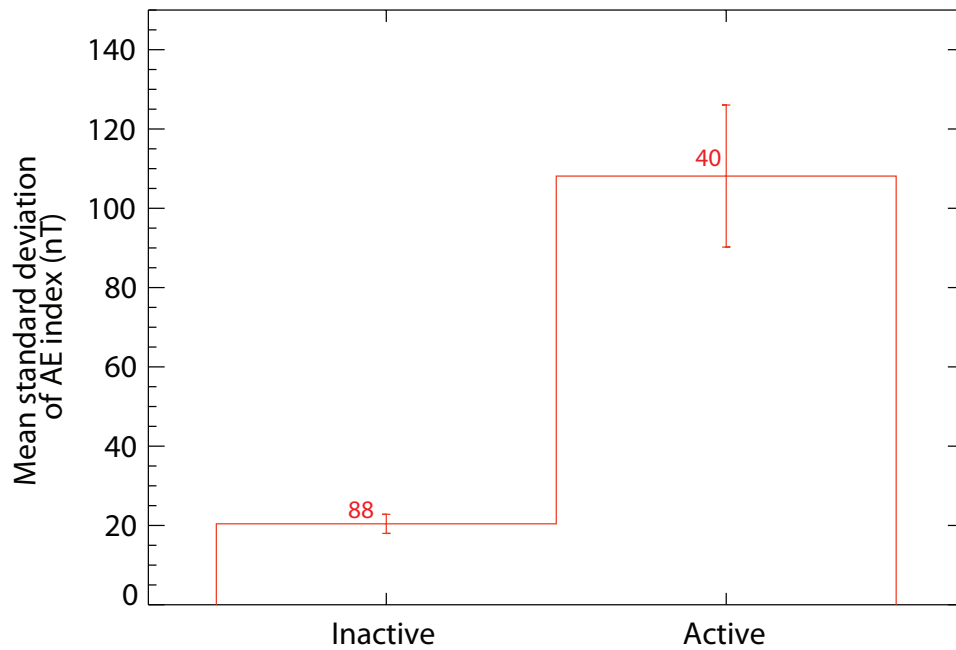


Figure 4.10: Mean standard deviation of the AE index for an inactive current sheet compared to a more active current sheet, for the normalised data. The inactive current sheet group comprises orbits with less than average number of normalised crossings (< 0.5 crossings per hour per orbit). The active current sheet group comprises orbits with greater than average normalised crossings (≥ 0.5 crossings per hour per orbit). Standard errors of the means are shown by vertical lines in the centre of each bar.

Comparison of current sheet under different geomagnetic conditions

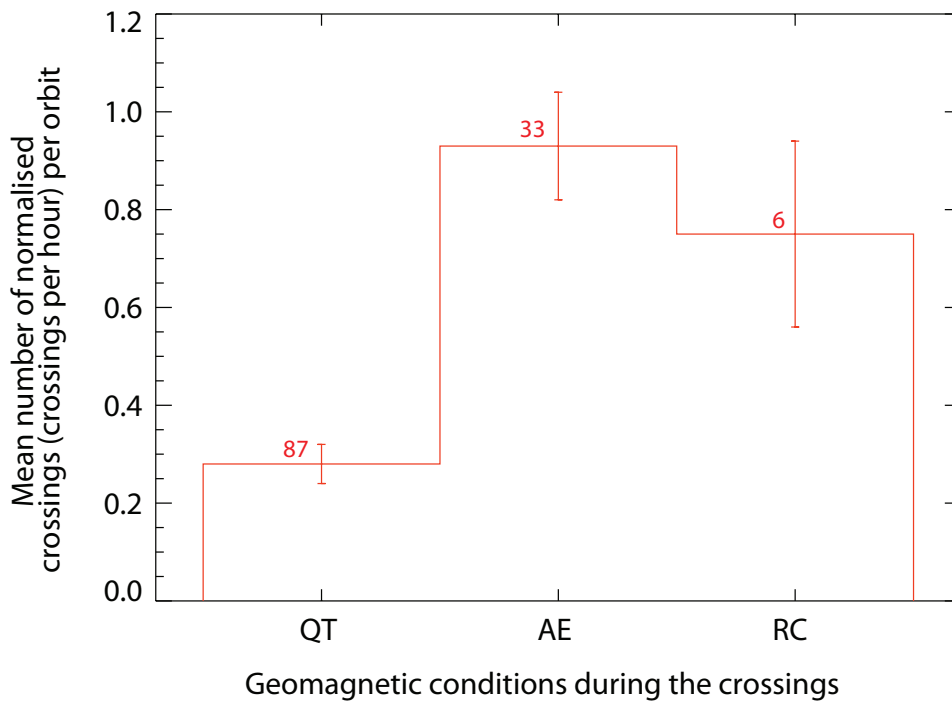


Figure 4.11: Mean number of crossings for different conditions for the normalised data. The group of orbits under quiet conditions (QT) have low AE variability and a quiet ring current. The group of orbits with greater than average AE variability and a quiet ring current are indicated by 'AE'. Finally the 'RC' group is a group of orbits with an enhanced ring current and high AE variability. Standard errors of the means are shown by vertical lines in the centre of each bar.

4.4 Discussion

The investigation of the magnetotail current sheet surveyed Cluster 3 orbits through the region and compared geomagnetic conditions for these orbits in terms of substorms and magnetic storms.

Figure 4.3 showed that 46% of orbits comprised one crossing of the current sheet using a ± 5 nT change in B_X , suggesting a stable region for nearly half the orbits studied. The distribution of different sizes of crossing was also compared using 3 nT and 7 nT thresholds. The results demonstrated that the majority of the orbits contained only one 7 nT crossing, but using the 3 nT threshold, less than 45% of orbits contained only one crossing and there were many orbits with more than one 3 nT crossing. Figure 4.4 showed that the mean number of crossings per year declined after 2002, which coincides with the declining phase of the solar cycle, implying that external effects may have an influence on the dynamics of the cross-tail current sheet. *Tanskanen et al.* [2011] showed a peak in substorms during 2003 in a study of 9000 substorms during solar cycles 22 and 23, covering 1993-2008. A comparatively low number of substorms occurred in 2002, at the time of the peak in the number of crossings in the present study. The different distributions in number of substorms and number of crossings in the two studies further implies that the solar cycle may affect current sheet motion and that if substorms play a role in current sheet motion, external effects may also be important. However, solar wind parameters prior to the crossing events have not been studied here, preventing a full investigation of the effect of external influences.

Two main methods of analysis were used to compare the orbits. Both methods considered the orbital path through the current sheet as a whole rather than studying each individual crossing of the current sheet. The first approach was to treat each year separately. The second method involved normalising the data in terms of its orbit, by considering the amount of time the spacecraft spent in the region

under investigation. The size of crossings was also compared, in terms of a change in B_X from +5 nT to -5 nT and similarly using ± 3 nT and ± 7 nT thresholds, for 2001-2004 data.

The survey provided two main results. Both methods of analysis showed that the current sheet is generally more dynamic in orbits where the standard deviation of the AE index is higher. Periods of large standard deviation of the AE index can be interpreted as having more magnetic variability due to a combination of more substorm activity and stronger substorms. It should be noted that although the results are not presented here, an identical picture is seen when using the maximum AE index reached during the crossings, rather than the standard deviation of the AE index, for the comparisons shown in Figures 4.6 and 4.8. Using either the standard deviation or maximum value reached of the AE index, both showed a more dynamic current sheet with substorm activity. The relationship with the AE index is in agreement with previous authors who studied individual crossings of the current sheet (e.g. *Sergeev et al.* [2006]) who found a correlation of current sheet motion with the growth phase of the AE index. The results also show that when the ring current is enhanced during magnetic storms, there is some evidence that the current sheet may be stabilised in terms of its motion for the 3 nT and 5 nT crossings, when compared to periods of substorm activity and a quiet ring current. The effect of the ring current is minimal for current sheet crossings involving a larger change in B_X . The difference between the larger and smaller changes in B_X is not surprising and fewer crossings per orbit when considering larger changes in B_X is to be expected. The results demonstrate that using a ± 5 nT threshold in B_X is appropriate for studying the effect of substorm and magnetic storm activity on the current sheet.

The reason for the possible ring current stabilisation effect is not clear. *Milan et al.* [2008] previously suggested a stabilising effect of an enhanced ring current on the magnetotail to substorm activity. It can be speculated that the increase

in the amount of open magnetic flux in the lobes observed by *Milan et al.* [2008] during these periods increases the rigidity of the tail and suppresses current sheet flapping. Although the group of orbits of Cluster 3 through the current sheet which coincided with an enhanced ring current was not large in number, the dampening effect was observed in the data and certainly warrants further study.

The aim of the study was to observe the current sheet on a global scale and as such the tilt or thickness of the current sheet have not been considered, which may have an effect on the amount of motion observed. The results of an investigation of tilt, half thickness and current density changes throughout each orbit in the database, is the subject of the next chapter. This will also provide a measure of how changeable the structure of the current sheet is under different geomagnetic conditions.

4.5 Conclusions

An analysis of the motion of the current sheet and the effects of substorms and magnetic storms was carried out using Cluster 3 data from 2001-2007. It was found that:

1. There is a decline in the mean number of crossings per year after 2002, which coincides with the decline of the solar cycle. This may suggest external influences affect current sheet motion.
2. The current sheet is generally more dynamic when the AE index implies greater than average substorm activity and a quiet ring current.
3. The current sheet is stabilised in terms of its smaller scale motion during periods of substorm activity when the ring current is enhanced, compared to periods of substorm activity and a quiet ring current. It is proposed that

magnetic storms cause a rigidity of the magnetotail which inhibits current sheet motion.

Chapter 5

Current sheet structure

5.1 Introduction

The main focus of this chapter is the structure of the cross-tail current sheet of the magnetotail, in terms of its orientation, current density and thickness. Again, Cluster data are used to assess these parameters, and are combined with ground-based data that record substorm and storm activity, to provide a comparison of the sheet parameters under different geomagnetic conditions.

The chapter initially describes the selection of the dataset, together with an explanation of the analysis techniques used. The results are then presented, followed by a discussion of the results, particularly in view of previous research as well as the results from the previous chapter. The findings are also discussed in the context of the global configuration of the magnetosphere and how this configuration may impede activity in the magnetotail.

5.2 Methodology

5.2.1 Selection of dataset

In the previous study, the number of current sheet crossings per orbit for Cluster 3 in the 2001-2007 tail seasons was identified. Orbits in which there were large data gaps (> 480 s) and in which the H^+ density was greater than 1.5 cm^{-3} were excluded to avoid missing any crossings or including crossings in the magnetosheath. The previous study [Davey *et al.*, 2012] also investigated various thresholds in B_X (± 3 nT, ± 5 nT and ± 7 nT) to define a crossing. The ± 5 nT threshold was shown in the previous chapter to be a sensible threshold for identifying current sheet crossings. Consequently, the ± 5 nT threshold for a change in B_X was used to define a crossing when the spacecraft was located at $X < -8 R_E$ and $|Y| < 10 R_E$. In this study, a similar set of criteria are used to identify those orbits with large data gaps or in which the spacecraft passed into the magnetosheath. However, in this study the current sheet crossings are identified using the barycentric magnetic field data from the Cluster spacecraft, estimated to be the average magnetic field across all four spacecraft.

5.2.2 Data analysis methods

For each crossing, the barycentric magnetic field (that is the magnetic field at the centre of mass of the spacecraft tetrahedron) was estimated as the mean magnetic field across the four spacecraft. The FGM 5 Hz resolution data were employed, box-car averaged and re-binned to a 1 second resolution. Only those crossings which involved a current sheet crossing within the barycentric data were used for the study.

Minimum variance analysis (MVA) [Sonnerup and Scheible, 1998] was used to identify the direction of maximum variance (\mathbf{I}) in the barycentric magnetic field

data for each crossing. All crossings included in the dataset had a ratio of maximum to intermediate variance eigenvalues of greater than 4. The curlometer technique [Dunlop *et al.*, 1988; Robert *et al.*, 1998] was used to estimate the magnitude and direction (\mathbf{m}) of the current density throughout the crossing. A cross product of the current density direction (\mathbf{m}) and the maximum variance direction (\mathbf{l}) provides an estimate of the direction normal to the current sheet (\mathbf{n}). The angle that the normal direction makes with the Z (GSM) axis ($\arctan(|n_Y|/|n_Z|)$) was defined as the tilt angle of the current sheet during each crossing. The effective position from the centre of the current sheet, or vertical scale along the normal (Z^*) was calculated using

$$Z^*(t) = \int_{t_1}^{t_2} \frac{\partial B_l}{\partial t} [\nabla_n B_l]^{-1} dt \quad (5.1)$$

taken from Runov *et al.* [2005a], where ∇_n is the gradient in the normal direction of the current sheet and B_l is the component of the magnetic field in the direction of maximum variance. When the current density is plotted as a function of Z^* it provides a profile of the current density and the half thickness of the current sheet can be estimated.

As discussed in Section 3.4.2, the curlometer technique assumes that the magnetic field varies linearly between the spacecraft. It estimates the current density within the tetrahedron and is a combination of the estimates of the current density through the faces of the spacecraft tetrahedron. In the calculations, the divergence of the magnetic field deviates from Gauss's Law, from errors in the data and the assumptions used in the curlometer technique, and is used to provide a measure of the accuracy of the estimates. The accuracy of the technique is lowered when there is a large separation between the spacecraft, forming the tetrahedron as the assumptions about linear changes between spacecraft are less valid. In addition, if the spacecraft separation is too large in comparison to the current sheets studied, then the current sheet may not be able to be fully resolved by the technique. This was discussed in Section 3.4.2. Crossings were included if the accuracy of the

current density estimate, indicated by the ratio of div B to curl B , was less than 0.3 for more than 60% of the crossing. This threshold has been selected as it has been used in previous work [Runov *et al.*, 2005a]. The database of crossings used in the present study comprised 279 crossings. For each crossing within the database, the SYM-H and AE indices at the time of the crossings i.e. where the barycentric $B_X=0$, were used to identify whether the ring current was enhanced and whether substorms were present.

5.3 Results

5.3.1 Current sheet orientation

Figure 5.1 shows how the current sheet tilt angle varies with the SYM-H (panel a) and AE (panel b) indices at the time of each crossing. When SYM-H is < -70 nT (in panel a), the tilt angles are $< 25^\circ$. In addition there are very high values of tilt angle, approaching 90° , that occur when SYM-H is positive and also when it is negative down to about -50 nT. In addition, the scatter of values increases as SYM-H increases (up to about +20 nT). The variation of tilt angle with the AE index is however not so clear (panel b). For the purposes of this work, the SYM-H index is used to give an indication of when the ring current is enhanced and therefore storm conditions are defined to be when SYM-H values are ≤ -50 nT as in the previous study. In view of this, the tilt angle variation with the AE index for non-storm times (where SYM-H > -50 nT) is indicated by the black data points and storm-times (where SYM-H ≤ -50 nT) by the red data points. For large AE values (> 500 nT) the non-storm times (black data points) have, in general, higher tilt angles than the storm-time data (red data points), although there are fewer data in this region compared to where $\text{AE} < 500$ nT. For lower values of the AE index, there is a wide range of tilt angles, with most crossings having tilt angles of less

than 25° . However there are also some crossings with tilt angles of $> 60^\circ$ when the AE index is low and in general there is no obvious trend for AE values < 500 nT.

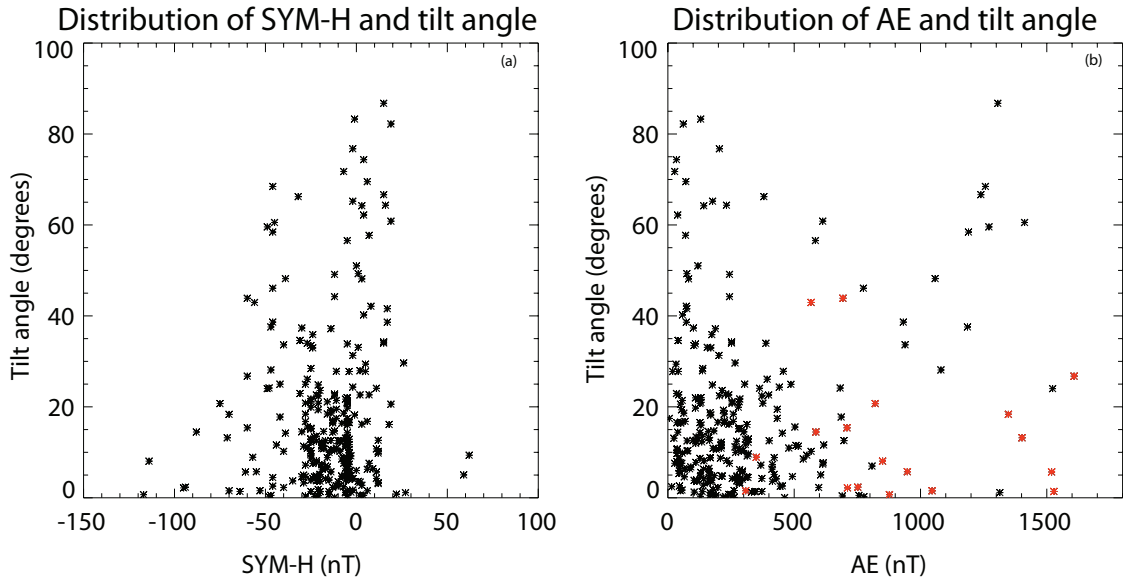


Figure 5.1: Distributions of tilt angle for each crossing, with SYM-H (panel a) and the AE index (panel b). In panel (b), black data points represent those crossings where $\text{SYM-H} > -50$ nT and the red data points are where $\text{SYM-H} \leq -50$ nT. The values of SYM-H and the AE index used are those at the point of the crossing where $B_X = 0$.

In order to view the distributions more clearly, Figure 5.2 shows the mean tilt angle in bins of SYM-H (panel a) and AE (panel b). As in Figure 5.1, Figure 5.2(b) shows non-storm time data in black with storm data in red. Vertical lines through each bar indicate the standard errors on the means and the numbers in each bin are shown above each bar. There is a peak in mean tilt angle where SYM-H is between 0 and 50 nT in panel (a), with a decrease in tilt angle as the bins approach -150 nT. In panel (b) the mean tilt angle increases with higher values of the AE index, although the number of data points decreases above 500 nT. To investigate the significance of the relationship with the AE index, the Mann-Whitney-Wilcoxon test was applied [Barlow, 1989], which was discussed in Chapter 3. When comparing the tilt angles in a group with low AE indices (< 500 nT) compared to a group with high AE indices (≥ 500 nT), for non-storm times only ($\text{SYM-H} > -50$ nT), the mean tilt angle

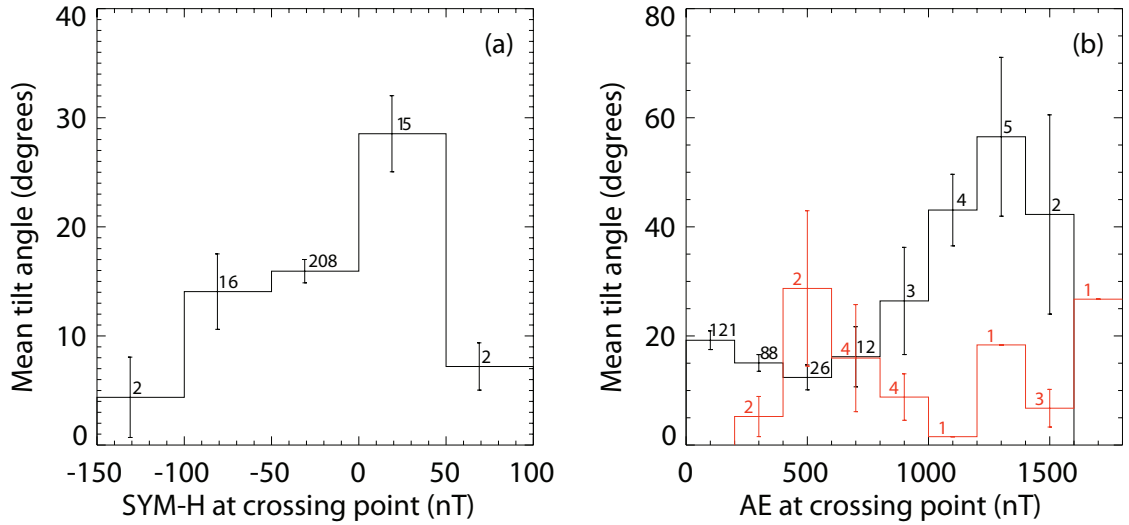


Figure 5.2: Distributions of mean tilt angle as a function of SYM-H (panel a) and the AE index (panel b). Panel (a) shows the data in 50 nT bins and panel (b) shows the data in 250 nT bins. In panel (b), those crossings where SYM-H > -50 nT are shown in black and SYM-H ≤ -50 nT are the red data. The values of SYM-H and the AE index used are those at the point of the crossing where $B_X = 0$. Standard errors of the means are shown by vertical lines through each bar and the numbers in each bin are above each bar.

for the lower AE group is 16.95° and 27.60° for the high AE group. The Mann-Whitney-Wilcoxon test shows that the two groups are statistically different to a 95% level.

In order to see any trends in tilt angle with position, the mean tilt angle of the current sheet for groups of crossings in $1 R_E$ bins, at different positions in the magnetotail is plotted in black in Figure 5.3. The positions used are the start of each crossing in X (panel a), Y (panel b) and Z (panel c) in GSM coordinates. Standard errors on the mean values are indicated by vertical lines through each data point. The numbers within each bin are indicated by the red bars (scale on the right hand side). The variation in the tilt angle with position in the X direction does not show any significant variation (panel a). Some of the bins contain only small numbers of crossings, particularly at the extremes in X and Z. Larger tilt angles are evident in the dawn flank of the tail compared to those around $Y=0$ (panel b).

There is no evidence that there are increased tilt angles on the dusk flank of the tail, although it should be noted that the data are restricted to $|Y| < 10 R_E$, so it is impossible to ascertain whether the tilt angles increase further into the dusk flank. Panel (c) shows larger tilt angles at larger Z values.

Figure 5.4 shows the mean tilt angle for three different levels of geomagnetic activity i.e. during quiet times, substorms and magnetic storms (indicated by an enhanced ring current). The data were separated according to the AE and SYM-H indices at the time of each crossing. Quiet conditions (QT) were defined as SYM-H > -50 nT and AE < 500 nT. Substorm conditions (AE) were defined as SYM-H > -50 nT and AE ≥ 500 nT and finally storm conditions with an enhanced ring current (RC) were defined as SYM-H ≤ -50 nT and AE ≥ 500 nT. It should be noted that the two crossings that occurred during enhanced ring current conditions with low values of the AE are not included in the analyses of the three groups mentioned previously, as the aim is to compare the effect of the ring current under similar AE conditions. Standard errors on the means are shown by vertical lines through each data point and the numbers in each group are shown above each bar. The tilt angle is largest for the substorm group (AE) whereas the enhanced ring current group (RC) has the lowest mean tilt angle. The Mann-Whitney-Wilcoxon test was again used to compare the QT and AE groups and the AE and RC groups. The differences between those groups was statistically significant to a 95% level.

Since the Cluster orbit changes from one year to the next the tilt angle for different geomagnetic conditions are compared for the first four years of data in Figure 5.5. The years 2005-2007 are not shown in this figure, as there are no crossings in the ‘RC’ group, which would allow a comparison across all three levels of geomagnetic activity for these years. The classification of the different geomagnetic groups is the same as in Figure 5.4. Standard errors on the means are shown by vertical lines through each data point and the numbers in each group are shown above each bar. The mean values of SYM-H and the AE index, for each of the

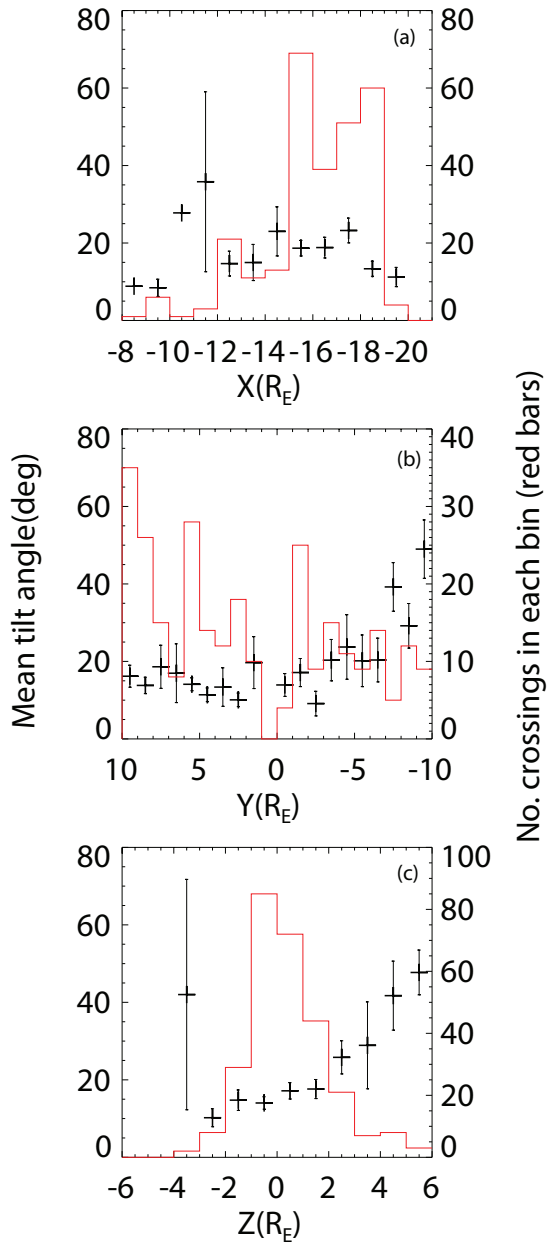


Figure 5.3: Mean tilt angle of the current sheet at the position of the start of the crossings, in terms of X(panel a), Y(panel b) and Z(panel c) in GSM coordinates. Data is presented in $1R_E$ bins and the standard errors in the mean values are shown by vertical lines through each data point. The secondary Y axis shows the numbers in each bin group, indicated by the red bars.

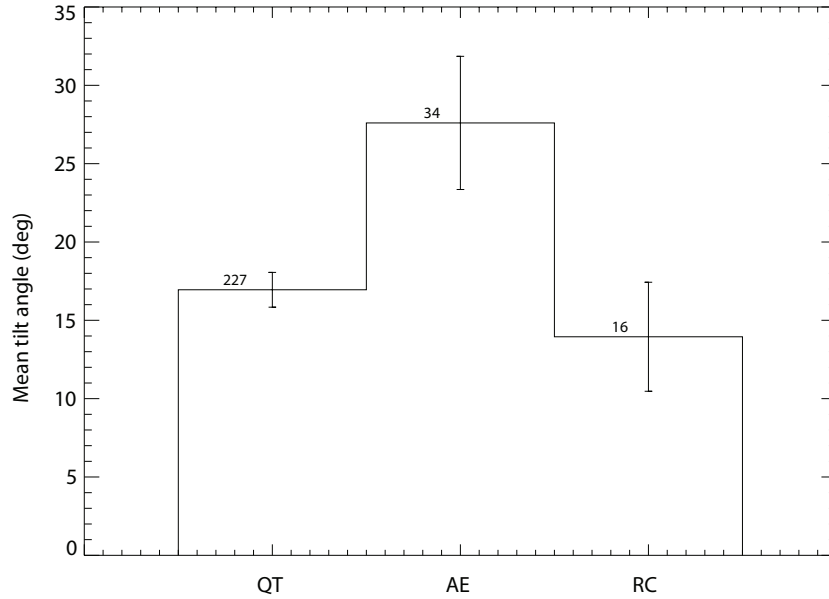


Figure 5.4: Mean tilt angle for different geomagnetic conditions for 2001-2007 data. ‘QT’ represent those crossings where $\text{SYM-H} > -50$ nT and $\text{AE} < 500$ nT. The ‘AE’ data include all crossings where $\text{SYM-H} > -50$ nT and $\text{AE} \geq 500$ nT. The ‘RC’ group are crossings where $\text{SYM-H} \leq -50$ nT and $\text{AE} \geq 500$ nT. Standard errors in the means are shown by vertical lines through each data point and the numbers in each group are shown above each bar.

groups, are also shown next to each plot. Panels (a)-(c) show that for 2001-2003, the ‘AE’ group has larger tilt angles compared to the ‘QT’ and ‘RC’ groups, although large variability is seen in the ‘AE’ group in 2002 and 2003. In 2004 (panel d), the ‘AE’ group has a lower value of mean tilt angle compared to the other groups. The largest difference between the mean tilt angles of the ‘AE’ and ‘RC’ groups is in 2001 (panel a) where the mean SYM-H value for the ‘RC’ group is -102 nT. In 2004, where the ‘RC’ group tilt angle is larger than the ‘AE’ group and the data do not follow the pattern of years 2001-2003, the mean SYM-H value for the ‘RC’ group is -59 nT, indicating a much less enhanced ring current than in the earlier years. Figure 5.5 indicates that there may be more of an effect of an enhanced ring current on the tilt angle when SYM-H is more negative as in 2001, compared to the later years when the values of SYM-H are less negative.

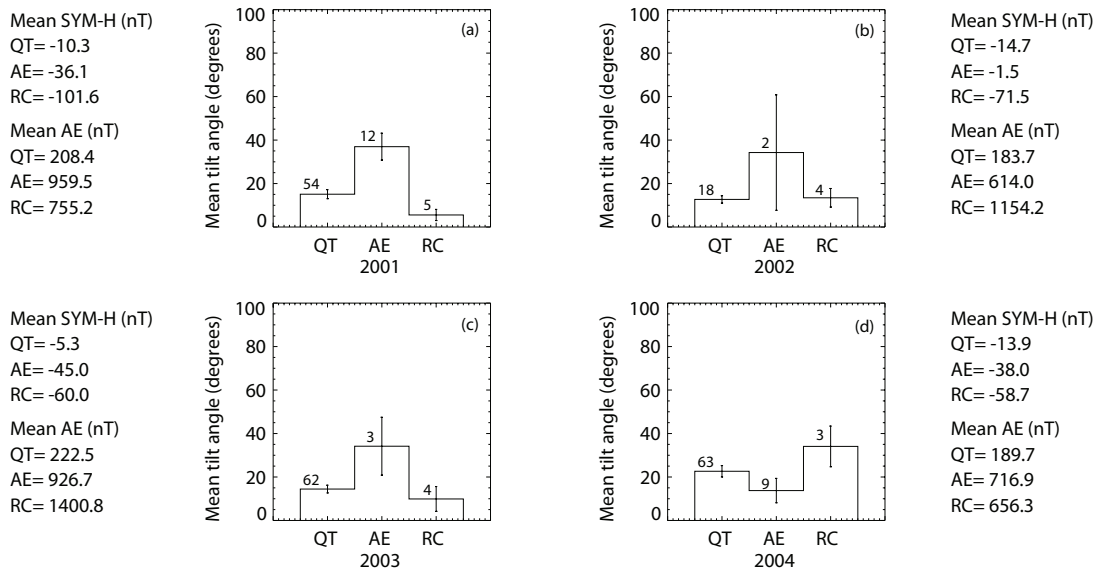


Figure 5.5: The mean tilt angle for different geomagnetic conditions for 2001-2004 only (panels a-d). For each panel, ‘QT’ represents those crossings where $\text{SYM-H} > -50$ nT and $\text{AE} < 500$ nT. ‘AE’ includes all crossings where $\text{SYM-H} > -50$ nT and $\text{AE} \geq 500$ nT. ‘RC’ is a group of crossings where $\text{SYM-H} \leq -50$ nT and $\text{AE} \geq 500$ nT. Standard errors in the means are shown by vertical lines through each bar and the numbers within each group are shown above each bar.

5.3.2 Current sheet current density

In this section, the current density in the magnetotail current sheet is analysed with respect to position and geomagnetic activity, in a similar manner to the treatment of the current sheet tilt angle in Section 5.3.1. For each crossing, the maximum current density magnitude reached was calculated and Figure 5.6 shows the spatial distribution of the means of those maximum current density values in $1R_E$ bins in the (a) X, (b) Y and (c) Z GSM directions. As in Figure 5.3 some of the bins have smaller numbers of crossings and should be treated with caution. The mean current density magnitude shows no obvious trend with position, unlike the current sheet tilt angle (Section 5.3.1).

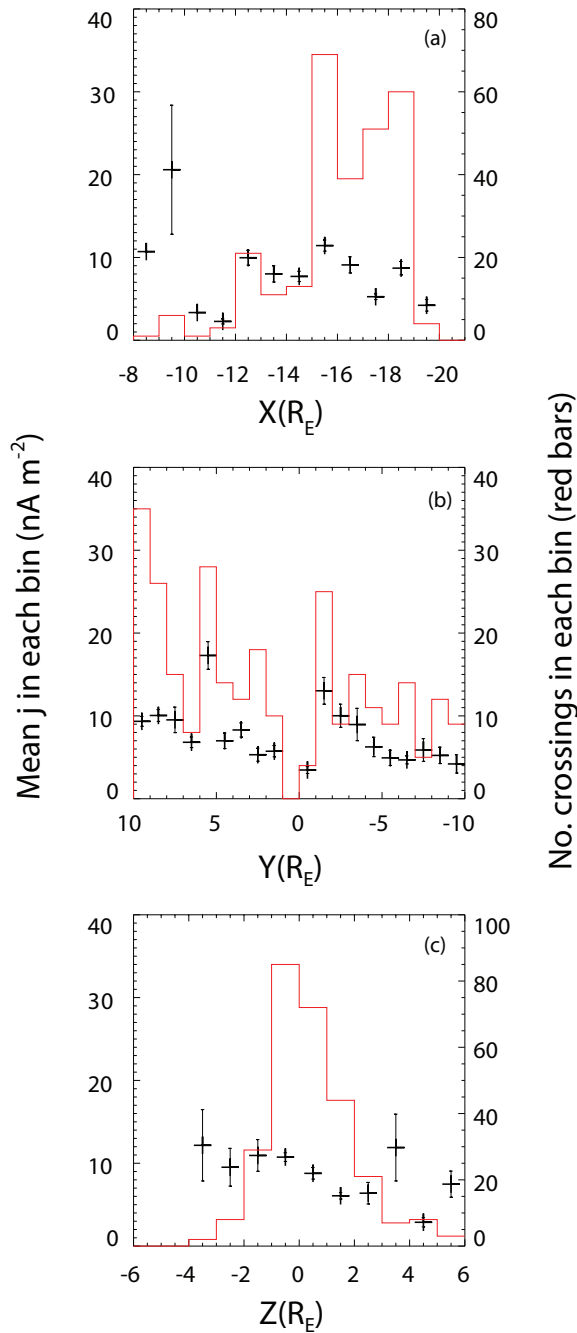


Figure 5.6: The means of the maximum current density magnitude reached in each crossing (using the left hand Y axis) for 2001-2007 data, in 1 R_E bins of the starting position of the crossings in X (panel a), Y (panel b) and Z (panel c) (GSM coordinates). Standard errors in the means are shown by vertical lines through each data point. The right hand side axis shows the numbers in each bin, indicated by the red bars.

In Figure 5.7 the mean current density magnitude is plotted as a function of Z^* in $0.1 R_E$ bins, for each of the geomagnetic condition groups described earlier, using all the data from 2001-2007. The mean current density magnitude within each bin of Z^* was calculated for each crossing and Figure 5.7 shows the means of those values for each geomagnetic activity group. The quiet conditions group (QT) is shown in red, the high AE index group (AE) is shown in green and the enhanced ring current group (RC) is in blue and they are defined in the same way as in previous figures. The standard errors on the mean values are indicated by vertical lines through each data point. When the data are considered together in this way, the ‘RC’ and ‘QT’ groups have larger maximum current densities than the ‘AE’ group, particularly in the central section of the current sheet, around $Z^*=0$.

As with the tilt angle study (Section 5.3.1), separating the data into the first four years of data enables a comparison of geomagnetic conditions within each tail season as well as an investigation of the effect of increasing strengths of the ring current. The mean current density data as a function of Z^* , in $0.1 R_E$ bins and separated by year, is presented (Figure 5.8) for the first four years of data where there are enough data to allow comparisons of all three geomagnetic condition groups. The mean values of SYM-H and AE are given for each group next to the panels. The geomagnetic conditions are indicated by the same colours as in the previous figure. Standard errors on the mean values are shown by vertical lines through each data point. Data from 2001 and 2002 show a larger maximum current density magnitude for the ‘RC’ group compared to the ‘AE’ and ‘QT’ groups. However, 2003 and 2004 data do not show the same results, with the ‘RC’ group having similar maximum current density values as the ‘AE’ group. It is interesting to note that for 2001 and 2002, the mean SYM-H values for the ‘RC’ group are more negative, indicating a more enhanced ring current, compared to years 2003 and 2004. In addition, the ‘QT’ groups in each year show a variation in magnitude of the maximum current density even though the mean AE and SYM-H

values for the QT groups are fairly similar in each year. This effect may be due to the spacecraft separation, with larger current densities found in 2003 at the smallest separation ($0.03 R_E$) and smaller values at larger separations.

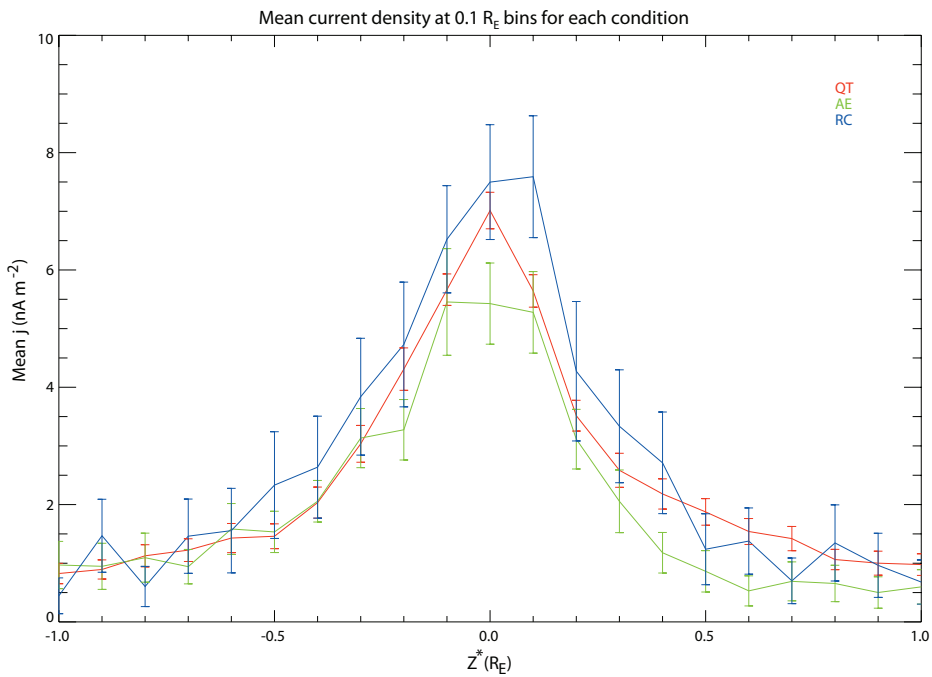


Figure 5.7: Mean current density magnitude for different geomagnetic conditions for 2001-2007 data, in $0.1 R_E$ bins of Z^* . The red data (QT) represent those crossings where $\text{SYM-H} > -50$ nT and $\text{AE} < 500$ nT. The green data (AE) include all crossings where $\text{SYM-H} > -50$ nT and $\text{AE} \geq 500$ nT. The blue data (RC) are crossings where $\text{SYM-H} \leq -50$ nT and $\text{AE} \geq 500$ nT. Standard errors in the means are shown by vertical lines through each data point.

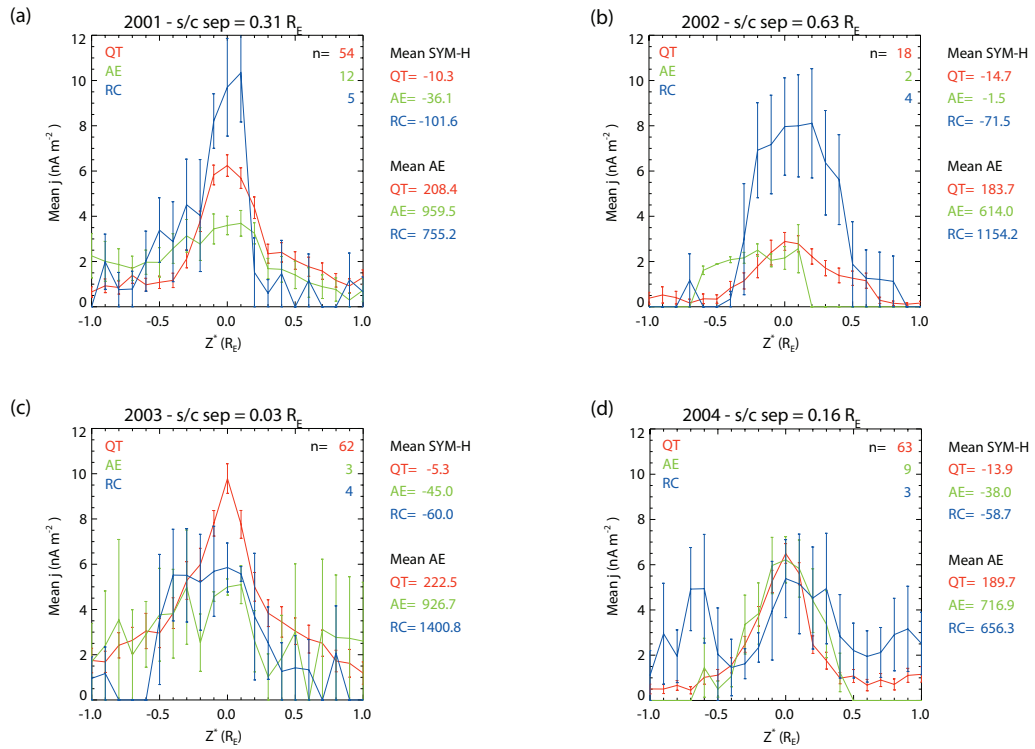


Figure 5.8: Mean current density magnitude for different geomagnetic conditions for 2001-2004 data (panels a-d), in $0.1 R_E$ bins of Z^* . The red data (QT) represent those crossings where $\text{SYM-H} > -50$ nT and $\text{AE} < 500$ nT. The green data (AE) include all crossings where $\text{SYM-H} > -50$ nT and $\text{AE} \geq 500$ nT. The blue data (RC) are crossings where $\text{SYM-H} \leq -50$ nT and $\text{AE} \geq 500$ nT. Standard errors in the means are shown by vertical lines through each data point. The numbers in each group are shown in the top right hand corner of each plot.

5.4 Discussion

This investigation focused on the cross-tail current sheet and studied its orientation in the YZ plane and current density. Data from Cluster's 2001-2007 tail seasons was used to examine whether the orientation and current density of the current sheet varied with three different levels of geomagnetic activity, defined using the AE and SYM-H indices.

Past research on the structure of the current sheet was discussed in Chapter 2. The studies concerning current sheet orientation have shown that when the current sheet is active (during flapping motion), it can be highly tilted in the YZ GSM plane and that this tilt is reduced during periods of inactivity when the current sheet is not undergoing flapping motion. Whilst these studies have indicated that the current sheet tilt is highly variable, there had been no systematic study of which factors stabilise the variation prior to the current work. One might assume that a combination of the conclusions from the previous chapter with past research, would conclude that the orientation varies with geomagnetic activity, although this had not been shown directly.

Observations of current sheet density have shown that it can range from less than 10 nA m^{-2} [Shen *et al.*, 2008; Sergeev *et al.*, 2003] to values as high as 30 nA m^{-2} [Runov *et al.*, 2005b, 2006]. Comparing these studies indicates that the current density in the current sheet tends to be larger when the sheet is active, but prior to the current study this had not been shown statistically nor had any physical mechanism been proposed to explain this.

Using data from the 2001-2007 Cluster tail seasons, all four spacecraft were employed in this study to provide current density and orientation estimations. The SYM-H and AE indices were used as measures of geomagnetic activity at the time of each crossing of the current sheet. The work in this chapter examined whether or not the tail is more inclined towards the flanks and whether or not the tail is more

highly inclined during periods of greater geomagnetic activity. It also investigated the current density within the sheet and how it varies with geomagnetic activity.

5.4.1 Tilt angle analysis

There was some indication from Figures 5.1 and 5.2 that there was a smaller tilt angle in crossings where the ring current was enhanced, implying that during magnetic storms the current sheet may be stabilized in terms of its orientation. The relationship with the AE index shown in Figure 5.2 implied that crossings of the current sheet during non-storm times had larger tilt angles than those during storm conditions and that the tilt angle increased with increasing AE, although the number of data points above 500 nT were fewer than where the $AE < 500$ nT. Figure 5.3 showed that the tilt angle also varied with position of the crossing. It suggested that the tilt angle may be slightly larger in the dawn flank (Y GSM direction) and at larger values of Z(GSM). The observation at high Z values is to be expected as the Cluster tail season occurs when the neutral sheet is located at positive Z, due to the tilt of the Earth. *Tsyganenko et al.* [1998] showed that the magnetotail current sheet is tilted away from the XY plane, with this warping increasing towards the flanks. As such, higher tilt angles at the flanks of the magnetosphere would be expected as the current sheet is naturally tilted away from the XY plane at these locations. The effect of the IMF B_Y on the tilt in the YZ plane was shown to be larger with increasing distance downtail as *Tsyganenko et al.* [1998] considered distances up to 100 R_E downtail. The effect of IMF B_Y has not been considered in this study, although based on the data from *Tsyganenko et al.* [1998], an estimation of the effect is between 6-9°, for IMF $B_Y = 10$ nT, in both flanks at the downtail distances considered in the study. Later, *Tsyganenko and Fairfield* [2004] performed model calculations based on GEOTAIL and Polar data and found a similar warping of the current sheet as found in the earlier study, which increased with increasing distance downtail and varied with solar wind dynamic pressure and

IMF B_Y .

The overall picture of the tilt data (Figure 5.4), comparing geomagnetic conditions for 2001-2007, clearly demonstrated the increased tilt angle during high values of the AE index and lower tilt angles during quiet and storm times. The first four years of data were then considered (Figure 5.5) and for 2001-2003 the groups of crossings with the enhanced ring current (RC) had lower tilt angles than the groups with the large AE indices and a quiet ring current (AE), although there was large variation for the AE group in 2002 and 2003. In contrast, 2004 did not follow this pattern. However, when the mean values of SYM-H for the enhanced ring current groups (RC) were compared, it was clear that the mean value of SYM-H for 2004 was more positive than in the previous years. The results suggest that crossings occurring when there is an enhanced ring current have a lower current sheet tilt angle, especially with increasing strength of the ring current.

The range of tilt angles calculated in this study are in agreement with those observed by others such as *Zhang et al.* [2002], *Runov et al.* [2005a] and *Sergeev et al.* [2003, 2004]. The larger tilt angles noted by others were generally found in flapping current sheets. Although this study did not investigate current sheet flapping, the last chapter found that current sheet flapping was associated with enhanced substorm conditions. The present study found that increased substorm conditions are associated with larger tilt angles and as such the combination of the studies from both chapters so far presented are in agreement with the previous studies. In addition the study discussed in the last chapter found that during magnetic storms, the flapping motion was generally decreased. Other work [*Petrukovich et al.*, 2005] showed lower tilt angles for an inactive current sheet. The present study, showing that during magnetic storms there are on average lower tilt angles, is again in agreement with what might be surmised on combining studies such as *Petrukovich et al.* [2005] and the previous chapter.

5.4.2 Current density analysis

The current density analysis also separated the data into geomagnetic condition groups and Figures 5.7 and 5.8 both showed that the groups of crossings with an enhanced ring current (RC) had higher maximum current densities compared to the other groups, specifically the group with high values of the AE index and a quiet ring current (AE). Research by, for example, *Runov et al.* [2003], *Runov et al.* [2006] and *Sergeev et al.* [2003], have shown a bifurcated structure of the current sheet. The exact processes which form a bifurcated current sheet are still unresolved. However *Zelenyi et al.* [2002] proposed that the mechanism involved the scattering of ions and the decay of the current sheet and *Greco et al.* [2002] suggested that the cause of bifurcated sheets could be localised magnetic turbulence in the central part of the current sheet. *Runov et al.* [2006] studied 30 rapid current sheet crossings using 2001 Cluster data and found that 5 out of those were bifurcated. They found no AE-dependence on the different types of thickness of current sheet. The present study did not restrict the duration of crossings and as such an estimation from the *Runov et al.* [2006] data cannot be made of how many of the crossings in the present study would be classified as bifurcated in structure. It is possible that bifurcation did occur in a proportion of the crossings and as such any averaging may have reduced the current density at $Z^*=0$. However, it cannot be assumed that this would have occurred in one group more than the other groups and as such any corrections for possible bifurcation have not been included. The lower current density for the ‘AE’ group may be due to the diversion of the tail current into the ionosphere during the onset of the expansion phase of a substorm, although the data have not been separated according to the substorm phase and so this has not been assessed. Figure 5.7 also shows a slightly wider current profile for the ‘RC’ group compared to the other geomagnetic condition groups, implying a larger half thickness. Estimates of half thickness taken from Figure 5.7 are approximately $0.4 R_E$ (≈ 2500 km) for the ‘RC’ group, $0.26 R_E$ (≈ 1700 km) for the ‘QT’ group

and $\approx 0.24 R_E$ (≈ 1500 km) for the ‘AE’ group. These are values taken from average current density estimates for groups of crossings. They are however in agreement with previous estimations, such as *Sergeev et al.* [2003] who found a half thickness of $0.36 R_E$ for a current sheet flapping event in 2001 and also by *Rong et al.* [2011]. *Runov et al.* [2005b] cited half thickness values of $\leq 0.16 R_E$ for the majority of fast current sheet crossing events studied. A larger range of values was calculated by *Runov et al.* [2005a] (0.24 - $1.57 R_E$) for a statistical study of 78 rapid current sheet crossings, and later *Runov et al.* [2006] found typical values of $< 0.31 R_E$ and $0.63 R_E$ (for bifurcated current sheets) for fast crossings during Cluster’s 2001 tail season.

If the averaged estimates of half thickness are considered to be accurate then spacecraft separations of 0.16 - $0.31 R_E$ should be adequate to resolve the current densities for the crossings and as such 2001 and 2004 data in Figure 5.8 should show good estimates of the current density profiles for each group. In contrast, the values in 2002 at $0.63 R_E$ separation may have underestimated the values somewhat for all groups. *Forsyth et al.* [2011] noted that the curlometer technique underestimates the current density, although it improves for larger current widths and that in simulations of an infinitely thin current sheet, the curlometer estimates about 20% of the input current. They stated that if the ratio of the current width to the spacecraft separation is greater than or equal to 0.5, the curlometer detects about 80% of the current. In addition, *Runov et al.* [2005a] calculated that the current density magnitude could be underestimated up to 30% and the half thickness up to 15%. This was calculated from model simulations and by comparing a regular tetrahedron shape to an irregular shape, using Cluster 2001 spacecraft separation and configuration data. The ‘QT’ groups in 2001 and 2004 show similar profiles. The ‘AE’ group has larger maximum current density in 2004, with a slightly lower mean value of the AE index than in 2001. However, the ‘RC’ group has a larger maximum current density in 2001, where the mean value of SYM-H for the group

is more negative than in 2004, indicating a possible effect of the strength of the ring current on the current density. In general, larger current densities are seen in the ‘RC’ group for years 2001 and 2002 where the mean SYM-H values are less than -70 nT. However in the later years, the mean current density values of the ‘RC’ groups are very similar to the ‘AE’ groups and here the mean SYM-H values are -59 nT (2003) and -60 nT(2004) for the ‘RC’ groups. The results demonstrate that as with the tilt angle, the strength of the ring current may affect the magnetic configuration of the magnetosphere such that the current density within the current sheet during a crossing is higher when SYM-H is less than about -70 nT, implying moderate storm activity.

The current density values estimated in this study are also in agreement with those noted in previous work such as *Rong et al.* [2011]; *Runov et al.* [2005a, 2006]; *Shen et al.* [2008]; *Sergeev et al.* [2003]; *Petrukovich et al.* [2007], with observations of maximum current density of less than 10 nA m^{-2} as well as values over 30 nA m^{-2} for individual crossings. The mean values in specific groups have been presented for the purposes of the analysis, rather than individual crossings.

Previous work by *Milan et al.* [2008] showed that the magnetotail contains more open flux during magnetic storms, suggesting that it becomes stabilized to substorm initiation at these times and that more open flux is needed for reconnection to occur. The previous study found that when the ring current is enhanced the current sheet is stabilized in terms of its motion. It also found that there is more motion when the standard deviation of the AE index implies stronger substorm activity and a quiet ring current. The results from this study suggest that the enhanced ring current also has an effect of reducing the tilt angle of the current sheet, when SYM-H values are approaching -100 nT. In addition, the results show an increased tilt angle of the current sheet during times when the AE index is $\geq 500 \text{ nT}$, implying strong substorm activity. Further, the results show larger current densities during storm times compared to quiet and substorm times.

5.5 Conclusions

An investigation was carried out of the orientation and current density within the cross-tail current sheet for current sheet crossings between 2001 and 2007, using the Cluster spacecraft.

The results suggest that crossings occurring when the AE index is large (>500 nT) with a quiet ring current involve larger values of tilt angle and a reduced current density during crossings than compared to quiet times. In contrast, crossings during substorms but with an enhanced ring current (during magnetic storms) involve a reduced tilt angle and an increased current density, with the strength of the enhanced ring current possibly playing a role in how much the current density and tilt angle are affected. It is proposed that the increased amount of flux in the lobe during magnetic storms, suggested by *Milan et al.* [2008], causes an increased pressure on the current sheet, causing it to not only have a reduced motion as found by the previous chapter, but also a smaller tilt angle in the YZ plane during each crossing and a larger current density caused by the larger change in B_X in the lobes.

Chapter 6

Magnetotail lobes

6.1 Introduction

This chapter describes the final data study within this thesis. Chapters 4 and 5 have shown how the current sheet dynamics and structure (in terms of its orientation, current density and thickness) vary depending on different levels of geomagnetic activity. The final study considers the lobes of the magnetotail, which are important regions for energy storage within the magnetosphere as discussed in Chapters 1 and 2. As more open flux is moved to the nightside to form the magnetotail, an open question remains regarding how the magnetic field within the lobes compare during different geomagnetic conditions. This chapter describes work that employed Cluster 3 spacecraft data during its 2001-2007 tail seasons, as well as the AE and SYM-H indices during these times.

6.2 Lobe selection

The list of part-orbits through the magnetotail current sheet from the first data study (Chapter 4) were used as a basis for the work within this study. Data prior to

the first current sheet crossing within each orbit and data after the last crossing of the current sheet within each orbit by the Cluster 3 spacecraft, were used to locate the lobes, using data from the FGM and CODIF CIS Cluster 3 instruments. The CIS data were employed to set a criterion for the lobe search, of H^+ number density $< 0.1 \text{ cm}^{-3}$ and H^+ temperature of $< 500 \text{ eV}$. The values used in the criterion were selected based on typical values of number density and temperature within the lobe [Kivelson and Russell, 1995], discussed in Chapter 1. The CIS data were box-car averaged to a 1 minute resolution and the FGM data used were the 5 Hz data, both obtained from the CAA.

The term ‘lobe boundary’ will be used to describe the central edge of each lobe, which is the closest point within the lobe to the plasma sheet, within the orbital pass through the magnetotail. The time, position, total magnetic field, SYM-H and AE values were noted at the boundaries in each lobe.

The lobe magnetic field has been shown to vary with position in the X GSM direction and with solar wind dynamic pressure (e.g. Fairfield and Jones [1996], Nakai *et al.* [1991] and Nakai *et al.* [1999]). The dynamic pressure was therefore used as a measure of solar wind conditions at the times the spacecraft was at each lobe boundary. This was measured using OMNI data, lagged to the magnetopause as described in Chapter 3. The OMNI data were then lagged further by taking the average solar wind speed in the 5 minutes preceding the boundary time and the distance between the omni-lagged position and the position of the boundary in X GSM coordinates. After lagging, the average dynamic pressure in the 5 minutes around each boundary time was then used in further analysis, described in the next section.

6.3 Position and dynamic pressure influences

The variation of total lobe magnetic field with distance downtail (position of the boundary in the X GSM direction) for the data in both lobes is shown in Figure 6.1. Larger magnetic field values are evident closer to the Earth, compared to those further downtail. The data are colour-coded according to the solar wind dynamic pressure, with blue data indicating dynamic pressure values less than 3 nPa, green data for values between 3-6 nPa, moving through yellow (6-9 nPa), orange (9-12 nPa) and pink (>12 nPa). It is also clear from Figure 6.1 that those data with larger dynamic pressure are generally at larger lobe field values compared to lower pressure data at the same distance downtail. The maximum lobe field reached is 73.18 nT and the overall mean is 31.28 nT. There are 204 orbits in total in the dataset.

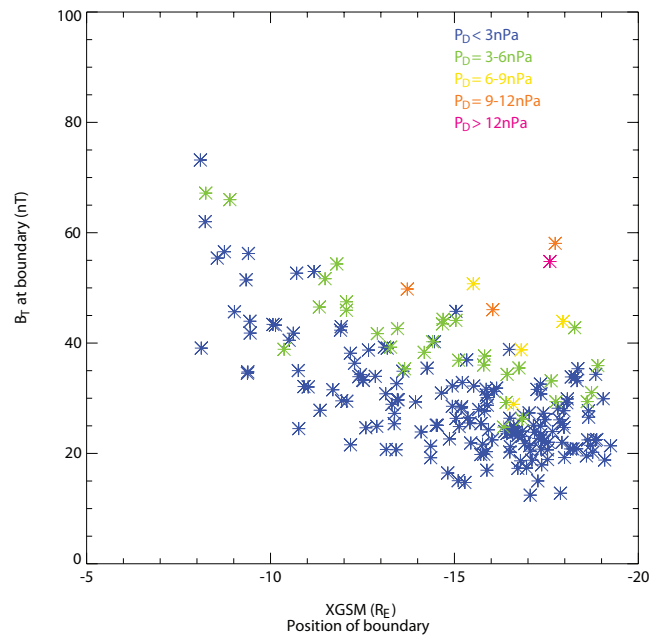


Figure 6.1: Variation of the lobe magnetic field at the lobe boundary point, with position along the X GSM direction. Data is colour-coded according to the dynamic pressure, with a full description in the text.

Figure 6.2 shows the variation of lobe magnetic field magnitude with solar wind dynamic pressure. The dynamic pressure is calculated as described in the previous section, lagged to the GSM X coordinate at the boundary. The data is colour-coded according to position in the X GSM direction, with those values between 8-10 R_E downtail being blue, 10-12 R_E downtail being dark green, going through light green (12-14 R_E), yellow (14-16 R_E), orange (16-18 R_E) and finally red (18-20 R_E). The results indicate an increase in magnetic field with solar wind dynamic pressure, with the slope of the data decreasing at high pressures. There is scatter in the data, particularly at low pressures, with those values closer to the Earth (blue and green) having higher lobe field values.

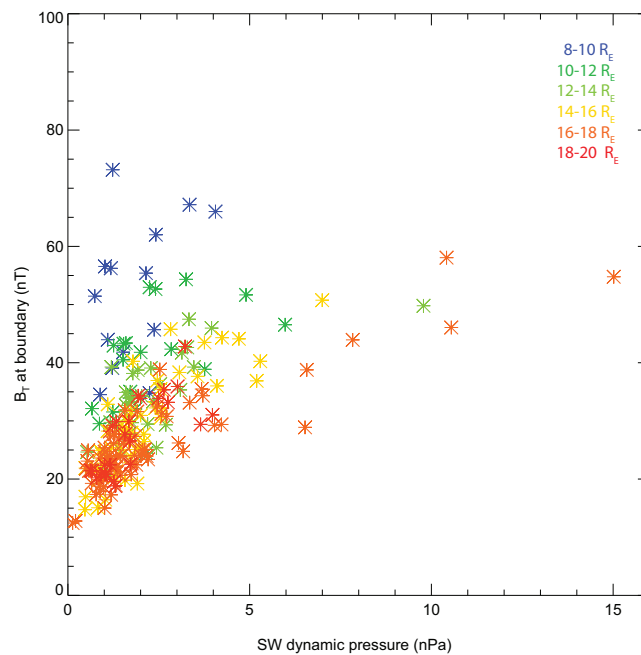


Figure 6.2: Variation of the total lobe magnetic field (B_T) at the boundary point, with solar wind (SW) dynamic pressure. Data is colour coded according to the position in the X GSM direction, with a full description in the text.

6.3.1 Normalisation

Due to the variation with both position downtail and solar wind dynamic pressure, shown in the previous section, the data were normalised to those parameters, firstly to position. Figure 6.3 shows the same data as in Figure 6.1, with coloured lines according to different relationships of lobe field with position. The orange line relates to the relationship found by *Nakai et al.* [1991] for radial distance, rather than distance in the X direction and as such will have a steeper slope in the near-Earth region; the blue line is the relationship of *Fairfield and Jones* [1996] for an analysis of data further downtail than the current study; the red line is a linear fit to the current dataset and the green line is a non-linear best fit for the current dataset, based on a fit of $B_T = 556.3 X^{-1.20} + 6.09$. The current dataset best fit (green) is clearly in agreement with the *Fairfield and Jones* [1996] relationship. The data were normalised according to the best fit of the current dataset (green).

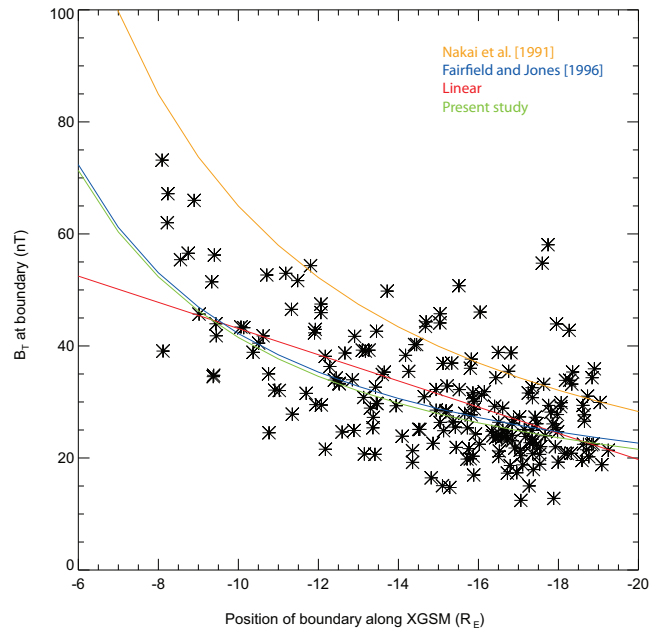


Figure 6.3: Variation of the lobe magnetic field at the boundary point, with position downtail. The coloured lines are various fits to the data, described fully in the text.

The variation of the resulting normalised magnetic field data (to distance down-tail) with solar wind dynamic pressure is shown in Figure 6.4 with an increase in lobe field with dynamic pressure. The red lines indicate two separate linear fits to the data with a steeper slope at lower pressures (<4 nPa) compared to higher pressures (≥ 4 nPa).

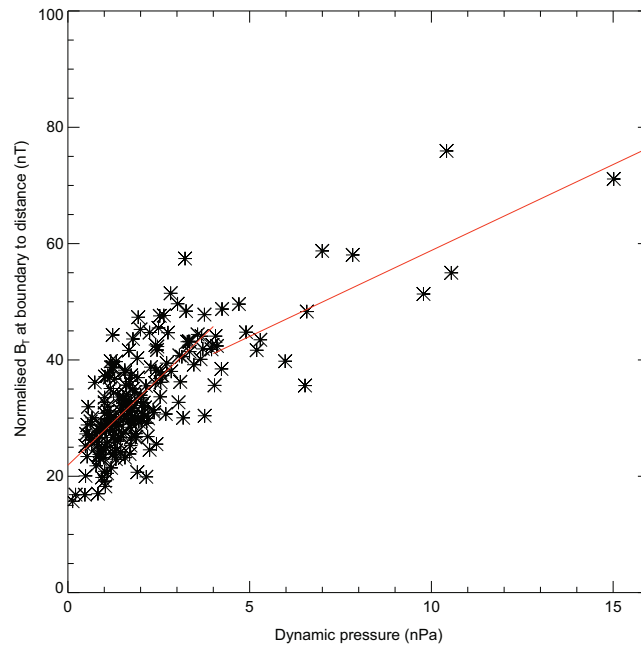


Figure 6.4: Variation of the normalised lobe magnetic field at the boundary point, with solar wind dynamic pressure. Two linear fits are shown in red for low and high pressures separately.

The data were then normalised for a second time, to dynamic pressure, using the two linear fits in Figure 6.4, for low and high pressures separately. The resulting data from both normalisation processes are shown in Figure 6.5, of normalised magnetic field with position in the X, Y and Z GSM directions. Larger lobe fields are evident at low Y and Z values compared to the outer tail regions. The maximum value reached is 41.37 nT and the overall mean of the normalised data is 31.27 nT.

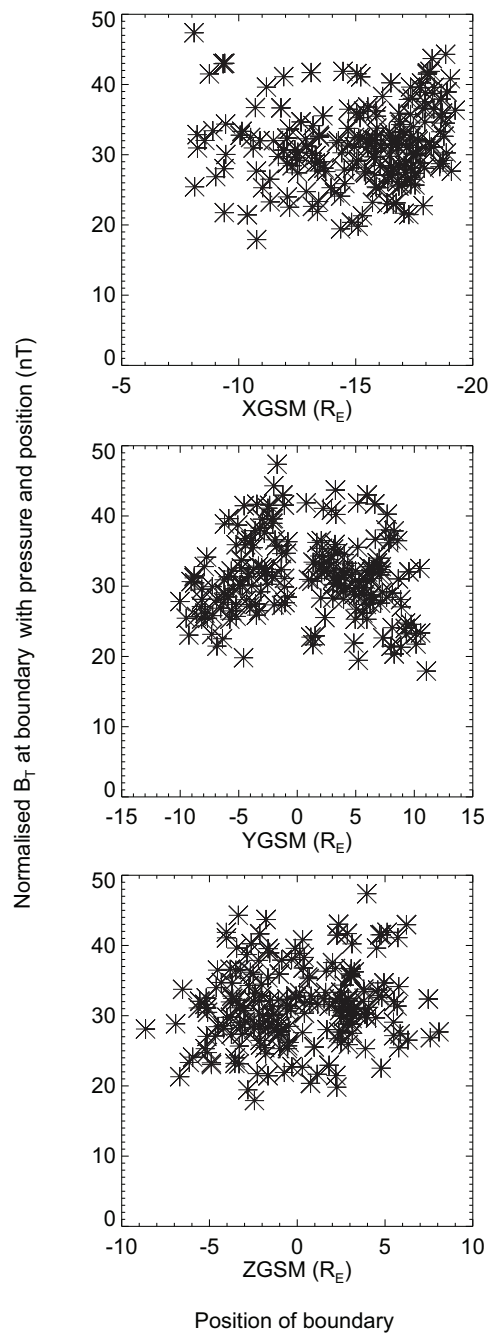


Figure 6.5: Variation of the normalised lobe magnetic field to dynamic pressure and position, with position of the boundary downtail in the X GSM (panel a), Y GSM (panel b) and Z GSM (panel c).

6.4 Influence of geomagnetic activity

A comparison of the normalised magnetic field under different geomagnetic conditions follows using the AE and SYM-H indices to indicate the presence of substorms and storms respectively.

The variation of normalised lobe field with position in the X, Y and Z GSM directions was shown in Figure 6.5. These data are shown again in Figure 6.6, although the data have been colour coded according to the AE and SYM-H conditions at the time of the measurements. Those data in red indicate where the AE index was ≥ 500 nT and the data circled in green indicate that SYM-H was ≤ -50 nT. No clear evidence of a difference between low (black) or high (red) AE values with normalised lobe field is evident. However, the stormtime data (green circles, SYM-H ≤ -50 nT) are generally in the top range of normalised lobe values, compared to non-stormtime data.

The distribution of normalised lobe field with the SYM-H value at the time that the spacecraft was at the boundary point is shown in panel (a) of Figure 6.7. The data in red show where the AE index is ≥ 500 nT. It is clear that when the ring current is enhanced (SYM-H ≤ -50 nT), there is less scatter in the data and values of normalised lobe field are all above 35 nT. Where SYM-H > -50 nT, the data range from around 18 nT to nearly 47 nT. The majority of the data at high AE values (≥ 500 nT, red) occur at negative SYM-H values. The distribution of normalised lobe magnetic field with the AE index in panel (b) of Figure 6.7 shows a large spread of data across all ranges of the AE index up to about 1200 nT with one data value at a very high value of the AE index (at about 2600 nT). The data in red show where SYM-H ≤ -50 nT. Again, the data with an enhanced ring current (in red) tend to be at larger values of normalised lobe field.

Further investigation of the magnetic storm events in both lobes where SYM-H ≤ -50 nT (red data in panel (b) of Figure 6.7) is shown in Table 6.1. The size

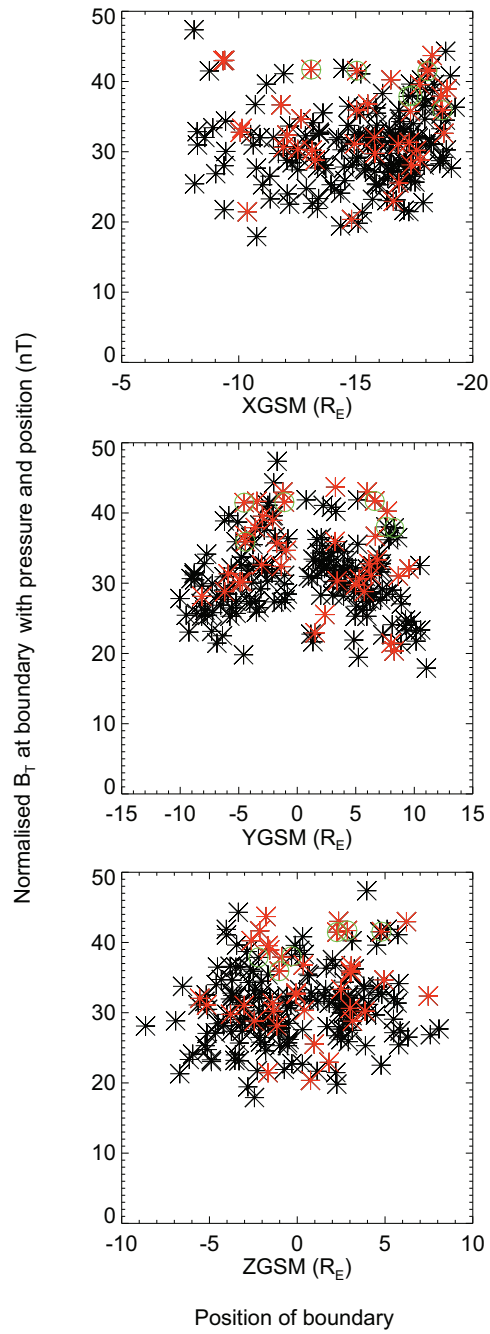


Figure 6.6: Variation of the normalised lobe magnetic field to dynamic pressure and position, with position of the boundary downtail for the north lobe (top row-panels a-c) and the south lobe (bottom row-panels d-f). Positions are shown in the X GSM (panels a and d), Y GSM (panels b and e) and X GSM (panels c and f). Red data are those where $AE \geq 500$ nT and the green circles indicate that $SYM-H \leq -50$ nT.

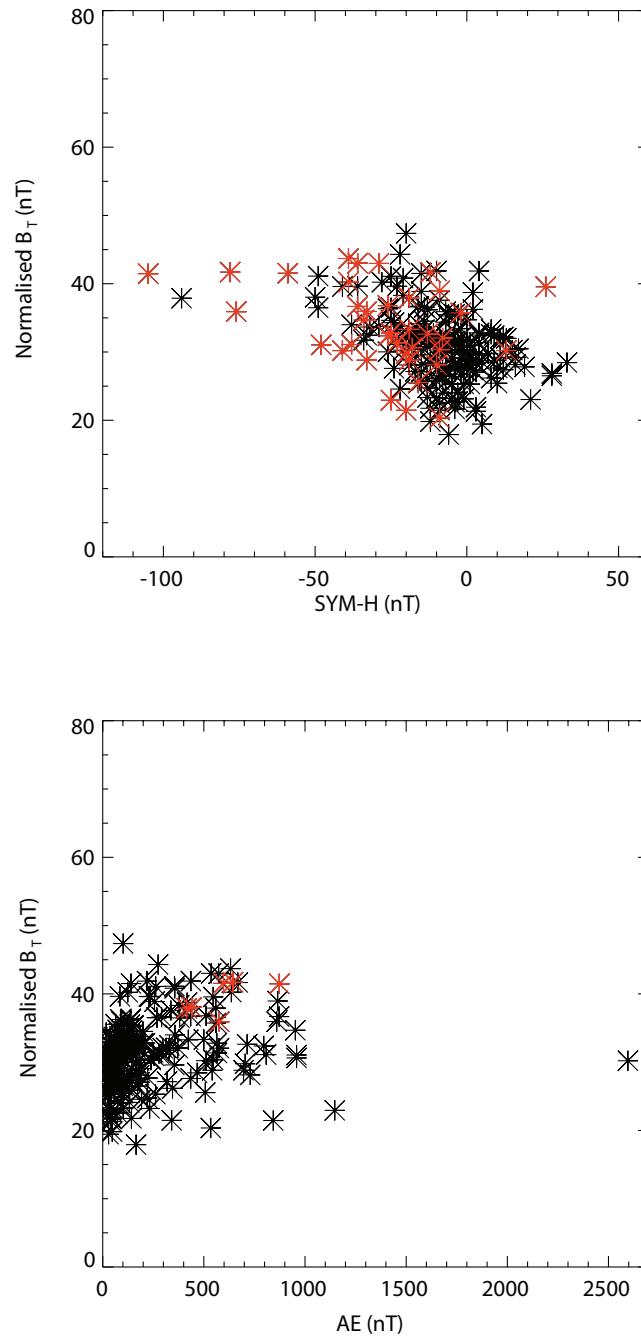


Figure 6.7: Variation of the lobe magnetic field normalised to dynamic pressure and position, with SYM-H (panel a) and the AE index (panel b). The data in red in panel (a) are where the AE index is ≥ 500 nT. The red data in panel (b) are where SYM-H is ≤ -50 nT.

of the storm (minimum SYM-H reached) and the phase of the storm occurring in each lobe pass is noted for each event. A full description of the columns is given in the caption. Events 1 and 5 are the same magnetic storm with the main phase occurring when the spacecraft was in the north lobe and the recovery phase for the south lobe. The ring current is more enhanced for this storm when the spacecraft is in the north lobe (main phase, SYM-H=-105 nT), than when the spacecraft is in the south lobe (recovery phase, SYM-H=-76 nT). The AE index was 873 nT when the spacecraft was at the north lobe boundary compared to 576 nT at the south lobe boundary. The resulting normalised lobe field is higher in the north lobe than in the south. Due to the small number of events, it is impossible to investigate whether the size of storm or storm phase influence the lobe magnetic field.

	Lobe	Date	Storm phase	AE (nT)	SYM-H (nT)	Storm size (nT)	Norm. lobe field (nT)
1	North	21/08/2002	Main	873	-105	-119	41.47
2	North	02/10/2002	Recovery	644	-78	-154	41.70
3	North	31/08/2004	Recovery	597	-59	-128	41.54
4	North	29/09/2001	Main	440	-50	-50	38.03
5	South	21/08/2002	Recovery	576	-76	-119	35.91
6	South	01/10/2001	Recovery	415	-94	-143	37.87

Table 6.1: A summary of the north and south lobe passes during enhanced ring current conditions when SYM-H \leq -50 nT. Column 2 notes whether the spacecraft was in the north or south lobe. Column 3 notes the date of the event. Column 4 notes the phase of the storm that is occurring when the spacecraft passes through the boundary point. Columns 5 and 6 give the AE and SYM-H values at the time of the pass through the boundary point. Column 7 gives an indication as to the size of the storm in terms of the minimum SYM-H value reached and the final column gives the normalised magnetic field value at the boundary point.

The full dataset shown in Figure 6.7 was then binned in two different ways. The first involved binning the data in terms of equal numbers of data. Figure 6.8 shows the binned data for SYM-H (panel a) and AE (panel b). The numbers above each bar indicate the bin size and the vertical lines indicate the standard error in the mean values. The first bin at negative SYM-H values has the highest mean

lobe field and the lowest mean lobe field is around -10 nT. The mean lobe field increases with increasing AE index (panel b), although there is a reduction in lobe field in the highest AE bin.

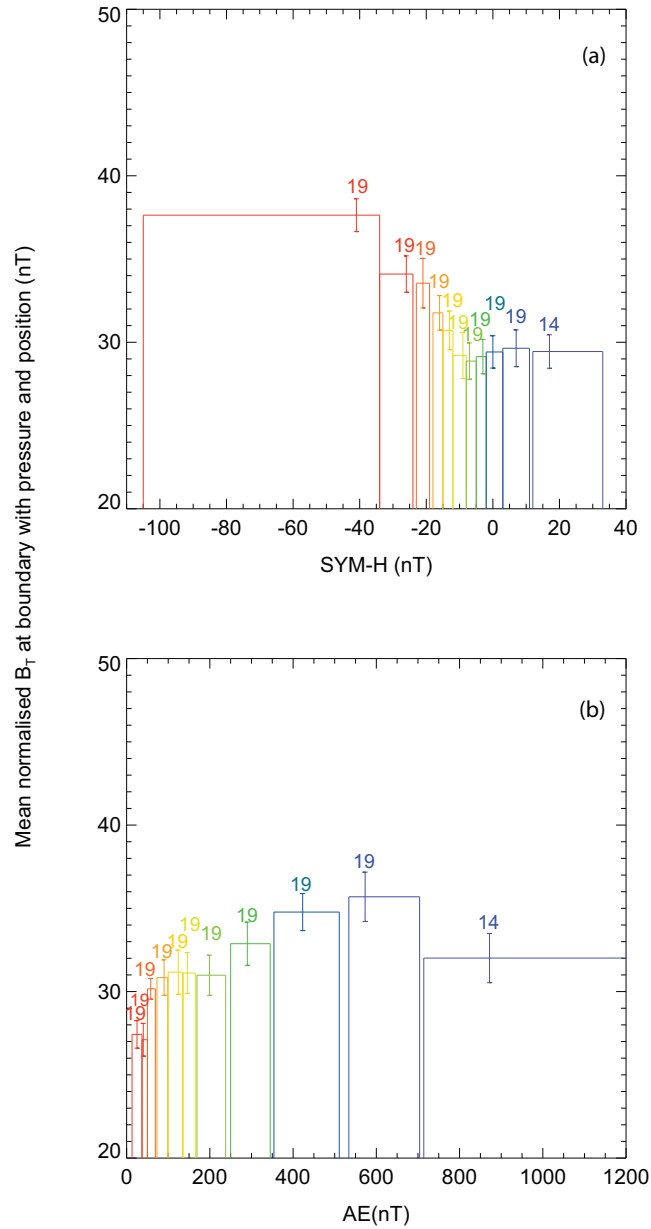


Figure 6.8: Variation of the normalised lobe magnetic field to dynamic pressure and position, with SYM-H (panel a) and AE (panel b). Data are separated into bins of equal number (with the exception of the last bin).

Figure 6.9 arranges the data in equal SYM-H and AE bins, and as such there

are a different number in each bin. Panel (a) of Figure 6.9 shows data binned in SYM-H. The vertical lines again indicate the standard error in the mean and the bin size is shown above each bar. The mean lobe field in the most negative SYM-H bin is highest with the lowest lobe field occurring at positive SYM-H values. The mean lobe field increases with the AE index (panel b) up to 900 nT, although the final bin at higher AE values has a lower mean lobe field.

Although the data in Figure 6.9 show the relationship between the lobe field and the AE and SYM-H indices, they do so separately. In order to combine the information and to compare stormtime substorms to non-stormtime substorms, the data is shown in a different way in Figure 6.10. The data are again binned according to the AE index, but the data are organised into non-storm (SYM-H > -50 nT, red) and storm times (SYM-H ≤ -50 nT, blue). There are no storm events at very low AE values. It should be noted that there is one non-storm (red) data point in the south lobe at about 2600 nT, which has not been included in this figure. Although there are relatively few storm data (in blue), the mean lobe field is larger for these, compared to the non-storm time data in red.

Finally, Figure 6.11 shows the mean normalised lobe field for different levels of geomagnetic activity. The groups have been chosen according to the AE and SYM-H indices at the boundary, in a similar way to the previous studies in Chapters 4 and 5. The data show that when the ring current is enhanced to the level used in the definition of ‘RC’ (SYM-H ≤ -50 nT), the normalised lobe field is larger at the boundary than compared to substorms and quiet times. It should be noted that the number of data points in the ‘RC’ group is lower than in previous figures due to the definition of the group restricting the data to stormtime substorms with AE ≥ 500 nT, and two passes occurred during storm times but at AE values less than 500 nT, and so are not included in the figure. Further analysis showed a statistical difference between the ‘AE’ and ‘RC’ groups to the 95 % level, using the Mann-Whitney-Wilcoxon test [Barlow, 1989].

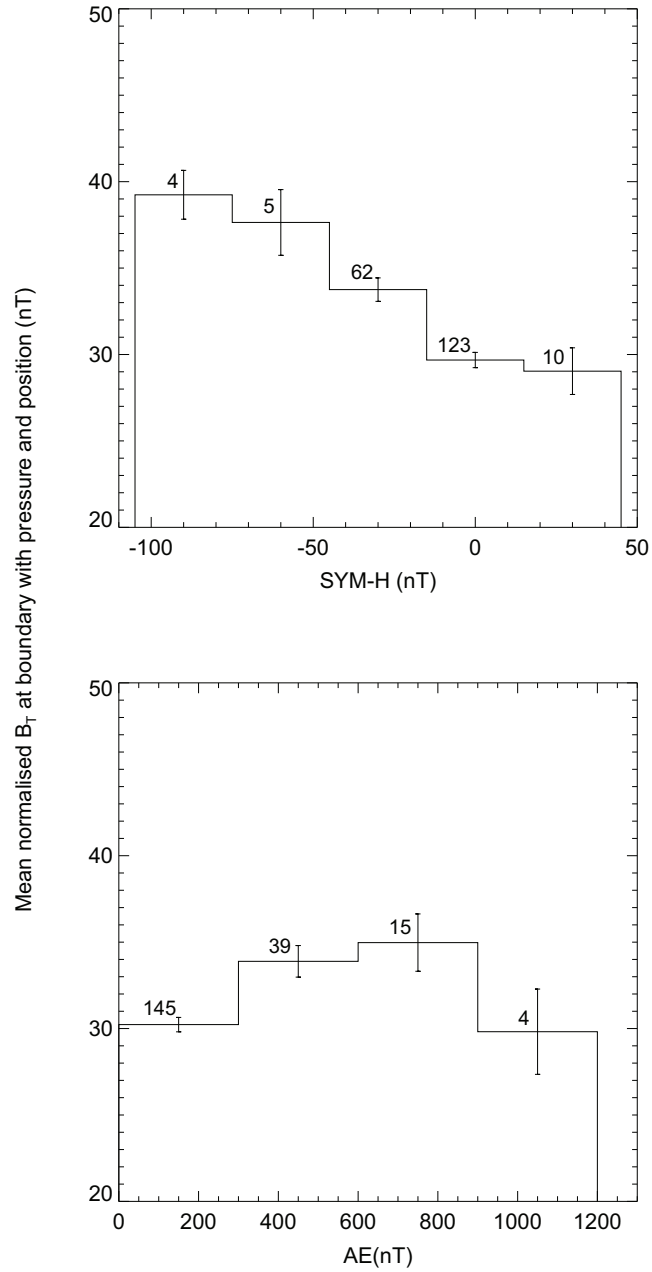


Figure 6.9: Variation of the normalised lobe magnetic field to dynamic pressure and position, with SYM-H (panel a) and AE (panel b). Data are separated into bins of equal SYM-H and AE.

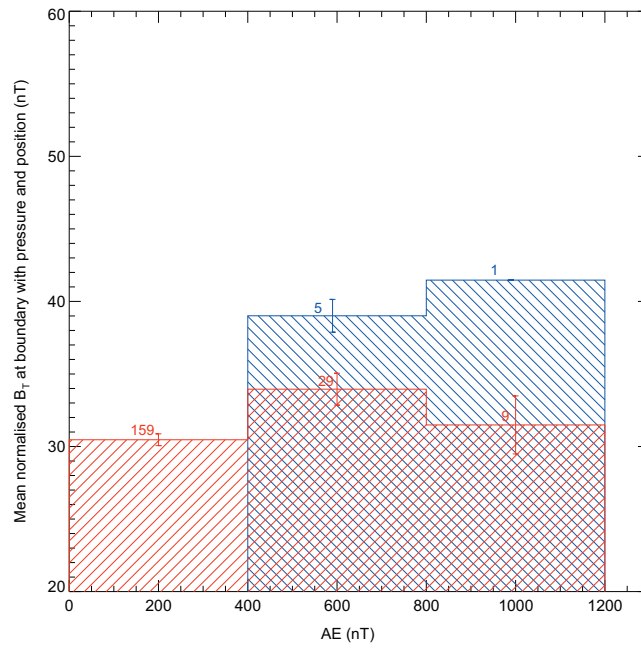


Figure 6.10: Variation of the normalised lobe magnetic field to dynamic pressure and position, with AE. Data are separated into bins of equal AE. Non-storm times are shown in red and storm times are shown in blue.

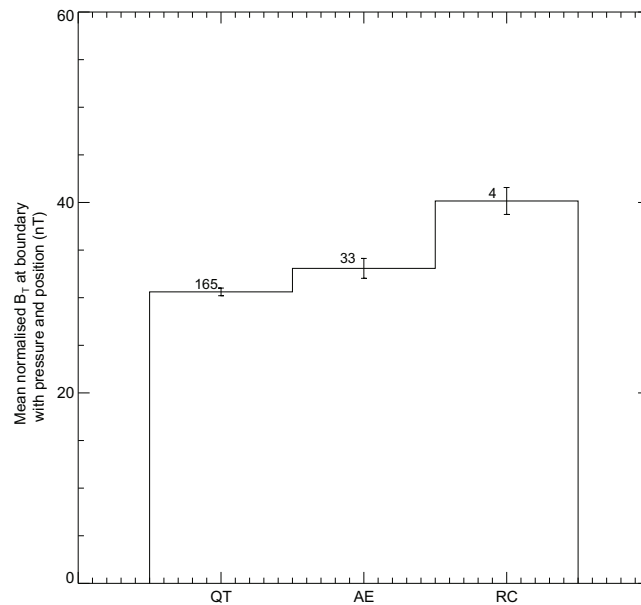


Figure 6.11: Normalised lobe magnetic field to dynamic pressure and position, for different levels of geomagnetic activity. Data are separated into geomagnetic activity groups were QT represent quiet conditions, AE represents substorm conditions and RC represents enhanced ring current and storm conditions. A full explanation is given in the text.

6.5 Discussion

The purpose of the final data study was to investigate the lobe magnetic field under different geomagnetic conditions. Previous research, reviewed in Chapter 2, has found a relationship of lobe magnetic field with substorms and storms, although only with respect to smaller storms [*Nakai et al.*, 1999]. Although *Miyashita et al.* [2005] did study a larger storm in 2003, it was a relatively rare storm, causing a very large deviation in the geomagnetic field, resulting in a Dst level of -400 nT. Lobe magnetic field values measured were 50-200 nT. The results were obtained at $8 R_E$ downtail and were not measured at further distances away from the Earth. *Milan et al.* [2008] proposed that the magnetotail was stabilised to substorm initiation during magnetic storms, and that, although substorms did indeed occur during magnetic storms, the enhanced ring current caused a locally more dipolar geomagnetic field on the tail side of the ring current, reducing the opportunity for reconnection in the tail, and that more open flux was needed in the lobes to cause magnetic reconnection. Although previous researchers have found that the lobe field changes with position downtail and solar wind conditions, no specific studies of the lobe field under different conditions in the mid-tail region have identified what may occur as a result of an enhanced ring current in comparison to quiet and substorm periods.

The first two data studies in Chapters 4 and 5 found evidence of an ‘activation’ of the current sheet during substorms, in terms of its motion and orientation. They also provided some indication of a stabilisation of these parameters during storms, even though substorms were still occurring. Current density estimates were larger during storms than during both substorms alone and quieter times. It was proposed that this may be due to the increased amount of open flux in the tail during storms and the reconnection of open field lines during non-stormtime substorms. This chapter investigated that proposal by studying the magnetic field in the lobes during Cluster’s orbits from 2001-2007.

6.5.1 Data analysis and normalisation

Using the Cluster 3 spacecraft, an investigation of the total magnetic field in both the north and south lobes was undertaken. The data were investigated in terms of position within the tail, solar wind dynamic pressure variations, levels of the auroral electrojets in the ionosphere and the enhancement of the ring current. Because the Cluster spacecraft pass through the magnetotail at different positions at different times, it was important to select an appropriate point at which the lobe field was assessed. The north lobe boundary was defined as the last point that the spacecraft was in the north lobe, prior to entering the plasma sheet for the first crossing of the current sheet during the magnetotail pass. The south lobe boundary was defined in a similar way, as the first point that the spacecraft was in the south lobe, after exiting the plasma sheet. Criteria were used to define the lobes, based on typical values.

The variation of lobe field with position downtail in the X direction in Figure 6.1 is in agreement with previous research, e.g. *Fairfield and Jones* [1996]. The variation of lobe field with solar wind dynamic pressure (Figure 6.4) was also in agreement with previous research discussed in Section 2.5 (e.g. *Fairfield and Jones* [1996]). Data from *Fairfield and Jones* [1996] showed a range of lobe field strength of between around 20-40 nT at about $15 R_E$ downtail, which is a similar range to that in Figure 6.1. In order to remove the variations with solar wind dynamic pressure and position, the data were normalised using data from both lobes, firstly to position, using a least squares non-linear fit and then to pressure using two separate linear fits for low and high pressures. The initial normalisation to position resulted in a variation of lobe field with solar wind dynamic pressure, in Figure 6.4, that increased with increasing pressure, although the slope of the data at lower pressures was steeper than at high pressures. Following both normalisations there was a spread of data with position in the X, Y and Z GSM directions (Figure 6.5).

6.5.2 Influence of substorms and magnetic storms

Figure 6.6 presented an initial analysis of the effect of an enhanced ring current (using SYM-H) and substorm activity (using the AE index) on the lobe field. It was clear that those passes through the lobes during an enhanced ring current were at higher lobe field values than the majority of the other data. The passes at high AE values were spread throughout the panels and no clear trend with AE was evident. These results are in contrast to those by *Nakai et al.* [1999] who found that the lobe field increased with increasing AE values but only at distances more than $9 R_E$ downtail.

The data were then presented in more detail, with distributions of the lobe field, with the SYM-H and AE indices (Figure 6.7). The results confirmed the previous result that the magnetic field for negative SYM-H values of less than about -50 nT, was higher and had less scatter in the data than when $\text{SYM-H} > -50$ nT. The response of the lobe field to the AE index did not show any clear trend.

To enable the data to be displayed more clearly, it was binned in two ways: with equal bin size and then in equal SYM-H and AE bins. Panel (a) of Figure 6.8 shows smaller lobe fields at about -10 nT SYM-H values, with increasing lobe field as SYM-H becomes more negative, indicating a more enhanced ring current and storm conditions. The data in panel (b) showed an increase in lobe field with the AE index, although there is a drop at the highest AE values. Figure 6.9 shows the normalised data according to equal SYM-H (panel (a)) or AE (panel (b)) bin sizes. The trends are similar to the previous figures, with larger lobe field when the ring current is enhanced at the most negative SYM-H values. Data for the AE show increases in the lobe field as AE increases, although at AE values larger than about 1000 nT, the lobe field drops.

The data from Figure 6.9 were re-binned and separated according to storm and non-storm times (using $\text{SYM-H} \leq -50$ nT to define storm times). Although the

number of storm data are few, the data clearly demonstrated larger lobe fields for storm times compared to non-storm times. It also showed that the increase in the lobe field with the AE index seen in earlier plots was probably due to the storm time events at higher AE values.

The final representation of the results was in Figure 6.11, which separated the data into the same geomagnetic groups as used in the first two data studies, using SYM-H and the AE index to define quiet (QT), substorm (AE) and storm (RC) conditions. The results show larger lobe fields for storm conditions compared to quiet and substorm times.

The SYM-H and AE indices identified whether the passes through the lobes were occurring during different geomagnetic conditions and allowed an investigation of whether the lobe field changed according to those parameters. The data certainly indicate that under storm conditions, the boundary lobe total field strength is larger than non-storm times. If storm times are accounted for, there does not seem to be any effect of substorms on the lobe field. The larger lobe field under storm conditions is not surprising following the results from the previous chapter, which found larger current density during storm times. It also found lower current density for substorms and quiet times. This is also in agreement with the smaller mean lobe fields for quiet and substorm conditions in this data study.

The enhanced current density and lobe field during storm times is most likely due to increased amount of open flux following prolonged dayside reconnection. Although some of the storm events occurred during the recovery phase, the results imply that there must still be a large amount of open flux in the tail during recovery, compared to quiet times. The lower values during substorms in terms of current density and lobe field show that the amount of open flux present in the lobes following dayside reconnection is being closed by tail reconnection quickly during the substorm process. The data have not been separated according to substorm phase, although further studies could be performed in the future to assess how

the lobe field changes during the growth, expansion and recovery phases and how stormtime and non-stormtime substorms differ in these factors. Although previous research has found a relationship with the AE index (e.g. *Nakai et al.* [1999]), the effect was only seen at distances further than $9 R_E$ downtail, with the opposite effect with AE (a decrease) closer to the Earth. The data from *Nakai et al.* [1999] did not examine large storms and only included those with a Dst value of greater than -45 nT, so a comparison cannot be made with the current dataset. It is unclear from the previous research, discussed in Chapter 2 whether any changes with the AE index, that were found, were separated in terms of non-storm and storm times.

6.6 Conclusions

This chapter described the work carried out in a third data study, investigating the lobe magnetic field strength. The Cluster 3 spacecraft was used to locate the lobes within passes through the magnetotail and also to assess the magnetic field strength within the lobes. The AE and SYM-H indices were used to define the geomagnetic conditions at the time of each magnetic field measurement and the field. OMNI data were used to assess the solar wind dynamic pressure for each pass through the north and south lobe.

The lobe field strength was found to vary with position downtail and solar wind dynamic pressure in a similar way to previous research. The data were normalised to account for variations with position along the X GSM direction and dynamic pressure. The study also considered the lobe field strength at different levels of geomagnetic activity and found that it is larger during magnetic storms compared to quiet and substorm conditions.

The final chapter summarises the three data studies within this thesis and looks to the future, providing questions that remain unanswered and ideas for further research.

Chapter 7

Summary and future work

7.1 Introduction

This thesis describes three statistical studies of the magnetotail, using both ground- and space-based instrumentation. Chapter 1 gave a summary of some of the relevant points in solar terrestrial physics followed by Chapter 2 which discussed previous research relating to the magnetotail, specifically the cross-tail current sheet and lobes. The instrumentation and analysis techniques used in the thesis work were described in Chapter 3. The main instrumentation used in the studies was ESA's Cluster mission, which has enabled a study of the dynamics of the cross-tail current sheet (Chapter 4), as well an investigation of its orientation, current density and thickness (Chapter 5), using multi-spacecraft techniques. The final study (Chapter 6) of the magnetotail lobes, provided a more complete picture of the region. This chapter summarises and provides the main conclusions from the three science studies. It then follows with a discussion of potential extensions to the work.

7.2 Thesis summary

The first data study described in Chapter 4 involved searching for current sheet crossings made by the Cluster 3 spacecraft. The number of crossings in each orbit through the magnetotail was assessed at distances more than $8 R_E$ downtail and within $10 R_E$ in either Y GSM direction. The data were analysed in two ways, firstly comparing the number of crossings per orbit under different levels of geomagnetic activity, which was assessed using the AE and SYM-H indices. Throughout the thesis the AE index was used as a measure of substorm activity and the SYM-H index was used as an indication that the ring current was enhanced and that a magnetic storm was occurring. Secondly the data were normalised to the amount of time spent in the region under study, to take account of differences in orbital path from 2001-2007.

The analyses showed that there was more motion of the current sheet during substorms, compared to both quiet and storm times. The mean standard deviation of the AE index was about 110 nT for an active current sheet, compared to about 20 nT for an inactive current sheet, indicating more substorm activity in an active current sheet. The data were also separated according to geomagnetic conditions. Results indicated that there was a larger mean number of crossings for the substorm group (0.93 normalised crossings) than for the quiet times group (0.28) and the storm group (0.75). Although substorms were still occurring during the storm time orbits, there was evidence of less motion when the ring current was enhanced. The reasons for the apparent stabilisation of the current sheet motion during storms was not clear. *Milan et al.* [2008] and *Nakai and Kamide* [2003] proposed a stabilisation of the tail to substorm initiation due to the increased amount of open flux during storms and the results from the first study also implied a stabilisation, but of the current sheet motion, which may be due to the same reasons. Previous research had been unclear as to the dependence of current sheet motion on substorms and for the first time a comparison was made of three different geomagnetic conditions

in this way.

The results from the first study led to an investigation of current sheet structure, to analyse whether the orientation, current density and thickness were also affected by different levels of geomagnetic activity (Chapter 5). The current sheet crossings database from the first study was used to examine each crossing individually. All four Cluster spacecraft were used to examine the structure of the current sheet using MVA and Curlometer techniques. Again the AE and SYM-H indices were employed as measures of substorm and storm conditions, respectively.

The results demonstrated a larger mean tilt angle (in the YZ plane) during substorms ($\sim 28^\circ$) than at quiet times ($\sim 17^\circ$). In contrast, during storm times, the tilt angle was significantly reduced compared to the substorm group, with a mean of about 14° . It was concluded that the tail rigidity alluded to in the previous study, during magnetic storms, suppresses the motion of the current sheet, and also in turn suppresses the tilt angle. The larger tilt of the current sheet during substorms is also related to the previous study that found more motion during substorms, implying larger tilt angles during current sheet motion. This is in agreement with previous studies that found a highly tilted current sheet during flapping motion. The effect of magnetic storms on the tilt angle had not been previously investigated, in particular in relation to substorms and quiet times.

The current density also varied depending on geomagnetic activity, with larger current densities found during magnetic storms ($\sim 7.5 \text{ nA m}^{-2}$), compared to quiet ($\sim 7 \text{ nA m}^{-2}$) and substorm times ($\sim 5.5 \text{ nA m}^{-2}$). The values of tilt angle, current density and half thickness were all in agreement with previous researchers, although the direct comparison of geomagnetic activity on these parameters had not been previously carried out. It was concluded that the larger current density during magnetic storms implied a larger lobe field, although this was not investigated at this stage.

The final study, concerning the magnetic field of the magnetotail lobes was initially propounded following the results of the previous investigations. The rigidity in the tail proposed as a result of the first two studies and the stabilisation of the tail found by *Milan et al.* [2008] implied larger lobe field during magnetic storms than compared to substorms alone. A large lobe field during storms is to be expected as a result of the storm process involving prolonged dayside reconnection, providing the increased amount of open flux. The lobe field should therefore be larger during storms than quiet times. However, a comparison of substorm, storm and quiet times at various points in the magnetotail had not been previously investigated.

Each part orbit through the magnetotail from the first study was used to provide a starting point for this study. The lobes either side of the plasma sheet were located using particle data and typical number density and temperature parameters of the lobe. The central boundary positions at the inner edges of the lobes were estimated for each orbit through the magnetotail. The IMF conditions at the time of the measurements were assessed using solar wind dynamic pressure data, lagged to the boundary positions. The total magnetic field was found to vary with both position downtail and solar wind dynamic pressure in agreement with previous research. The data were then normalised to both position downtail in the X GSM direction and dynamic pressure, and separated according to AE and SYM-H values, into the same three geomagnetic condition groups as previously used.

The results indicated larger lobe field strength during magnetic storms (40.16 nT) compared to substorms and quiet times. The lobe field during substorms (33.08 nT) was similar to that at quiet times (30.61 nT). The proposals from the previous two studies that the lobe strength was increased during storms was borne out in the results of the final study.

In summary, the three science studies described in this thesis provide a picture of the magnetotail's response to an enhanced ring current and substorms and how these compare to quiet times. The main results are summarised in Table 7.1 with

the highest number of stars indicating which geomagnetic group had the largest results for each current sheet or lobe parameter. The data analyses imply that either substorms or the processes that cause substorms result in current sheet motion and also a highly tilted current sheet. In contrast, even though substorms are still occurring during magnetic storms, the enhanced ring current and increased amount of open flux in the lobes, cause a rigidity to the tail, suppressing current sheet motion and tilt and increasing the current density within the current sheet. Although some questions regarding the magnetotail and geomagnetic activity have been answered, more remain. As such, the work could be taken forward in various ways, and this is discussed in the following section.

Geomagnetic condition	Current sheet motion	Current sheet tilt angle	Current sheet current density	Lobe field
Quiet	*	**	**	**
Substorms	***	***	*	*
Storms	**	*	***	***

Table 7.1: A summary of the main results from the thesis. *** indicates the largest value in each column and * indicates the smallest value in each column.

7.3 Future work

The work presented in this thesis could be taken further in two main stages. The first stage would be an extension of the dataset. One of the main difficulties with this work has been the low number of magnetic storms occurring at the times the spacecraft is located in the region under study. An extension of the dataset could therefore increase the number of storm events. The extension could arise from three areas: Cluster's later tail seasons, the THEMIS spacecraft and the GEOTAIL spacecraft.

Firstly, Cluster tail seasons after 2007 could be employed to increase the dataset. Although the orbit in the later years has altered from passing the current sheet in the mid-tail region, further investigation of the lobe field could be possible. The use of THEMIS data would also extend the dataset after 2007 as this was the year of its launch. Its tail seasons were between December and April of 2007/2008 and 2008/2009, with the five spacecraft at times, aligned along the tail in conjunction, down to about $-30 R_E$ in the X direction [Frey *et al.*, 2008]. The THEMIS spacecraft are not in the same orbit as Cluster, and as such do not pass from the north lobe, through the current sheet and into the south lobe, making a direct extension to the first study unlikely. However, they may be able to provide lobe field data and can certainly observe current sheet motion, enabling extensions to the second and third studies. They have already been used in previous research to study the current sheet (e.g. Runov *et al.* [2009]).

The final extension to the research would involve the GEOTAIL spacecraft which has already been employed by Sergeev *et al.* [2006] in a current sheet investigation. Again, the orbit is unlike Cluster, and its path is near the solar-ecliptic plane at small Z values. It was launched in 1992 and its apogee was at about $-200 R_E$ in the X direction in the first few years of the mission, reducing in the second phase to about $-30 R_E$, enabling an extension both in terms of years of study and of position downtail [Nishida *et al.*, 1992]. GEOTAIL data could be used in both the second and third studies on the current sheet structure and lobe field. Although multi-spacecraft techniques would not be possible, estimates of the current density from the lobe field is possible using single spacecraft. Not only would the use of these three datasets increase the number of events studied, they would allow a comparison of current sheet and lobe parameters with geomagnetic conditions during solar maximum and the recent extended solar minimum.

The second stage of further work is a series of studies to investigate the lobes and current sheet in more detail. The first of these potential studies is a case study

of a storm event which occurs when Cluster is in the north lobe, and continues as the spacecraft move into the current sheet and south lobe. This would allow an analysis of the magnetotail through the process of a magnetic storm.

Secondly, the effect of substorm phase and storm phase is a necessary follow-up to the work. It might be the case that the response of the tail, in terms of current sheet motion, current sheet structure and lobe field may be different depending on the phase of the event, even with similar AE or SYM-H values. This could certainly be investigated in terms of substorm phase with the current dataset, although the numbers of storm events are too few. However, an extension of the dataset may enable the storm phase to also be investigated. The substorm phase could be investigated specifically to see whether the lower current densities found compared to those during storm times are affected by the phase of the substorm. The current density may be significantly enhanced during the growth phase of the substorm, followed by a recovery as the open flux is closed by tail reconnection and the averaging of data in the final study would not have shown this detail. It would be interesting to compare stormtime and non-stormtime substorms in terms of the substorm phase.

A further important analysis would be of the different structures alluded to by *Runov et al.* [2006]. It would be interesting to ascertain the frequency of occurrence of the bifurcated, centred and asymmetric current sheets in the present dataset and compare their occurrence with geomagnetic conditions at the times of the current sheet crossings. Although the tilt of the current sheet in the YZ plane has been studied as part of this thesis work, the investigation could be expanded to include an analysis of the hinge angle in the XZ plane. *Petrukovich et al.* [2005] found hinge angles up to 20° but a study of geomagnetic conditions was not made.

In addition, the present studies did not discriminate according to duration of crossings whereas previous research has either focused on fast crossings (e.g. *Sergeev et al.* [2006] and *Runov et al.* [2006]) or slower crossings (e.g. *Petrukovich*

et al. [2005]). A further study could separate out fast and slow crossings and investigate any differences between the two types in terms of geomagnetic conditions and current sheet and lobe parameters.

Further work should also include an investigation of the solar wind effect on current sheet motion and structure. *Forsyth et al.* [2009] observed current sheet motion following a solar wind pressure pulse, but as yet this has not been studied statistically. The present analysis could be extended to see what effect solar wind dynamic pressure has on current sheet motion and current sheet structure.

Finally, a superposed epoch analysis of lobe field according to geomagnetic conditions would be a natural progression to the third data study in particular. This would provide an extension to the boundary lobe field data used in the current work, to the lobe field throughout the orbits in both lobes.

Although the Earth's magnetosphere has been investigated extensively, there are always more questions that remain, as the solar-terrestrial relations are complex in nature. The cross-tail current sheet and lobes are important regions in these processes and more work is needed to understand their behaviour fully.

Bibliography

- Akasofu, S.-I. (1964), The development of the auroral substorm, *Planet. Sp. Sci.*, *12*, 273, doi:10.1016/0032-0633(64)90151-5.
- Akasofu, S.-I. (1981), Relationships between the AE and Dst indices during geomagnetic storms, *J. Geophys. Res.*, *86*, 4820–4822, doi:10.1029/JA086iA06p04820.
- Balogh, A., C. M. Carr, M. H. Acuña, M. W. Dunlop, T. J. Beek, P. Brown, K. Fornaçon, E. Georgescu, K. Glassmeier, J. Harris, G. Musmann, T. Oddy, and K. Schwingenschuh (2001), The Cluster Magnetic Field Investigation: overview of in-flight performance and initial results, *Ann. Geophys.*, *19*, 1207–1217, doi:10.5194/angeo-19-1207-2001.
- Barlow, R. J. (1989), *Statistics: A Guide to the Use of Statistical Methods in the Physical Sciences (Manchester Physics Series)*, reprint ed., WileyBlackwell.
- Bauer, T. M., W. Baumjohann, and R. A. Treumann (1995), Neutral sheet oscillations at substorm onset, *J. Geophys. Res.*, *100*, 23,737–23,742, doi:10.1029/95JA02448.
- Baumjohann, W., and R. A. Treumann (1996), *Basic space plasma physics*, edited by Baumjohann, W. & Treumann, R. A., London: Imperial College Press.
- Behannon, K. W. (1968), Mapping of Earth's Bow Shock and Magnetic Tail by Explorer 33, *J. Geophys. Res.*, *73*, 907, doi:10.1029/JA073i003p00907.

- Caan, M. N., R. L. McPherron, and C. T. Russell (1975), Substorm and interplanetary magnetic field effects on the geomagnetic tail lobes, *J. Geophys. Res.*, *80*, 191–194, doi:10.1029/JA080i001p00191.
- Chapman, S., and V. C. A. Ferraro (1930), A New Theory of Magnetic Storms, *Nature*, *126*, 129–130, doi:10.1038/126129a0.
- Coroniti, F. V., and C. F. Kennel (1972), Changes in magnetospheric configuration during the substorm growth phase., *J. Geophys. Res.*, *77*, 3361–3370, doi:10.1029/JA077i019p03361.
- Dandouras, I., A. Barthe, E. Penou, S. Brunato, H. Rème, L. M. Kistler, M. B. Bavassano-Cattaneo, and A. Blagau (2010), Cluster Ion Spectrometry (CIS) Data in the Cluster Active Archive (CAA), in *The Cluster Active Archive, Studying the Earth's Space Plasma Environment*, edited by Laakso, H., Taylor, M., & Escoubet, C. P., pp. 51–72, Springer, Netherlands.
- Dandouras, I., A. Barthe, K. L., and A. Blagau (2011), Calibration report of the CIS measurements in the Cluster Active Archive (CAA), *Tech. Rep. CAA-EST-CR-CIS (1.2)*, European Space Agency. Cluster Active Archive.
- Davey, E. A., M. Lester, S. E. Milan, and R. C. Fear (2012), Storm and substorm effects on magnetotail current sheet motion, *J. Geophys. Res.*, *117*, A02202, doi:10.1029/2011JA017112.
- Davis, T. N., and M. Sugiura (1966), Auroral Electrojet Activity Index AE and Its Universal Time Variations, *J. Geophys. Res.*, *71*, 785–801.
- Dungey, J. W. (1961), Interplanetary Magnetic Field and the Auroral Zones, *Physical Review Letters*, *6*, 47–48, doi:10.1103/PhysRevLett.6.47.
- Dungey, J. W. (1965), The Length of the Magnetospheric Tail, *J. Geophys. Res.*, *70*, 1753–1753, doi:10.1029/JZ070i007p01753.

- Dungey, J. W. (1966), The Magnetosphere, Inaugural Lecture 3 May 1966, Imperial College of Science and Technology, University of London.
- Dunlop, M. W., and J. P. Eastwood (2008), The Curlometer and Other Gradient Based Methods, *ISSI Scientific Reports Series*, 8, 17–26.
- Dunlop, M. W., and T. I. Woodward (2000), Cluster Magnetic Field Analysis Techniques, in *Cluster-II Workshop Multiscale / Multipoint Plasma Measurements*, *ESA Special Publication*, vol. 449, edited by R. A. Harris, p. 351.
- Dunlop, M. W., D. J. Southwood, K.-H. Glassmeier, and F. M. Neubauer (1988), Analysis of multipoint magnetometer data, *Adv. Space Res.*, 8, 273–277, doi:10.1016/0273-1177(88)90141-X.
- Dunlop, M. W., A. Balogh, K.-H. Glassmeier, and P. Robert (2002), Four-point Cluster application of magnetic field analysis tools: The Curlometer, *J. Geophys. Res.*, 107, 1384, doi:10.1029/2001JA005088.
- Escoubet, C. P., M. Fehringer, and M. Goldstein (2001), The Cluster Mission, *Ann. Geophys.*, 19, 1197–1200.
- Fairfield, D. H. (1987), *Structure of the geomagnetic tail in Magnetotail Physics*, pp. 23–33, edited by Lui, A. T. Y. and Akasofu, S.-I., Baltimore, MD, Johns Hopkins University Press.
- Fairfield, D. H., and J. Jones (1996), Variability of the tail lobe field strength, *J. Geophys. Res.*, 101, 7785–7792, doi:10.1029/95JA03713.
- Fairfield, D. H., and N. F. Ness (1970), Configuration of the geomagnetic tail during substorms., *J. Geophys. Res.*, 75, 7032–7047, doi:10.1029/JA075i034p07032.
- Forsyth, C., M. Lester, R. C. Fear, E. Lucek, I. Dandouras, A. N. Fazakerley, H. Singer, and T. K. Yeoman (2009), Solar wind and substorm excitation of the wavy current sheet, *Ann. Geophys.*, 27, 2457–2474, doi:10.5194/angeo-27-2457-2009.

- Forsyth, C., M. Lester, A. N. Fazakerley, C. J. Owen, and A. P. Walsh (2011), On the effect of line current width and relative position on the multi-spacecraft curlometer technique, *Planet. Space Sci.*, *59*, 598–605, doi:10.1016/j.pss.2009.12.007.
- Frey, S., V. Angelopoulos, M. Bester, J. Bonnell, T. Phan, and D. Rummel (2008), Orbit Design for the THEMIS Mission, *Space Sci. Rev.*, *141*, 61–89, doi:10.1007/s11214-008-9441-1.
- Gloag, J. M., E. A. Lucek, L. Alconcel, A. Balogh, P. Brown, C. M. Carr, C. N. Dunford, T. Oddy, and J. Soucek (2010), FGM Data Products in the CAA, in *The Cluster Active Archive, Studying the Earth's Space Plasma Environment*, edited by Laakso, H., Taylor, M., & Escoubet, C. P., pp. 109–128, Springer, Netherlands.
- Gonzalez, W. D., J. A. Joselyn, Y. Kamide, H. W. Kroehl, G. Rostoker, B. T. Tsurutani, and V. M. Vasyliunas (1994), What is a geomagnetic storm?, *J. Geophys. Res.*, *99*, 5771–5792, doi:10.1029/93JA02867.
- Gopalswamy, N., S. Nunes, S. Yashiro, and R. A. Howard (2004), Variability of solar eruptions during cycle 23, *Adv. Space Res.*, *34*, 391–396, doi:10.1016/j.asr.2003.10.054.
- Greco, A., A. L. Taktakishvili, G. Zimbardo, P. Veltri, and L. M. Zelenyi (2002), Ion dynamics in the near-Earth magnetotail: Magnetic turbulence versus normal component of the average magnetic field, *J. Geophys. Res.*, *107*, 1267, doi:10.1029/2002JA009270.
- Hargreaves, J. K. (1995), *The Solar-Terrestrial Environment*, 434 pp., Cambridge, UK: Cambridge University Press.
- Intriligator, D. S., H. R. Collard, J. D. Mihalov, J. H. Wolfe, and O. L. Vaisberg

- (1979), Evidence for earth magnetospheric tail associated phenomena at 3100 R sub E, *Geophys. Res. Lett.*, *6*, 585–588, doi:10.1029/GL006i007p00585.
- Iyemori, T. (1990), Storm-time magnetospheric currents inferred from mid-latitude geomagnetic field variations, *J. Geomagn. Geoelectr.*, *42*, 1249–1265.
- Iyemori, T., and D. R. K. Rao (1996), Decay of the Dst field of geomagnetic disturbance after substorm onset and its implication to storm-substorm relation, *Ann. Geophys.*, *14*, 608–618, doi:10.1007/s00585-996-0608-3.
- Kivelson, M. G., and C. T. Russell (1995), *Introduction to Space Physics*, Cambridge, UK: Cambridge University Press.
- Laakso, H., C. Perry, S. McCaffrey, D. Herment, A. J. Allen, C. C. Harvey, C. P. Escoubet, C. Gruenberger, M. G. G. T. Taylor, and R. Turner (2010), Cluster Active Archive: Overview, in *The Cluster Active Archive, Studying the Earth's Space Plasma Environment*, edited by Laakso, H., Taylor, M., & Escoubet, C. P., pp. 3–37, Springer, Netherlands.
- Li, L. Y., J. B. Cao, G. C. Zhou, T. L. Zhang, D. Zhang, I. Dandouras, H. Rème, and C. M. Carr (2011), Multiple responses of magnetotail to the enhancement and fluctuation of solar wind dynamic pressure and the southward turning of interplanetary magnetic field, *J. Geophys. Res.*, *116*, A12223, doi:10.1029/2011JA016816.
- Lui, A. T. Y., C. Meng, and S. Akasofu (1978), Wavy nature of the magnetotail neutral sheet, *Geophys. Res. Lett.*, *5*, 279–282, doi:10.1029/GL005i004p00279.
- Maeszawa, K., and T. Hori (1998), The Distant Magnetotail: Its Structure, IMF Dependence, and Thermal Properties, in *New Perspectives on the Earth's Magnetotail*, edited by A. Nishida, D. N. Baker, and S. W. H. Cowley, p. 1.
- Maltsev, Y. P. (2004), Points of controversy in the study of magnetic storms, *Space Sci. Rev.*, *110*, 227–277, doi:10.1023/B:SPAC.0000023410.77752.30.

- Mayaud, P. N. (1980), Derivation, meaning, and use of geomagnetic indices., *Geophys. Monogr. Ser.*, *22*, doi:10.1029/GM022.
- Mihalov, J. D., and C. P. Sonett (1968), The Cislunar Geomagnetic Tail Gradient in 1967, *J. Geophys. Res.*, *73*, 6837–6841, doi:10.1029/JA073i021p06837.
- Milan, S. E. (2009), Both solar wind-magnetosphere coupling and ring current intensity control of the size of the auroral oval, *Geophys. Res. Lett.*, *36*, L18101, doi:10.1029/2009GL039997.
- Milan, S. E., M. Lester, S. W. H. Cowley, K. Oksavik, M. Brittnacher, R. A. Greenwald, G. Sofko, and J.-P. Villain (2003), Variations in the polar cap area during two substorm cycles, *Ann. Geophys.*, *21*, 1121–1140, doi:10.5194/angeo-21-1121-2003.
- Milan, S. E., S. W. H. Cowley, M. Lester, D. M. Wright, J. A. Slavin, M. Fillingim, C. W. Carlson, and H. J. Singer (2004), Response of the magnetotail to changes in the open flux content of the magnetosphere, *J. Geophys. Res.*, *109*, A04220, doi:10.1029/2003JA010350.
- Milan, S. E., J. A. Wild, B. Hubert, C. M. Carr, E. A. Lucek, J. M. Bosqued, J. F. Watermann, and J. A. Slavin (2006), Flux closure during a substorm observed by Cluster, Double Star, IMAGE FUV, SuperDARN, and Greenland magnetometers, *Ann. Geophys.*, *24*, 751–767, doi:10.5194/angeo-24-751-2006.
- Milan, S. E., P. D. Boakes, and B. Hubert (2008), Response of the expanding/contracting polar cap to weak and strong solar wind driving: Implications for substorm onset, *J. Geophys. Res.*, *113*, 9215–+, doi:10.1029/2008JA013340.
- Miyashita, Y., Y. Miyoshi, Y. Matsumoto, A. Ieda, Y. Kamide, M. Nosé, S. Machida, H. Hayakawa, R. W. McEntire, S. P. Christon, D. S. Evans, and O. A. Troshichev (2005), Geotail observations of signatures in the near-Earth

- magnetotail for the extremely intense substorms of the 30 October 2003 storm, *J. Geophys. Res.*, *110*, A09S25, doi:10.1029/2005JA011070.
- Miyashita, Y., Y. Kamide, Y. Miyoshi, S. Machida, K. Liou, T. Mukai, Y. Saito, C.-I. Meng, and G. K. Parks (2006), Magnetotail variations associated with substorm expansion onsets for storm time and nonstorm time, *Geophys. Res. Lett.*, *33*, L24101, doi:10.1029/2006GL028142.
- Nakagawa, T., and A. Nishida (1989), Southward magnetic field in the neutral sheet produced by wavy motions propagating in the dawn-dusk direction, *Geophys. Res. Lett.*, *16*, 1265–1268, doi:10.1029/GL016i011p01265.
- Nakai, H., and Y. Kamide (2003), Substorm-associated large-scale magnetic field changes in the magnetotail: a prerequisite for magnetotail deflation events, *Ann. Geophys.*, *21*, 869–879, doi:10.5194/angeo-21-869-2003.
- Nakai, H., Y. Kamide, and C. T. Russell (1991), Influences of solar wind parameters and geomagnetic activity on the tail lobe magnetic field - A statistical study, *J. Geophys. Res.*, *96*, 5511–5523, doi:10.1029/90JA02361.
- Nakai, H., Y. Kamide, and C. T. Russell (1999), Dependence of the near-Earth magnetotail magnetic field on storm and substorm activities, *J. Geophys. Res.*, *104*, 22,701–22,712, doi:10.1029/1999JA900273.
- Nakamura, R., and S. Kokubun (2000), Tail Configuration During Storms, *Adv. Space Res.*, *25*, 1631–1638, doi:10.1016/S0273-1177(99)00677-8.
- Nakamura, R., W. Baumjohann, Y. Asano, A. Runov, A. Balogh, C. J. Owen, A. N. Fazakerley, M. Fujimoto, B. Klecker, and H. Rème (2006), Dynamics of thin current sheets associated with magnetotail reconnection, *J. Geophys. Res.*, *111*, A11206, doi:10.1029/2006JA011706.
- Ness, N. F. (1987), *Magnetotail research - The early years*, in *Magnetotail Physics*,

11-16 pp., edited by Lui, A. T. Y. and Akasofu, S.-I., Johns Hopkins University Press, Baltimore, MD.

Ness, N. F., C. S. Scearce, and S. C. Cantarano (1967), Probable Observations of the Geomagnetic Tail at 10^3 Earth Radii by Pioneer 7, *J. Geophys. Res.*, *72*, 3769, doi:10.1029/JZ072i015p03769.

Nishida, A., K. Uesugi, I. Nakatani, T. Mukai, D. H. Fairfield, and M. H. Acuna (1992), Geotail mission to explore earth's magnetotail, *EOS Transactions*, *73*, 425, doi:10.1029/91EO00314.

Oberc, P. (1983), The viscous-like magnetospheric convection and the length of the earth's magnetotail, *Planet. Space Sci.*, *31*, 885–888, doi:10.1016/0032-0633(83)90143-5.

Perry, C., T. Eriksson, P. Escoubet, S. Esson, H. Laakso, S. McCaffrey, T. Sanderson, H. Bowen, A. Allen, and C. Harvey (2006), The ESA Cluster Active Archive, in *Cluster and Double Star Symposium, ESA Special Publication*, vol. 598.

Petrukovich, A. A., W. Baumjohann, R. Nakamura, A. Runov, and A. Balogh (2005), Cluster vision of the magnetotail current sheet on a macroscale, *J. Geophys. Res.*, *110*, A06,204, doi:10.1029/2004JA010825.

Petrukovich, A. A., W. Baumjohann, R. Nakamura, A. Runov, A. Balogh, and H. Rème (2007), Thinning and stretching of the plasma sheet, *J. Geophys. Res.*, *112*, A10213, doi:10.1029/2007JA012349.

Pollock, C. J., P. C:Son-Brandt, J. L. Burch, M. G. Henderson, J.-M. Jahn, D. J. McComas, S. B. Mende, D. G. Mitchell, G. D. Reeves, E. E. Scime, R. M. Skoug, M. Thomsen, and P. Valek (2003), The Role and Contributions of Energetic Neutral Atom (ENA) Imaging in Magnetospheric Substorm Research, *Space Sci. Rev.*, *109*, 155–182, doi:10.1023/B:SPAC.0000007518.93331.d5.

Prölss, G. W., and M. K. Bird (2004), *Physics of the Earth's Space Environment: an introduction*, translated by Dr Michael Keith Bird, Springer-Verlag Berlin Heidelberg.

Rème, H., C. Aoustin, J. M. Bosqued, I. Dandouras, B. Lavraud, J. A. Sauvaud, A. Barthe, J. Bouyssou, T. Camus, O. Coeur-Joly, A. Cros, J. Cuvilo, F. Ducay, Y. Garbarowitz, J. L. Medale, E. Penou, H. Perrier, D. Romefort, J. Rouzaud, C. Vallat, D. Alcaydé, C. Jacquy, C. Mazelle, C. D'Uston, E. Möbius, L. M. Kistler, K. Crocker, M. Granoff, C. Mouikis, M. Popecki, M. Vosbury, B. Klecker, D. Hovestadt, H. Kucharek, E. Kuenneth, G. Paschmann, M. Scholer, N. Sckopke, E. Seidenschwang, C. W. Carlson, D. W. Curtis, C. Ingraham, R. P. Lin, J. P. McFadden, G. K. Parks, T. Phan, V. Formisano, E. Amata, M. B. Bavassano-Cattaneo, P. Baldetti, R. Bruno, G. Chionchio, A. di Lellis, M. F. Marcucci, G. Pallochia, A. Korth, P. W. Daly, B. Graeve, H. Rosenbauer, V. Vasyliunas, M. McCarthy, M. Wilber, L. Eliasson, R. Lundin, S. Olsen, E. G. Shelley, S. Fuselier, A. G. Ghielmetti, W. Lennartsson, C. P. Escoubet, H. Balsiger, R. Friedel, J. Cao, R. A. Kovrazhkin, I. Papamastorakis, R. Pellat, J. Scudder, and B. Sonnerup (2001), First multispacecraft ion measurements in and near the Earth's magnetosphere with the identical Cluster ion spectrometry (CIS) experiment, *Ann. Geophys.*, *19*, 1303–1354, doi:10.5194/angeo-19-1303-2001.

Robert, P., M. W. Dunlop, A. Roux, and G. Chanteur (1998), Accuracy of Current Density Determination, *ISSI Scientific Reports Series*, *1*, 395–418.

Rong, Z., C. Shen, E. Lucek, A. Balogh, and L. Yao (2010), Statistical survey on the magnetic field in magnetotail current sheets: Cluster observations, *Chin. Sci. Bull.*, *55*(23), 2542–2547, doi:10.1007/s11434-010-3096-5.

Rong, Z. J., W. X. Wan, C. Shen, X. Li, M. W. Dunlop, A. A. Petrukovich, T. L. Zhang, and E. Lucek (2011), Statistical survey on the magnetic struc-

- ture in magnetotail current sheets, *J. Geophys. Res.*, *116*, A09218, doi:10.1029/2011JA016489.
- Runov, A., R. Nakamura, W. Baumjohann, T. L. Zhang, M. Volwerk, H. Eichelberger, and A. Balogh (2003), Cluster observation of a bifurcated current sheet, *Geophys. Res. Lett.*, *30*(2), 1036–1039, doi:10.1029/2002GL016136.
- Runov, A., V. A. Sergeev, W. Baumjohann, R. Nakamura, S. Apatenkov, Y. Asano, M. Volwerk, Z. Vörös, T. L. Zhang, A. Petrukovich, A. Balogh, J. Sauvaud, B. Klecker, and H. Rème (2005a), Electric current and magnetic field geometry in flapping magnetotail current sheets, *Ann. Geophys.*, *23*, 1391–1403, doi:10.5194/angeo-23-1391-2005.
- Runov, A., V. A. Sergeev, R. Nakamura, W. Baumjohann, T. L. Zhang, Y. Asano, M. Volwerk, Z. Vörös, A. Balogh, and H. Rème (2005b), Reconstruction of the magnetotail current sheet structure using multi-point Cluster measurements, *Planet. Space Sci.*, *53*, 237–243, doi:10.1016/j.pss.2004.09.049.
- Runov, A., V. A. Sergeev, R. Nakamura, W. Baumjohann, S. Apatenkov, Y. Asano, T. Takada, M. Volwerk, Z. Vörös, T. L. Zhang, J. Sauvaud, H. Rème, and A. Balogh (2006), Local structure of the magnetotail current sheet: 2001 Cluster observations, *Ann. Geophys.*, *24*, 247–262, doi:10.5194/angeo-24-247-2006.
- Runov, A., V. Angelopoulos, V. A. Sergeev, K. Glassmeier, U. Auster, J. McFadden, D. Larson, and I. Mann (2009), Global properties of magnetotail current sheet flapping: THEMIS perspectives, *Ann. Geophys.*, *27*, 319–328, doi:10.5194/angeo-27-319-2009.
- Russell, C. T., X. W. Zhou, P. J. Chi, H. Kawano, T. E. Moore, W. K. Peterson, J. B. Cladis, and H. J. Singer (1999), Sudden compression of the outer magnetosphere associated with an ionospheric mass ejection, *Geophys. Res. Lett.*, *26*, 2343–2346, doi:10.1029/1999GL900455.

- Schödel, R., K. Dierschke, W. Baumjohann, R. Nakamura, and T. Mukai (2002), The storm time central plasma sheet, *Ann. Geophys.*, *20*, 1737–1741, doi:10.5194/angeo-20-1737-2002.
- Sergeev, V., V. Angelopoulos, C. Carlson, and P. Sutcliffe (1998), Current sheet measurements within a flapping plasma sheet, *J. Geophys. Res.*, *103*, 9177–9188, doi:10.1029/97JA02093.
- Sergeev, V., A. Runov, W. Baumjohann, R. Nakamura, T. L. Zhang, M. Volwerk, A. Balogh, H. Rème, J. A. Sauvaud, M. André, and B. Klecker (2003), Current sheet flapping motion and structure observed by Cluster, *Geophys. Res. Lett.*, *30*(6), 1327–1330, doi:10.1029/2002GL016500.
- Sergeev, V., A. Runov, W. Baumjohann, R. Nakamura, T. L. Zhang, A. Balogh, P. Louarnd, J. Sauvaud, and H. Reme (2004), Orientation and propagation of current sheet oscillations, *Geophys. Res. Lett.*, *31*, 5807–5810, doi:10.1029/2003GL019346.
- Sergeev, V. A., D. A. Sormakov, S. V. Apatenkov, W. Baumjohann, R. Nakamura, A. V. Runov, T. Mukai, and T. Nagai (2006), Survey of large-amplitude flapping motions in the midtail current sheet, *Ann. Geophys.*, *24*, 2015–2024, doi:10.5194/angeo-24-2015-2006.
- Shen, C., Z. J. Rong, X. Li, M. Dunlop, Z. X. Liu, H. V. Malova, E. Lucek, and C. Carr (2008), Magnetic configurations of the tilted current sheets in magnetotail, *Ann. Geophys.*, *26*, 3525–3543, doi:10.5194/angeo-26-3525-2008.
- Shue, J.-H., and Y. Kamide (2001), Effects of solar wind density on auroral electrojets, *Geophys. Res. Lett.*, *28*, 2181–2184, doi:10.1029/2000GL012858.
- Sibeck, D. G., and J. T. Gosling (1996), Magnetosheath density fluctuations and magnetopause motion, *J. Geophys. Res.*, *101*, 31–40, doi:10.1029/95JA03141.

- Slavin, J. A., E. J. Smith, D. G. Sibeck, D. N. Baker, and R. D. Zwickl (1985), An ISEE 3 study of average and substorm conditions in the distant magnetotail, *J. Geophys. Res.*, *90*, 10,875, doi:10.1029/JA090iA11p10875.
- Sonett, C. P., J. D. Mihalov, and J. P. Klozenberg (1971), The flux content and form of the geomagnetic tail., *Cosmic Electrodyn.*, *Vol. 2*, p. 22 - 33, *2*, 22–33.
- Sonnerup, B. U. Ö., and M. Scheible (1998), Minimum and Maximum Variance Analysis, *ISSI Scientific Reports Series*, *1*, 185–220.
- Speiser, T. W. (1973), Magnetospheric current sheets, *Radio Sci.*, *8*, 973–977, doi:10.1029/RS008i011p00973.
- Speiser, T. W., and N. F. Ness (1967), The Neutral Sheet in the Geomagnetic Tail: Its Motion, Equivalent Currents, and Field Line Connection through It, *J. Geophys. Res.*, *72*, 131–141, doi:10.1029/JZ072i001p00131.
- Tanskanen, E. I., T. I. Pulkkinen, A. Viljanen, K. Mursula, N. Partamies, and J. A. Slavin (2011), From space weather toward space climate time scales: Substorm analysis from 1993 to 2008, *J. Geophys. Res.*, *116*, A00I34, doi:10.1029/2010JA015788.
- Thompson, S. M., M. G. Kivelson, K. K. Khurana, R. L. McPherron, J. M. Weygand, A. Balogh, H. Réme, and L. M. Kistler (2005), Dynamic Harris current sheet thickness from Cluster current density and plasma measurements, *J. Geophys. Res.*, *110*, A02212, doi:10.1029/2004JA010714.
- Tsurutani, B. T., R. L. McPherron, W. D. Gonzalez, G. Lu, N. Gopalswamy, and F. L. Guarnieri (2006), Magnetic Storms Caused by Corotating Solar Wind Streams, in *Recurrent Magnetic Storms: Corotating Solar Wind*, *Washington DC American Geophysical Union Geophysical Monograph Series*, vol. 167, edited by R. McPherron, W. Gonzalez, G. Lu, H. A. José, and S. Natchimuthukonar Gopalswamy, p. 1.

- Tsyganenko, N. A., and D. H. Fairfield (2004), Global shape of the magnetotail current sheet as derived from Geotail and Polar data, *J. Geophys. Res.*, *109*, A03218, doi:10.1029/2003JA010062.
- Tsyganenko, N. A., S. B. P. Karlsson, S. Kokubun, T. Yamamoto, A. J. Lazarus, K. W. Ogilvie, C. T. Russell, and J. A. Slavin (1998), Global configuration of the magnetotail current sheet as derived from Geotail, Wind, IMP 8 and ISEE 1/2 data, *J. Geophys. Res.*, *103*, 6827–6842, doi:10.1029/97JA03621.
- Wanliss, J. A., and K. M. Showalter (2006), High-resolution global storm index: Dst versus SYM-H, *J. Geophys. Res.*, *111*, A02202, doi:10.1029/2005JA011034.
- Weimer, D. R. (2004), Correction to “Predicting interplanetary magnetic field (IMF) propagation delay times using the minimum variance technique”, *J. Geophys. Res.*, *109*, A12104, doi:10.1029/2004JA010691.
- Weimer, D. R., and J. H. King (2008a), Improved calculations of interplanetary magnetic field phase front angles and propagation time delays, *J. Geophys. Res.*, *113*, A01105, doi:10.1029/2007JA012452.
- Weimer, D. R., and J. H. King (2008b), Correction to “Improved calculations of IMF phase-front angles and propagation time delays”, *J. Geophys. Res.*, *113*, A07106, doi:10.1029/2008JA013075.
- Weimer, D. R., D. M. Ober, N. C. Maynard, M. R. Collier, D. J. McComas, N. F. Ness, C. W. Smith, and J. Watermann (2003), Predicting interplanetary magnetic field (IMF) propagation delay times using the minimum variance technique, *J. Geophys. Res.*, *108*, 1026, doi:10.1029/2002JA009405.
- Wilken, B., C. K. Goertz, D. N. Baker, P. R. Higbie, and T. A. Fritz (1982), The SSC on July 29, 1977 and its propagation within the magnetosphere, *J. Geophys. Res.*, *87*, 5901–5910, doi:10.1029/JA087iA08p05901.

- Zelenyi, L. M., D. C. Delcourt, H. V. Malova, and A. S. Sharma (2002), “Aging” of the magnetotail thin current sheets, *Geophys. Res. Lett.*, *29*(12), 1608, doi:10.1029/2001GL013789.
- Zhang, T. L., W. Baumjohann, R. Nakamura, A. Balogh, and K. Glassmeier (2002), A wavy twisted neutral sheet observed by CLUSTER, *Geophys. Res. Lett.*, *29*(19), 1899–1902, doi:10.1029/2002GL015544.
- Zhang, T. L., R. Nakamura, M. Volwerk, A. Runov, W. Baumjohann, H. U. Eichelberger, C. Carr, A. Balogh, V. Sergeev, J. K. Shi, and K. Fornacon (2005), Double Star/Cluster observation of neutral sheet oscillations on 5 August 2004, *Ann. Geophys.*, *23*, 2909–2914, doi:10.5194/angeo-23-2909-2005.
- Zhang, T. L., W. Baumjohann, R. Nakamura, A. Runov, M. Volwerk, Y. Asano, Z. Vörös, H. Eichelberger, V. Sergeev, J. K. Shi, and A. Balogh (2006), A statistical survey of the magnetotail current sheet, *Adv. Space Res.*, *38*, 1834–1837, doi:10.1016/j.asr.2006.05.009.